Role of Ab Initio Calculations in the Design and Development of Lanthanide Based Single Molecule Magnets

Tulika Gupta, Mukesh Kumar Singh, and Gopalan Rajaraman

Contents

Abstract   In this book chapter, we have reviewed recent trends in employing ab initio calculations based on complete active space self-consistent field (CASSCF)/restricted active space spin interaction with spin–orbit coupling (RASSI-SO) procedure to interpret, rationalize and predict suitable lanthanide based molecular magnets. We begin with the general introduction on the methods used followed by various pragmatic instances where ab initio calculations have been employed to understand the magnetic anisotropy in lanthanide based single-ion magnets (SIMs). While a detailed section is dedicated to the mononuclear Dy^{III} SIMs, we have also covered other lanthanide SIMs briefly. Particularly, we have classified various SIMs based on the observed crystal-field splitting between ground and first excited states and this likely to shed light on the most important issue of suitable geometries that could yield high blocking temperature SIMs.

T. Gupta, M. K. Singh, and G. Rajaraman (✉)
Department of Chemistry, IIT Bombay, Mumbai, India
e-mail: rajaraman@chem.iitb.ac.in

1 Introduction

Since the first invention of single molecule magnet (SMM) in 1993, various realms have been researched ranging from zero-dimensional polymeric metal clusters to metal–radical SMMs, 1D single chain magnets (SCMs) and single-ion magnets (SIMs), etc. [1–11] While tremendous progress on synthesis of polynuclear metal clusters/SCMs/metal–radical systems has been achieved, structures are often not predictable and so is the magnetic characteristic. SIMs enact as remedy in this regard due to their facile synthesis and simplified structures compared to the complexities that lie in polynuclear SMMs [12]. Magnetic properties of SIMs are linked to the adjacent crystal field generated by the coordinated ligands [13]. This cumulatively invokes improved understanding between structural and magnetic properties in SIMs and entails the pivotal role of ligand field in the design and development of novel SIMs. For SIMs, the coordination number, local point group symmetry as well as crystal field strength need to be manoeuvred simultaneously to achieve larger energy barrier for magnetization reversal (U_{eff}). In SIMs, interaction between magnetic ion and surrounding ligand field is the origin of magnetic anisotropy. Compared to 3d and 5f congeners, 4f (Lanthanide, Ln[III]) based SIMs are more successful in achieving attractive magnetization blocking temperatures [14–17]. This is due to weaker lanthanide–ligand interactions and large unquenched orbital angular momentum, rendering strong spin–orbit coupling (SOC), leading to a large inherent magnetic anisotropy. Complexes with more than one 4f magnetic ions evoke weaker 4f-4f exchange rendering faster quantum tunnelling of magnetization (QTM) leading to a drastic reduction in the desired magnetization blockade. This is one of the major problems in the area of SMM where scientists are indulged in improving energy barrier and the blocking temperature. Recent breakthroughs in Ln[III]-SIMs, exhibiting improved energy barrier [18–20] and blocking temperature up to 60 K appeared [21, 22] to some extent relieve the ongoing contention and now focus is to enhance blocking temperature beyond liquid nitrogen temperatures.

Accounting these facts, we would confine our discussions to Ln[III]-based SIMs in this chapter. We will begin our discussion with the theoretical depiction of crystal field splitting and various avenues available to compute these parameters for Ln-based molecules. This will be followed up by brief discussion on the ab initio CASSCF/CASPT2 methodologies that are widely employed for the computation of spin Hamiltonian parameters of Ln[III] SIMs. This will be followed by discussion on various Ln[III] SIMs reported in the literature. While a detailed section has been devoted to Dy[III] ion based SIMs, for other lanthanide ions a succinct section is presented followed by conclusions and future outlook.
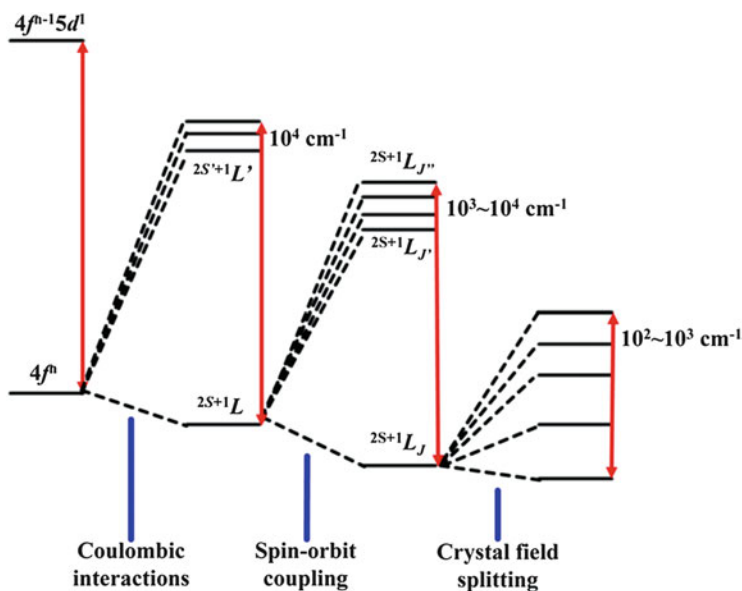
Fig. 1 Schematic diagram of the plausible energy level splitting for lanthanide ions in logarithmic energy scale. Reprinted with permission from Meng et al. [23] Copyright @1997 American Chemical Society

1.1 Theoretical Depiction of Crystal Field Splitting

Considering the strong SOC in lanthanides, patterns of $^{2S+1}L_J$ multiplets can be deduced by accounting strong inter-electron repulsion (coulombic) followed by the SOC. Weaker ligand field effect (compared to 3d congeners) subsequently promotes splitting of the $^{2S+1}L_J$ multiplets (see Fig. 1) [23]. As the ligand field splitting is dependent on the coordination environment, it dictates in the Ln^{III}-SIMs/SMMs, the nature of magnetic anisotropy and its relaxation process [24]. It is a well-established fact that, in order to gain insights into the magnetic characteristics in Ln^{III}-SIMs/SMMs and develop magneto-structural correlation, we need to estimate the corresponding crystal field parameters [25]. This solely relies on the 27 crystal field parameters corresponding to the symmetry of central lanthanide ions. The crystal field can be denoted as follows [26]:

$$\widehat{H} = \sum_{i,k,q} B_k^q O_k^q(\theta_i, \varphi_i) \tag{1}$$

where $O_k^q(\theta_i, \varphi_i)$ delineates Stevens operator which relies on angular coordinates (θ_i, φ_i) as expressed within the given coordinate system, B_k^q depicts crystal field parameters for the ranks = 2, 4, 6, i indicates the number of electrons and q ranges from $-k$ to $+k$. Although efforts have been made to estimate these parameters using experimental techniques, as there are numerous possibilities, a single experimental/spectroscopic technique alone is not suffice to obtain the full depiction of crystal

field splitting and directions of local anisotropy axes precisely. This rejuvenates the need to implicate versatile theoretical models [27, 28] to illustrate crystal field splitting in Ln^{III}-SIMs/SMMs and with time it has proven to be extremely useful both for understanding the anisotropy and also to design molecules possessing attractive magnetic properties.

1.1.1 Ab Initio Description of Crystal Field Splitting

As explained earlier, various experimental obstacles necessitate the estimation of crystal field parameters from first principles to facilitate targeted synthesis of lanthanide compounds to avoid serendipitous assembly. In this context, ab initio methodologies embedded within MOLCAS [29–35] suite have been proven to be viable in the depiction of wave functions, energies as well as Zeeman interactions in terms of the pseudospin operators of the low-lying multiplets [36]. These calculations for lanthanide elements were pioneered by Chibotaru and co-workers and remain ubiquitous for the rationalization of the magnetic properties of lanthanides [37]. Within the used approach, relativistic effects have been considered based on Douglas–Kroll–Hess (DKH) Hamiltonian [38, 39]. In the first step of this computational process, scalar relativistic effects are considered for the generation of basis sets. In the next step, spin-free eigenstates are generated with active space formed by the lanthanide 4f orbitals embedded within CASSCF (complete active space self-consistent field) approach of MOLCAS module. This is followed by restricted active space (RAS) [35] calculation accounting spin–spin and spin–orbit coupling (RASSI-SO) employing the previous steps resultant eigenfunctions as input states. Here, the SOC is illustrated within the atomic mean field integral (AMFI) approximation [40]. This leads to the generation of spin–orbit eigenfunctions as linear combinations of aforestated spin-free functions. At the final step, specifically selected precise eigenfunctions are projected onto pseudospin operator $\tilde{S}$. The aforementioned ab initio approach postulates crystal field splitting of the ground atomic J-multiplet of lanthanide ions (multiplet specific crystal field Hamiltonian) [26, 28]. For accurate determination of crystal field parameters (B_k^q), highly beneficial irreducible tensor operator (ITO) technique has been employed (within SINGLE_ANISO module of MOLCAS). The advantage of this approach is well established and can be expressed in terms of crystal field states $|J_M>$ [26]. This induces acquirement of crystal field parameters for specific coordination frame/quantization axis [26]. The key feature of this approach lies in unique way of deducing crystal field parameters without the utilization of fitting procedure as employed in other methods. Therefore, the spin–orbit energy multiplets obtained from the previous RASSI-SO step will be subsequently used to derive crystal field parameters [37, 41]. For the deduction of principal g-tensor values of Kramers doublet, pseudospin $\tilde{S} = \frac{1}{2}$ formalism has been utilized. Hence, the ab initio calculations render accurate illustration of the energy multiplets and corresponding energies. Although these calculations are expensive, their robustness made them persuasive towards rational design of 4f – based SIMs/SMMs.

1.1.2 Electrostatic Definition for Crystal Field Splitting Based on True Electronic Charge Distribution

Despite the versatility of the ab initio calculations, these calculations are often computationally demanding and possibly cannot be used for screening large number of molecules. To overcome these shortcomings, other qualitative methodologies to obtain CF parameters are proposed. In this regard, the electrostatic effects of the ligands coordinated to lanthanide on the ground state have been considered. This electrostatic model (true electronic charge based) has been developed counting on the aspherical lanthanide 4f electron density distribution for the free ions following Hund's rule and $|\pm M_J>$ energy state configuration [42–44], positions and charges of the adjacent coordinated ligands. Minimization of electrostatic energy for the estimation of ground state magnetic anisotropy axis forms the basis of this methodology. The charge of the coordinated atoms of the ligands dictates the electrostatic potential realized by the central metal ion. This induces evaluation of electrostatic field generated by ligand charges within minimal valence bond (VB) model [42] and promotes construction of crystal field potential from fractional formal charges as embedded within the aforementioned model (exclusion of neutral atoms). After the deduction of ligand charges based on charge partitioning, electrostatic potential can be estimated from the well-known crystal field theory. This instigates estimation of the $|\pm M_J>$ multiplet energy as a function of ion orientation. Therefore, VB model coupled with electrostatic energy minimization generates specific orientation of principal anisotropy axis and preferential alignment of the crystal field quantization axis for a specific geometry. The issues pertain to addressing neutral ligands and failing to address systems where the ground state $|\pm M_J>$ strongly mixes with excited states restricting the prevalence of this model towards precise deduction of magnetic anisotropy/crystal field parameters; yet, as these methods are computationally robust, this has been often used to screen large number of molecules possessing interesting magnetic characteristics.

1.1.3 Electrostatic Description for Crystal Field Splitting Based on Effective Point-Charge Distribution

This model is based on the estimation of effective crystal field Hamiltonian, which considers classical effective point-charge electrostatic (PCE) model around the central magnetic ion [24, 45–51]. This model parameterizes ligand field effect around the central Ln^{III} ion by positioning point charges (LoProp, Mulliken) at the pertinent metal surrounding ligand atom positions. Further improvements to this model were implemented by placing effective charges amidst the chemical bonds, different donor atoms, by incorporating ab initio computed charges/parameters. Using this point-charge model, splitting of lanthanide $|\pm M_J>$ sublevels has been nicely illustrated. In this approach, effective charge, effective radial distance along the bond between metal and coordinated ligand atom, effective displacement perpendicular to that bond and a few other parameters are taken into consideration.

These are free fitting parameters acquired from high-resolution spectroscopic data for the corresponding lanthanide systems.

The accuracy of these models depends on how good these models are in replicating the experimental data? The electrostatic anisotropy axis (orientation of the principal magnetization based on electrostatic model of true charges) [42] lies in close proximity to the ab initio calculated and experimentally determined anisotropy axis (wherever applicable). But, this model is not valid when: (1) a system possesses ground state which strongly mixes with the excited states and (2) a system does not take into consideration the uncharged ligands. The PCE model nicely explains the experimental SMM/SIM characteristics through estimation of crystal field parameters and eigenvector contributions of the low-lying energy multiplets [49]. This model is known to closely replicate the energies of the first excited energy levels against experiment. However, higher energy levels as predicted by this model deviate from experimental data by <15% and also fourth range extra-diagonal crystal field parameters come into play [48]. Lack of accurate determination of symmetry axis within the molecule diverts the expected direction of principal magnetization direction. But, the bottleneck of this model underlies in the estimation of varieties of transferable robust parameters for broad range of ligands. In the literature, most of the single-crystal magnetometry measured crystal field splitting direction were compared with respect to that obtained from ab initio calculations accentuating its prevalence over other models. The divergence between ab initio calculations and experimental data has generally been found to be ~10–20 cm^{-1}/ ~30%. The deviation ascribes to the fact that the calculations are undertaken on non-optimized geometries and at ~100 K. However, the magnetic and spectroscopic measurements are usually performed at comparatively much lower temperatures. Incorporation of dynamic correlation (CASPT2) or enhancement of active space (RASSCF) in conjunction with electrostatic Madelung potential of the crystal attenuates the demarcation between the experimental and ab initio calculated energies [26]. Accounting all these explanations, ab initio calculations seem to be promising in deducing crystal field splitting energy levels of the lanthanide complexes (see Fig. 2). Recent years have witnessed substantial progress in the ab initio calculations owing to precision and pace towards novel synthetic design of SIMs/ SMMs. Efficient intuitive potential continues to keep them in the limelight and they continue to play pivotal role towards experimental synthesis of SIMs/SMMs beyond serendipity.

Utilizing ab initio calculations for the deduction of exchange spectrum and exchange parameters in polynuclear lanthanide complexes remains elusive compared to the estimation of crystal field splitting in mononuclear SIMs. Polymeric complexes are dealt in two steps: (a) fragmentation of the polymeric structure into mononuclear fragments and rigorous ab initio calculations on each monomeric fragment. This is followed by (b) effective evaluation of the magnetic exchange interaction between the monomeric fragments [28]. The magnetic coupling between the magnetic sites is accounted within the Lines model [52] where dipole–dipole coupling is considered exactly. The Lines model evokes derivation of anisotropic magnetic coupling between the spin moments of the magnetic centres in the absence of SOC by a single parameter. Incorporation of isotropic Heisenberg model with
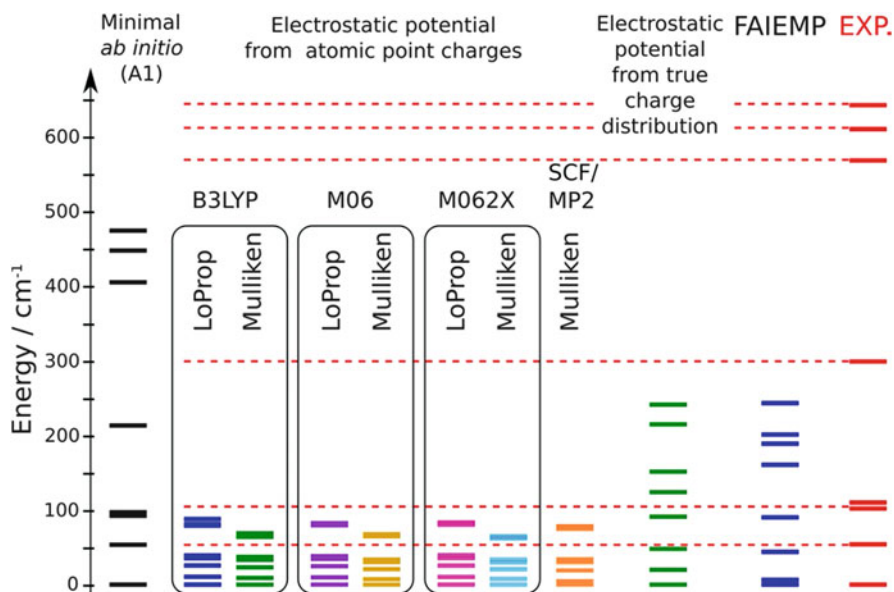
Fig. 2 Comparisons of the crystal field spectrum in Er-trensal complexes as obtained from various electrostatic models and ab initio calculations. Reprinted from Ungur and Chibotaru [26] with permission from John Wiley and Sons

effective parameter implicating true spins of the two magnetic sites has been carried out. This is followed by composition of the matrix based on the products from the localized lowest energy levels of the two magnetic sites obtained from fragmented ab initio calculations. The resultant exchange matrix outlines the exchange interaction in three limiting instances: (1) one anisotropic and one isotropic magnetic centre (Ising + Heisenberg = Ising exchange), (2) two anisotropic magnetic centres (Ising exchange) and (3) two isotropic magnetic centres (Heisenberg exchange). The Lines model depicts the magnetic coupling accurately in first case mentioned above (between the anisotropic and the isotropic ions). In remaining instances, Lines model enacts as a reasonable approximation and implementation of these methodologies in POLY_ANISO routine by Chibotaru and co-workers enables one to carry out such simulations for {3d-4f} systems [37, 53].

2 Modelling Magnetic Anisotropy of Lanthanide Single-Ion Magnets Using Ab Initio Calculations

Due to the multi-configurational nature of the ground as well as low-lying excited states of the lanthanide ions, ab initio CASSCF approach is indispensable for the description of the lanthanide electronic and magnetic properties. Selection of orbitals in CASSCF approach is undertaken by partitioning the molecular orbitals (MO) into:

inactive (doubly occupied), active and virtual (empty) orbitals. The inactive and virtual orbitals remain doubly occupied and empty, respectively, in all possible configurations utilized to construct CASSCF wave function. The rest of the electrons occupy correlated orbitals and that is considered as active space. The CASSCF wave function can be considered as linear combination of all plausible configurations (Slater determinants, SDs) which are formed by the partitioning scheme. The CASSCF active orbitals are supposedly some of the highest occupied and lowest unoccupied orbitals generated from restricted Hartree–Fock (RHF) calculations. Within the active MOs, full configuration interaction (CI) calculations are carried out and all configurational state functions (CSF) must be included within the CASSCF optimization. Coefficients of the SDs (CI coefficients) and the MO consideration rendered minimization of energy. Within active space, only limited/ specific numbers of SD configurations are constructed by allowing electronic excitation to higher energy orbitals. Therefore, the CASSCF wave function can be variationally optimized through optimization of CI coefficients in the CI expansion and the MOs, as mentioned earlier. The type of orbitals to be incorporated into the active space of CASSCF approach is dependent upon the nature of computational problem we intend to address. The viability of CASSCF approach in resolving lanthanide problems lies in its ability to depict systems possessing near-degeneracy and close-lying excited states. This make this method ubiquitous for the delineation of magnetic anisotropy and the associated crystal field parameters of lanthanide complexes. CASSCF wave function accounts only for the static electronic correlation and meagre number of electrons spreading the frontier MOs are correlated between them. In order to consider dynamic electron correlation, perturbative CASPT2 approach consideration is indispensable which renders better description of the magnetic properties (as stated in Sect. 1.1.3). Although CASSCF remains the omnipresent electronic structure method to study the multi-configurational systems, computational cost enhances proportionally with the number of active orbitals and active electrons. This poses a challenge to the method as often larger reference space is required to address complex chemical problems. If excitations from/to the orbitals beyond the chosen CAS reference space are envisioned, alternative approach can be adapted to enhance the size of the reference space. This secondary space is known as 'RAS' and excitation limits to one or two electrons only. In this RASSCF methodology, active MOs are partitioned into three sections: RAS1, RAS2 and RAS3 containing restrictions on the number of allowed excitations (occupations). The RAS1 and RAS3 space belongs to doubly occupied and empty MOs of the HF reference determinants, respectively. Limited number of excitations from RAS1 is allowed while identical excitation is allowed from RAS1/RAS2 to RAS3. RAS2 is reminiscent of the active space depicted earlier in the CASSCF approach where all plausible electronic arrangements within the orbitals are allowed. Henceforth, although all plausible electronic configurations within CAS space are permitted, only specific number of RAS configurations exists. So, RASSCF renders reasonable solutions for degenerate systems both in ground and excited states. Notably, in general calculations, we only consider RAS2 active space putting no holes/electrons/orbitals in RAS1/RAS3 space. However, enhancement of the active space by

the utility of RAS1/RAS3 space has pronounced effect in providing better depiction of the electronic and magnetic properties (as stated in Sect. 1.1.3). All these key features are inscribed within MOLCAS suite. MOLCAS suite also enables estimation of the molecular properties harnessing formulas of expectation values or finite perturbation theory utilizing the RASSI (restricted active space spin interaction) programme. RASSI evaluates interaction between various CASSCF/RASSCF wave functions based on orbitals that are non-orthonormal. RASSI is generally used to evaluate transition dipole moments in spectroscopy and to acquire eigenstates of relativistic Hamiltonian with the incorporation of spin–orbit (SO) interaction. During the study of lanthanide properties, precision of SO coupling treatment is a crucial feature to comply with their pertinent vital relativistic effects. Within the RASSI-SO approach, as implemented in MOLCAS package, SOC is considered non-perturbatively within the mean-field theory. It is noteworthy to mention here that RASSI-SO treats all wave functions as 'frozen', i.e. CASSCF/RASSCF wave functions do not alter during the computations. In the end, these consequential ground as well as excited spin–orbit multiplets are harnessed to perform non-perturbative computation of: (a) effective spin (pseudospin) Hamiltonian, (b) static field and temperature dependence magnetic features and (c) pseudospin Hamiltonians for Zeeman interaction (g tensors) using the SINGLE_ANISO routine of MOLCAS.

Another important aspect that needs to be considered for lanthanides is the relativistic effects. The scalar relativistic effects are treated within the basis set consideration of atomic natural orbitals (ANOs) embedded with relativistic correction. The ANOs are obtained from the average density matrix of the ground and lowest excited states of the element and the element in an electric field. The ANO-RCC (RCC invokes relativistic and (semi-)core correlation) basis sets for the whole periodic table were formed utilizing average density matrix acquired from CI computation on ground as well as excited states of the ions inside the electric field (describing polarizability of the elements). These basis sets were constructed for relativistic one- or two-component calculations which include scalar relativistic effect via second order DKH Hamiltonian. For heavier elements, incorporation of correlation from semi-core electrons becomes extremely imperative. For lanthanides, 5s and 5p semi-core electrons are added in the correlation treatment entailing their inclusion even when the basis sets are being used. The remaining core electrons are delineated through minimal basis set and are abstained from the correlation treatment to evade larger basis set superposition errors. Hence, the standard ANO-RCC basis set library as embedded within MOLCAS routine is optimized for use with DKH transformation of one-electron integrals. Meticulous literature perusal on the ab initio calculations of lanthanide systems suggest that in all instances ANO-RCC basis sets as embedded within MOLCAS package were employed. However, the range of basis sets employed for the involved elements varied from ANO-RCC-VQZP $\rightarrow$ ANO-RCC-VTZP $\rightarrow$ ANO-RCC-VDZP $\rightarrow$ ANO-RCC-VDZ. At this level, the accuracy or choice of basis set for these types of anisotropy calculations remains elusive. However, from survey, we can postulate that: (a) increase of basis set (from double to triple to quadruple) on lanthanide ions always leads an enhancement in energy gap between ground and first

excited states as well as higher energy multiplets [13, 54] though reverse trend is also noted in some cases [55], (b) modification from ANO-RCC-VTZP → ANO-RCC-VDZP reveals ~10–15 cm^{-1} increment in barrier height estimated, (c) however, change from ANO-RCC-VQZP → ANO-RCC-VTZP poses hardly any effect on the barrier value or anisotropy nature, (d) in all these variations of ANO-RCC-VQZP → ANO-RCC-VTZP → ANO-RCC-VDZP, the g_{zz} values remain uniform throughout, (e) however, prominent change in barrier value/anisotropy behaviour was detected for basis set changes between ANO-RCC-VTZP → ANO-RCC-VTZ and ANO-RCC-VDZP → ANO-RCC-VDZ, i.e. addition of polarization functions in the basis sets found to induce pronounced impact and (f) in order to consider impact of neighbouring molecules, point charges were located at each atomic position of the crystal which does not exert prominent effect on anisotropy [54, 56]. The information required to perform computation on individual lanthanide ions are described in Table 1.

Cholesky decomposition of the two-electron integrals with a threshold of 10^{-8} is generally employed to avoid large usage of hard disk and reduce computational

Table 1 Illustrative table describing the electronic configuration of the individual Ln^{III} ions along with the expected g_{zz} value of the largest |M$_J$> level and possible multiplets that could be adapted for: (1) CASSCF calculations and (2) RASSI-SO step

Ions	Number of 4f electrons (4f^N)	Ground state term symbol	Expected g_{zz} for the highest $\| \pm M_J>$	Active space CAS (n, m)	Plausible CASSCF configurations	Multiplets mixed in the RASSI step
Ce^{III}	4f^1	$^2F_{5/2}$	4.5	CAS (1, 7)	7 doublets	7 doublets
Nd^{II}	4f^3	$^4I_{9/2}$	6.55	CAS (3, 7)	35 quartets and 112 doublets	35 quartets and 112 doublets
Tb^{III}	4f^8	$^7F_6$	18	CAS (8, 7)	7 septets, 140 quintets and 195 triplets	7 septets, 105 quintets and 112 triplets
Dy^{III}	4f^9	$^6H_{15/2}$	20	CAS (9, 7)	21 sextets, 224 quartets and 158 doublets[a]	21 sextets, 128 quartets and 130 doublets
Ho^{III}	4f^{10}	$^5I_8$	20	CAS (10, 7)	35 quintets, 210 triplets and 196 singlets	30 quintets, 99 triplets and 31 singlets
Er^{III}	4f^{11}	$^4I_{15/2}$	18	CAS (11, 7)	35 quartets and 112 doublets	35 quartets and 112 doublets
Tm^{III}	4f^{12}	$^3H_6$	14	CAS (12, 7)	21 triplets and 28 singlets	21 triplets and 28 singlets
Yb^{III}	4f^{13}	$^2F_{7/2}$	8	CAS (13, 7)	7 doublets	7 doublets

Here, n electrons are distributed in all plausible pathways in m orbitals
[a]Sometimes 21 sextets in CASSCF and RASSI-SO step would suffice the desired anisotropy behaviour in Dy^{III}

demand. The molecular orbitals (MOs) were optimized in state-averaged CASSCF calculations, where the active space was defined by the nine 4f electrons in the seven 4f orbitals of Dy^{III} (see Table 1). Considering the SOC, for the Dy^{III} site, the CASSCF calculation is executed at ground state ($S = \frac{5}{2}$) with all of the 21 configurations, the first excited state ($S = \frac{3}{2}$) with all of the 224 configurations and the second excited state ($S = \frac{1}{2}$) with the 158 configurations independently for each spin state. After the CASSCF calculation, the RASSI-SO calculations of RAS state interaction are undertaken. In this step, 21 configurations for the ground state; 128 configurations for the $S = \frac{3}{2}$ state and 130 configurations for the state $S = \frac{1}{2}$ states were mixed by SOC corresponding to an energy cut-off of ~50,000 cm^{-1}. However, only consideration of 21 sextets in CASSCF and RASSI-SO step for Dy^{III} has proven to be apt towards the determination of pertinent anisotropy [57]. For the Er^{III} centre, both the CASSCF and RAS calculations are executed at the ground state with all of the 35 configurations, and the doublet states with all of the 112 configurations. In a similar manner, for other Tb^{III}, Ho^{III}, Nd^{III}, Tm^{III}, Yb^{III} and Ce^{III} lanthanide ions specific numbers of configurations were harnessed in the CASSCF step which was followed by admixing of certain configurations in RASSI-SO approach as shown in Table 1.

3 Ab Initio Calculations on Lanthanide Based Magnets

Before we delve into the detailed compilation of the ab initio calculations on several experimental crystallographic geometries, it is important to stress on the prerequisites and suitable geometries for SIM characteristics. In transition metal based SMMs, the barrier height for reorientation of magnetization is known to be correlated to the $|D|S^2$ (for integer spin systems) with D representing axial zero-field splitting and S represents the ground state S value. In lanthanides, the anisotropy is correlated to the splitting of the lowest spin–orbit states by the crystal field terms. For example, in Dy^{III} SIMs, the splitting of $^6H_{15/2}$ by the crystal field determines the barrier height. This can be correlated to the familiar DS^2 equation of transition metals SMMs, where crystal field that plays the role of D and S is represented by the corresponding $|\pm M_J>$ levels. Naturally, to have a higher barrier height, a strong crystal field in particular direction and a large $|\pm M_J>$ level as the ground state are desired. In lanthanides, stabilization of the highest $|\pm M_J>$ level and minimal mixing of the corresponding ground multiplet wave function with the excited states are crucial to obtain larger energy barrier for magnetization reversal (U_{eff}/U_{cal}; in cm^{-1}).

As the nature of the anisotropy in lanthanides is correlated to the nature of electron density at the ground $|\pm M_J>$ level, the lanthanide ions are qualitatively divided into oblate and prolate type ions [43]. Depending on the type of ions, preferably axial and equatorial crystal fields are required to stabilize maximum angular momentum projection in oblate (Ce^{III}, Pr^{III}, Nd^{III}, Tb^{III}, Dy^{III} and Ho^{III}) and prolate (Pm^{III}, Sm^{III}, Er^{III}, Tm^{III} and Yb^{III}) ions, respectively. Meticulous
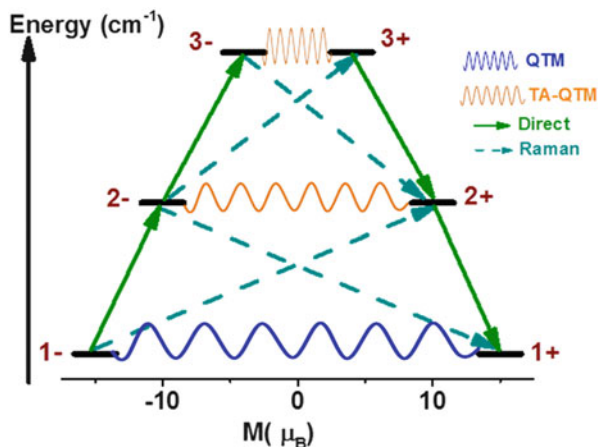
Fig. 3 Schematic representation of the energy multiplets ($\pm n$) pertinent to the crystal field components of the ground atomic J multiplet. The two energy states of specific doublet boast opposing values of magnetization such as $|+M_J\rangle$ and $|-M_J\rangle$, respectively. There are four kinds of relaxation pathways as indicated by the respective texts representing each arrows and curved arrows. Ideally, relaxation should be promoted by the direct (green arrows) process subject to the quenching of other relaxation mechanisms

literature perusal accentuates that compounds with point groups $C_{\infty v}$, $D_{\infty h}$, S_8, D_{4d}, D_{5h} and D_{6d} are most suited to achieve improved SIM/SMM behaviour [17, 58, 59]. Computed crystal field parameter B_2^0 (see Eq. 1) determines the nature of Ln^{III} centre and its corresponding sign (negative preferred) governs the magnitude of U_{eff}/U_{cal} values [49]. Complexes with suppressed QTM (as for ± 1 as indicated in Fig. 3) [24–26, 28, 60] within the ground multiplets of reverse magnetization (for Kramers ion and for non-Kramers ions lower value of tunnel splitting; Δ_{tun}) are favourable for SIM/SMMs. Besides, the ground multiplet should be strongly axial with oppressed transversal components ($g_{zz} \ggg g_{xx}/g_{yy}$), reasserting the need for higher ligand field symmetry around the central Ln^{III} metal ion to induce larger barrier. Thermally assisted QTM (TA-QTM; between ± 2 and ± 3 as represented by Fig. 3) within the higher energy levels of reversed magnetization also should ideally remain quenched. This should be accompanied by stronger spin–phonon relaxation pathways (Orbach, Raman and direct; between ± 1 and ± 2 or ± 2 and ± 3 states) via the higher energy multiplets to promote relaxation and procurement of larger barrier. Through ab initio calculations, one can attempt to estimate the transversal magnetic moment of the electronic transition matrix element corresponding to the various relaxation pathways, i.e. QTM, TA-QTM, Raman, Orbach, etc. [60, 61] One can also obtain the $g_{xx}/g_{yy}/g_{zz}$ values pertaining to the energy levels to determine the axiality/non-axiality of the complexes. Besides, the resultant crystal field parameters as acquired from the output of the ab initio calculations render determination of the preferred relaxation pathways and nature of the complexes. All aforestated avenues

will be taken into account in the following pragmatic discussion on calculation of magnetic anisotropy in lanthanide complexes.

We would like to note here that often the ab initio calculations yield barrier heights which are larger than the ones estimated from experiments. To distinguish these two parameters, here we are using the terminology U_{cal} for theoretically estimated effective energy barrier and U_{eff} for the values obtained from experiments. While the accuracy of the chosen methodology can be improved (incorporation of dynamic correlation, expansion of reference space, larger basis sets, etc.), still the differences are often larger. This difference between U_{cal} and U_{eff} values can be attributed to one of the following reasons: (1) while probability for QTM can be computed, this relaxation pathway is not taken in consideration while estimating U_{cal} values; (2) intermolecular interactions often play a critical role in the relaxation mechanism. Since the dipolar coupling between the metal ions is rather strong in lanthanides, this can facilitate further relaxation and this effect is not captured in the calculated U_{cal} values; (3) hyperfine coupling of metal ions and the coordinated ligands facilitate tunnelling process and this effect is completely neglected in the U_{cal} estimates and (4) other relaxation processes such as spin–lattice, multi-phonon excitations, etc. are possible while this has not been accounted in the estimate of U_{cal} values.

3.1 Illustrative Examples of Dy^{III} Single-Ion Magnets Studied Using Ab Initio Calculations

Since the invention of Ln^{III}-based SIM/SMM, Dy^{III} ($^{6}H_{15/2}$) complexes remain pervasive and this can be accrued onto their: (a) large total spin–orbit angular momentum quantum number, J/M_J, (b) stronger magnetic anisotropy compared to other lanthanides, (c) strongest magnetic moment and (d) odd number of 4f electrons assuring the presence of magnetic bistability and Kramers nature of ground multiplets. The Dy^{III} ion is an oblate type ion with equatorially expanded electron density and axial crystal field is imperative to stabilize the highest angular momentum projection. Stabilization of the largest M_J level as the ground state and the crystal field splitting of the M_J levels are the most desired characteristics of lanthanide based SMMs. Here, we intend to cover various Dy^{III} SIMs based on their ground state $|\pm M_J>$ levels and the computed crystal field splitting. This will help the research groups to choose the best ligand field suitable for Dy^{III} ion to develop new generation SMMs. Thus, here we classify the Dy^{III} SIMs/SMMs into six different categories: (1) category **A** deals with complexes having ground state other than $\frac{15}{2}$ ($|\pm M_J \neq \frac{15}{2}>$), (2) category **B** deals with Dy^{III} SMMs possessing $|\pm M_J = \frac{15}{2}>$ ground state but with significant QTM contributions leading to a field-induced SIM (f-SIM) behaviour, (3) category **C** deals with Dy^{III} SIMs possessing $|\pm M_J = \frac{15}{2}>$ ground state with weak crystal field splitting (first excited state lying at within ~50 cm^{-1}) exhibiting zero-field SMM characteristics, (4) category **D** deals with

Dy^{III} SIMs possessing $|\pm M_J = \frac{15}{2}>$ ground state with moderate crystal field splitting (first excited state lying within ~100 cm^{-1}) exhibiting zero-field SMM characteristics, (5) category **E** deals with Dy^{III} SIMs possessing $|\pm M_J = \frac{15}{2}>$ ground state with strong crystal field splitting (first excited state lying at >100 cm^{-1}) exhibiting zero-field SMM characteristics and (6) category **F** deals with Dy^{III} SIMs with easy plane/ hard axis anisotropy behaviour. To avoid repetition of molecular formulas and other details, we have listed all the molecular formula of all the complexes described in this chapter in a tabular form (see Table 2). Individual section deals with list of molecules belonging to their categories and this will be followed by non-Dy^{III} SIMs. In the conclusions section, we have cross compared the geometries and the computed barrier height to assess and understand how different geometries and ligand donor strength yield superior SIMs for Dy^{III}/Er^{III} and Tb^{III} ions. This will be followed by the future outlook describing the future directions that the ab initio calculations likely to focus in years to come.

3.1.1 Ab Initio Studies on Category A Complexes: Dy^{III} Complexes Having Ground State Other than $\frac{15}{2}$ ($|\pm M_J \neq \frac{15}{2}>$)

Although the largest $|\pm M_J>$ ($\pm = \frac{15}{2}$ in this instance) stabilization is the most preferred ground state for the Dy^{III} ions, there are a few examples in the literature where complexes with concomitant non-$|\pm M_J = \frac{15}{2}>$ ground energy level exhibit SIMs/SMMs behaviour. CASSCF+RASSI-SO+SINGLE_ANISO calculations performed on complex **1** (see Table 2 for molecular formula) suggest the ground state wave function to be $|\pm M_J = \frac{13}{2}>$ state [62]. This was further corroborated by the computed g_{zz} value of 16.9 corresponding to the $|\pm M_J = \frac{13}{2}>$ energy level in conjunction with prominent transverse anisotropy components, i.e. $g_{xx} = 0.4$ and $g_{yy} = 0.3$ (see Fig. 4a and Table 3). Magnetic measurements indicate an f-SIM behaviour for **1** with U_{eff} value estimated to be 23.63 cm^{-1}. Ab initio calculations, however, yield the effective barrier (U_{cal}) of 84.7 cm^{-1} (with respect to first excited Kramers doublet; KD) [62]. Complex **1** has ten-coordinate Dy^{III} centre with four nitrogen donors and six oxygen donor atoms (see Fig. 4a and Table 3), and the weaker coordination by the nitrogen donors leads to the stabilization of $|\pm M_J = \frac{13}{2}>$ state. From the combined experimental and theoretical studies, it becomes clear that for the Dy^{III} ion, placing the crystal field above and below the XY plane along the computed g_{zz} axis likely yields the largest M_J value as ground state and improved SMM characteristics [62].

Complex [Dy(COT)$_2$]$^-$ (**2**) (see Fig. 4b and Tables 2 and 3) is a zero-field SIM and is found to possess $|\pm M_J = \frac{9}{2}>$ ground state with nominal contributions from other $|\pm M_J>$ projections. This was supported by pronounced QTM within ground multiplet as revealed by pertinent transversal magnetic moment of 0.04 μ$_B$. Computed main g-anisotropic factors, i.e. $g_{xx} = g_{yy} = 1.6 \times 10^{-1}$ and $g_{zz} = 12.64$ favoured the nature of aforementioned ground state wave function (see Table 3). The non-axiality of first excited KD in combination with non-collinear anisotropy axis

Table 2 Molecular formula of all the studied complexes

	Structure
1	[Dy (L)]; (L = *N,N'*-bis(amine-2-yl)methylene-1,8-diamino-3,6-dioxaoctane)
2	[Dy(COT)$_2$]$^-$; ({COT} = Cyclooctatetraene)
3	[DyPc$_2$]$^-$; (Pc = Phthalocyanine)
4	[Dy(FTA)$_3$L]; {FTA = 2-furyl-trifluoro-acetonate, L = (S,S)-2,2'-Bis(4-benzyl-2-oxazoline)}
5	[Dy(12C4)(H$_2$O)$_5$] (ClO$_4$)$_3$.H$_2$O; ({12C4} = 12-crown-4)
6	[Dy(H$_2$L)(NO$_3$)$_3$]; {H$_2$L = *N,N',N''*-trimethyl-*N,N''*-bis(2-hydroxy-3-methoxy-5-methylbenzyl)
7	[Dy(paaH*)$_2$(NO$_3$)$_2$(MeOH)][NO$_3$]; (paaH* = The neutral zwitterionic *N*-(2-Pyridyl)-ketoacetamide)
8	[Dy(H$_2$DABPH)$_2$](NO$_3$)$_3$; (H$_2$DABPH = 2,6-diacetylpyridinebis(benzoic acid hydrazone)
9	[Dy(H$_2$DABPH)(HDABPH)](NO$_3$)$_2$
10	[Na{Dy(DOTA)(H$_2$O)}]; (DOTA = 1,4,7,10-tetraazacyclo-dodecane-1,4,7,10-tetraaceticacid)
11	[Dy(9Accm)$_2$-(NO$_3$)(dmf)$_2$]; (Accm = 1,7-di-9-anthracene-1,6-heptadiene-3,5-dione)
12	[Dy(NTA)$_3$L]; (L = (1R,2R)-1,2-diphenylethane-1,2-diamine, NTA = Nitrilotriacetic acid)
13	[K(DME)$_2$][Dy(tmtaa)$_2$]; (H$_2$tmtaa = acrocyclic 6,8,15,17-tetramethyl-dibenzotetraaza[14]annulene)
14	[K(DME)(18-crown-6)][Dy(tmtaa)$_2$]
15	[Dy(TTA)$_3$(L$_3$)]; (TTA = 2-thenoyltrifluoroacetonate; L$_3$ = 4,5-pinenebipyridine)
16	[Dy(H$_2$BPz^{Me2}$_2$)$_3$]
17	[Zn$_3$Dy(L^{Pr})(NO$_3$)$_3$(MeOH)$_3$]·4H$_2$O; specific macrocycle (L^{Pr})$^{6-}$ was prepared by reaction between 1,4-diformyl-2,3-dihydroxybenzene and 1,3-diaminopropane at room temperature in methanol
18	[R,R-ZnLDy(μ-OAc)(NO$_3$)$_2$]; (H$_2$L = phenol,2,2'[2,2-diphenyl-1,2-ethanediyl]bis[(E)-nitrilomethylidyne]-bis(6-methoxy)
18a	[S,S-ZnLDy(μ-OAc)(NO$_3$)$_2$]; (H$_2$L = phenol,2,2'[2,2-diphenyl-1,2-ethanediyl]bis[(E)-nitrilomethylidyne]-bis(6-methoxy)
19	[DyCo$_2$(hmb)$_2$(CH$_3$O)$_2$(OAc)$_3$]; (H$_2$hmb = 2-hydroxy-3-methoxybenzylidene benzohydrazide)
20	[ZnDy(NO$_3$)$_2$(L)$_2$(CH$_3$CO)$_2$)]; (HL = 2-methoxy-6-[(E)-phenyliminomethyl]phenol)
20a	[Dy(HL)$_2$(NO$_3$)$_3$]; (HL = 2-methoxy-6-[(E)-phenyliminomethyl]phenol)
21	[Dy(H$_3$L)$_2$](NO$_3$); (H$_4$L = 2,2'-{[(2-aminoethyl)imino]bis[2,1-ethanediyl-nitriloethylidyne]}bis-2-hydroxy-benzoic acid)
22	[Dy(hfac)$_3$(L)] .0.5C$_6$H$_{14}$; (L = 3-(2-pyridyl)-4-aza[6]-helicene(racemic))
23	[Dy(15C5)(H$_2$O)$_4$](ClO$_4$)$_3$. (15C5); ({15C5} = 15-crown-5)
24	[Dy(COT'')$_2$Li(THF)(DME)]; {(COT'') = 1,4-bis(trimethylsilyl)cyclooctatetraenyl dianion}
25	[Dy(COT'')$_2$]$^-$
26	[Dy(dpq)(acac)$_3$]
27	[Dy(dppz)(acac)$_3$]
28	[Dy(acac)$_3$(H$_2$O)$_2$]
29a	[Dy(phen)(acac)$_3$]

Table 2 (continued)

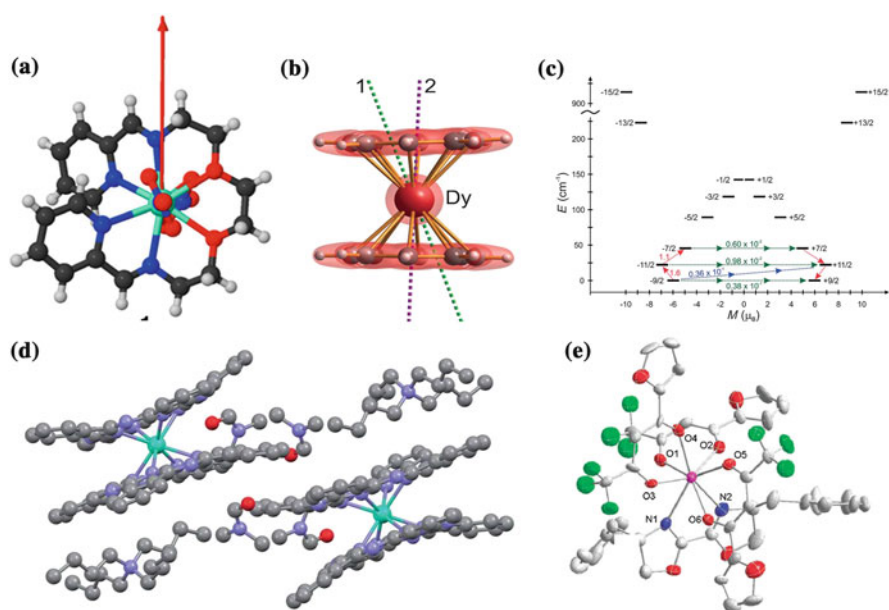|	Structure
29b	[Dy(TTA)$_3$(2,2′-bipyridine)]; (TTA = 4,4,4-trifluoro-1-(2-thienyl)-1,3-butanedionate)
30	[Dy(TTA)$_3$(1,10-phenanthroline)];
31a	[Dy(hfac)$_3$(L)]·C$_6$H$_{14}$; {hfac$^-$ = 1,1,1,5,5,5-hexafluoroacetylacetonate}
31b	[Dy(tta)$_3$(L)]·C$_6$H$_{14}$; {tta$^-$ = 2-thenoyltrifluoroacetonate}
32	[DyL]; (L = N,N'-bis(imine-2-yl)methylene-1,8-diamino-3,6-dioxaoctane)
33	[Dy(hfac)$_3$(L)]; L = 3-(2-pyridyl)-4-aza[6]-helicene (enantiomerically pure)
34	[Dy(tta)$_3$(L)]; (tta– = 2-thenoyltrifluoroacetonate, L = 2-{1-methylpyridyl-4,5-[4,5-bis (propylthio)tetrathiafulvalenyl]-1H-benzimidazol-2-yl}pyridine)
35	[ZnCl(μ-L)Dy(μ-L)ClZn]; (H$_2$L = N,N'-dimethyl-N,N'-bis(2-hydroxy-3-formyl-5-bromo-benzyl)ethylenediamine)
36	[{LZn(H$_2$O)}$_2$Dy(H$_2$O)]$^{3+}$; (L^{2-} = di-deprotonated form of the N$_2$O$_2$ compartmental N,N'-2,2-dimethylpropylenedi(3-methoxysalicylideneiminato))
37	[Dy(paaH*)$_2$(H$_2$O)$_4$][Cl]$_3$; (paaH* = N-(2-Pyridyl)-ketoacetamide)
38	[DyLCl$_2$(THF)$_2$ (DyNCN)]; (L = 2,6-(2,6-C$_6$H$_3$R$_2$N=CH)$_2$-C$_6$H$_3$)
39	[Ln(BIPM™^{S})$_2$][K(18C6)(THF)$_2$]; ({18C6} = 18-crown-6)
40	([Zn$_2$(L^1)$_2$DyCl$_3$]; (H$_2$L^1 = N,N'-bis(3-methoxysalicylidene)phenylene-1,2-diamine)
41	[Zn$_2$(L^1)$_2$Dy(MeOH)Br$_3$]; (H$_2$L^1 = N,N'-bis(3-methoxysalicylidene)phenylene-1,2-diamine)
42	[Zn$_2$(L^1)$_2$Dy(H$_2$O)Br$_2$]; (H$_2$L^1 = N,N'-bis(3-methoxysalicylidene)phenylene-1,2-diamine)
43	[Zn$_2$(L^2)$_2$DyCl$_3$]; (H$_2$L^2 = N,N'-bis(3-methoxysalicylidene)-1,2-diaminocyclohexane:)
44	Li(DME)$_3$[Dy(DAD)$_2$]; (DAD = ene-diamido[2,6-iPr$_2$C$_6$H$_3$N–CH=CH–NC$_6$H$_3$iPr$_2$–2,6]$^{2-}$
45	[Dy^{III}(NHPhiPr$_2$)$_3$(THF)$_2$]
46	[Dy(Bc^{Me})$_3$]; (Bc^{Me-} = dihydrobis(methylimidazolyl)borate)
47	[Dy(LH)$_3$]; (LH$^-$ = 2-hydroxy-N'-[(E)-(2-hydroxy-3-methoxyphenyl) methylidene] benzohydrazide)
48	[{LZn(Br)}$_2$Dy(H$_2$O)]$^+$; (L^{2-} = di-deprotonated form of the N$_2$O$_2$ compartmental N,N'-2,2-dimethylpropylenedi(3-methoxysalicylideneiminato))
49	[{LZn(Cl)}$_2$Dy(H$_2$O)]$^+$; (L^{2-} = di-deprotonated form of the N$_2$O$_2$ compartmental N,N'-2,2-dimethylpropylenedi(3-methoxysalicylideneiminato))
50	[LZnBrDy(ovan)(NO$_3$)(H$_2$O)]; (L^{2-} = di-deprotonated form of the N$_2$O$_2$ compartmental N,N'-2,2-dimethylpropylenedi(3-methoxysalicylideneiminato))
51	[LZnClDy(thd)$_2$]; (thd = 2,2,6,6-tetramethyl-3,5-heptanedionato ligand)
52	[(LZnBr)$_2$Dy (MeOH)$_2$]$^+$; L = dideprotonated forms of the 2-{(E)-[(3-{[(2E,3E)-3-(hydroxyimino)-butan-2-ylidene]amino}-2,2-dimethylpropyl)imino]methyl}-6-methoxyphenol
53	[(Cp^{ttt})$_2$Dy][B(C$_6$F$_5$)$_4$]; (Cp^{ttt} = 1,2,4-tri(tertbutyl)cyclopentadienide)
54	[Dy(Cp^{ttt})$_2$][B(C$_6$F$_5$)$_4$]; (Cp^{ttt} = {C$_5$H$_2$^{t}Bu$_3$-1,2,4} and ^{t}Bu = C(CH$_3$)$_3$)
55	[Dy(tta)$_3$(L)] (polymorph-t); (L = 4-[6-(1,3-benzothiazol-2-yl)pyridin-3-yl]-4′5′-bis (methylthio)tetrathiafulvene)
55′	[Dy(tta)$_3$(L)] (polymorph-m); (L = 4-[6-(1,3-benzothiazol-2-yl)pyridin-3-yl]-4′5′-bis (methylthio)tetrathiafulvene)
56	[Dy(Cy$_3$PO)$_2$(H$_2$O)$_5$]Cl$_3$; (Cy3PO = tricyclohexyl phosphine oxide)
57	[Dy(Cy$_3$PO)$_2$(H$_2$O)$_5$]Br$_3$; (Cy3PO = tricyclohexyl phosphine oxide)
58	[Dy(bbpen)Cl]; (H$_2$bbpen = N,N'-bis(2-hydroxybenzyl)-N,N'-bis(2-methylpyridyl) ethylenediamine)

(continued)

Table 2 (continued)

	Structure
59	[Dy(bbpen)Br]; (H$_2$bbpen = N,N'-bis(2-hydroxybenzyl)-N,N'-bis(2-methylpyridyl) ethylenediamine)
60	[Zn$_2$DyL$_2$(MeOH)]$^+$; (L = 2,2',2''-(((nitrilotris(ethane-2,1-diyl))tris(azanediyl))tris(methylene))tris-(4-bromophenol))
61	[Dy(O^{t}Bu)$_2$(py)$_5$][BPh$_4$]
62	[L$_2$Dy(H$_2$O)$_5$][I]$_3$; (L = ^{t}BuPO(NH^{i}Pr)$_2$)
63	[Dy(CyPh$_2$PO)$_2$(H$_2$O)$_5$]Br$_3$
79	[Er(thd)$_3$(bath)]; (bath = bathophenanthroline)
80	[Er(COT)$_2$]$^-$; (COT = (cyclooctatetraenyl dianion))
81	[Er(COT'')$_2$]$^-$; (COT'' = 1,4-bis-(trimethylsilyl) cyclooctatetraenyl dianion)
82	[Er(COT)Cp*]$^-$; (Cp* = pentamethylcyclopentadienide and COT = cyclooctatetraenyl dianion)
83	[Er(N(SiMe$_3$)$_2$)$_3$]
84	[Er(NHPhiPr$_2$)$_3$(THF)$_2$]
85	[Er{N(SiMe$_3$)$_2$}$_3$Cl].2THF
85a	[Er{N(SiMe$_3$)$_2$}$_3$Cl]$^-$
86	[Er(HL)$_2$(NO$_3$)$_3$]; (HL = 2-methoxy-6-[(E)-phenyliminomethyl]phenol)
87	(NBu$_4$)$^+$[ErPc$_2$]$^-$.2DMF
88	[Er(COT)$_2$]$^-$
89	[Er(trensal)]; (H$_3$trensal = 2,2',2''-Tris-(salicylideneimino)triethylamine)
90	[Er(3-I,5-Me-trensal)]
91	[Er(5-Cl-trensal)]
92	Na[ErDOTA(H$_2$O)]·4H$_2$O
93	[Yb(H$_3$L)$_2$]Cl$_3$; (H$_3$L = tris(((2-hydroxy-3-methoxybenzyl)amino)ethyl)-amine)
94	Na[Yb(DOTA)(H$_2$O)]·4H$_2$O
95	Na[Tb(DOTA)(H$_2$O)]·4H$_2$O
96	Na[Ho(DOTA)(H$_2$O)]·4H$_2$O
97	Na[Tm(DOTA)(H$_2$O)]·4H$_2$O
98	[Yb(DTMA)OH$_2$]$^{3+}$
99	[Yb(DTMA).F]$^{2+}$; Yb-F = 1.97 Å
100	[Yb(DTMA)F]$^{2+}$; Yb-F = 2.38 Å
101	[Ce{Zn(L)}$_2$(MeOH)]BPh$_4$; (L = N,N,O,O-tetradentate Schiff base ligand)
102	[Li(dme)$_3$][Ce(COT'')$_2$]; (DME = dimethoxyethane, COT'' = 1,4-bis(trimethylsilyl) cyclooctatetraenyl dianion)
103	[CeCd$_3$(Hquinha)$_3$(n-Bu$_3$PO)$_2$I$_3$]; quinaldichydroxamic acid (H2quinha)
104	[NdCd$_3$(Hquinha)$_3$(n-Bu$_3$PO)$_2$I$_3$]; quinaldichydroxamic acid (H2quinha)
105	[L$_2$Nd(H$_2$O)$_5$][I]$_3$; (L = ^{t}BuPO(NH^{i}Pr)$_2$)
106	(NBu$_4$)$^+$[HoPc$_2$]$^-$.2dmf
107	[Ho(BcMe)$_3$]; ([BcMe]$^-$ = dihydrobis(methylimidazolyl)borate)
108	[Ho(BpMe)$_3$]; ([BpMe]− = dihydrobis(methypyrazolyl)borate)
109	[Ho(CyPh$_2$PO)$_2$(H$_2$O)$_5$]I$_3$; (Cy = cyclohexyl)
110	[(Tp)Tm(COT)]; (Tp = hydrotris(1-pyrazolyl)borate; COT = cyclooctatetraenide)
111	[(Tp*)Tm(COT)]; (Tp* = hydrotris(3,5-dimethyl-1-pyrazolyl)borate)
112	[Pc$_2$Ln]$^-$ TBA$^+$; (Pc = dianion of phthalocyanine; TBA$^+$ = N(C$_4$H$_9$)$_4$$^+$)

<div align="right">(continued)</div>

Table 2 (continued)

	Structure
113	$[Tb(BcMe)_3]$
114	$[Tb(BpMe)_3]$
115	$Li(DME)_3[Tb(DAD)_2]$; (DAD = ene-diamido[2,6-iPr$_2$C$_6$H$_3$N–CH=CH–NC$_6$H$_3$iPr$_2$-2,6]$^{2-}$)
116	$[(Pc)Tb]\{Pc[O(C_6H_4)\text{-}p\text{-}tBu]_8\}$
117	$[Tb\{Pc[OC_{11}H_{21}]_4\}_2]$
118	$[Tb\{Pc[N(C_4H_9)_2]_8\}_2]$
119	$[(Pc)Tb\{Pc[N(C_4H_9)_2]_8\}]$; $\{Pc[N(C_4H_9)_2]_8 = 2,3,9,10,16,17,23,24$-octakis(dibutylamino) phthalocyaninate, Pc = phthalocyaninate$\}$

Fig. 4 (**a**, **b**, **d**, **e**) Molecular structures of complexes **1–4**, respectively. Arrows in complex **1** and **2** (green colour) show the orientation of the principal magnetization axis. In complex **2**, violet colour arrow shows direction of KD2 g_{zz} axis. (**c**) Ab initio computed relaxation mechanism in complex **2**. Colour code: central atom = Dy, red = O, dark blue/light blue = N, black/dark-brown/light-brown/white-ellipsoid shape = C, green = F and small-spherical white = H atoms. Reprinted with permission from Campbell et al. [62] Copyright@2014 American Chemical Society. Reprinted from Ungur et al. [13] with permission from John Wiley and Sons. Reprinted from Marx et al. [54], Li et al. [63] with permission from the Royal Society of Chemistry

Table 3 List of complexes {from category A} with pertinent experimental energy barrier (U_{eff}, in cm^{-1}), ab initio computed energy barrier (U_{cal}, in cm^{-1}), main magnetic g factors, ground state M_J levels (major contributing) and crystallographic structural information

	U_{eff}	U_{cal}	g_{xx}–g_{yy}	g_{zz}	KD1	Type of coordinated atoms	Structure	Ref.
1	23.6	84.7	0.3–0.4	16.9	±13/2	4 N, 6 O	Distorted bicapped square antiprismatic	[62]
2	7.6	22.3	0.06–0.14	12.64	±9/2	(η^8-fashion)-All C	–	[13]
3	35	52.3	~10^{-4}	17.36	±13/2	8 N	–	[54]
4	37.8	67.2	0.16–0.33	19.24	±11/2	6 O, 2 N	Distorted bicapped triangular prism	[63]

alignment renders U_{cal} value of 22.3 cm^{-1} against experimental U_{eff} estimate of 7.6 cm^{-1}.

Complex **2** is composed of two {COT}$^{2-}$ ligands which are bound to central Dy^{III} ion in an η_8 fashion with one equivalent of [K(18-crown-6)] counter ion. Transverse contribution to ligand field from π cloud of COT causes stabilization of $|\pm M_J = \frac{9}{2} >$ as ground state with partial mixing from other states. The planar COT ligands present in complex **2** exhibit strong equatorial interaction and weak axial interaction. This leads to stabilization of intermediate $|\pm M_J>$ as the ground state. This is clearly reflected in the computed CF parameters where contrary to the expected negative sign, positive crystal field parameters B_2^0 and B_4^0 (3.51 and 0.02, respectively) are found and this enacted as genesis for the non-$|\pm M_J = \frac{15}{2} >$ ground energy level in **2** (see Fig. 4c for computed magnetization relaxation mechanism) [13].

Ab initio calculations on complex **3** (see Fig. 4d and Tables 2 and 3) led to theoretical barrier estimate of 52.3 cm^{-1} against U_{eff} value of 35 cm^{-1} (see Table 3). However, the wave function of the ground KD turns out to be: $|\pm\frac{13}{2} >$: 0.93 $|\pm\frac{13}{2} >$ +0.31 $|\pm\frac{15}{2} >$+0.21 $|\pm\frac{11}{2} >$ with concomitant ground state crystal field parameter B_2^0 and g_{zz} as -2.47 and ~17, respectively, for **3** and these CF parameters are in agreement with the experimental results obtained from far-IR spectra recorded at low temperature [54]. As phthalocyanine ligands are capping the Dy^{III} ion above and below and these are not purely axial ligand that Dy^{III} enjoys, this leads to the stabilization of $|\pm\frac{13}{2} >$ as the ground state with strong mixing from the excited states. The difference in the U_{eff} and U_{cal} values is attributed to the difference in the structure employed; particularly, ab initio calculations are often performed on X-ray structure collected at 100 K while the precise spectroscopic measurements are performed at 5 K. The structural distortions, however small, are likely to influence the computed parameters and here in this example, variation of Dy-N distance by 0.05 Å found to rationalize the difference observed. This point is particularly important as often, ab initio calculations yield barrier heights which are larger than the ones estimated from experiments. While the accuracy of the theoretical level can be improved (using dynamic correlation and expanding the reference space), often

the difference is attributed to the difference in the structure and/or intermolecular effects that are not fully captured in the calculations.

For complex **4** (see Fig. 4e and Tables 2 and 3), ab initio calculations suggest a ground state of $|\pm M_J = \frac{11}{2}>$ and this has been substantiated by the estimated g-factors: $g_{xx} = 0.16$, $g_{yy} = 0.33$ and $g_{zz} = 19.24$. Furthermore, **4** displayed zero-field SIM characteristics with U_{eff} value of 37.8 cm^{-1} with respect to the U_{cal} of 67.2 cm^{-1} [47, 63]. Here, the geometry around Dy^{III} ion is distorted bicapped triangular prism with $\{DyO_6N_2\}$ core. Here, the average Dy-O distances are estimated to be 2.323 Å while the two Dy–N bonds are at ~2.580 Å suggesting strong oxygen donations from one side. Strong oxygen donations from one side and moderate nitrogen donations from the other side lead to the stabilization of $|\pm M_J = \frac{11}{2}>$ as the ground state with concomitant mixing with other states.

3.1.2 Ab Initio Studies on Category B Complexes: Field-Induced Dy^{III} Single Molecule Magnets Possessing $|\pm M_J = \frac{15}{2}>$ Ground State

There are several Dy^{III} SIMs/SMMs reported to possess the desired $|\pm M_J = \frac{15}{2}>$ ground state. However, the lack of strong axial interactions and/or moderate equatorial interactions leads to the absence of Ising type anisotropy. In those cases, mixing of the $|\pm M_J = \frac{15}{2}>$ with the excited states is expected to yield strong QTM behaviour at the ground state. Prominent QTM within the ground KD induces fast relaxation and deters the presence of SIM/SMM behaviour in zero field. Application of static *dc* field quenches the QTM propensity and promotes further relaxation via higher energy excited sublevels instilling SIM behaviour. In this section, we intend to compile such literature reports which display SIM behaviour only in the presence of certain applied *dc* field but possess the largest M_J ground state.

The first example in this group is complex **5** (see Tables 2 and 4). Complex **5** has been characterized to possess SIM behaviour in the presence of 1,500 Oe magnetic field. Calculations postulate U_{cal} value of 33 cm^{-1} against the spectroscopically (Luminescence) dictated first excited energy level located at 30 $\pm$3 cm^{-1} (see Table 4). The pronounced QTM contribution within the ground state is evident from the large calculated transverse anisotropy ($g_{xx} = 0.90$, $g_{yy} = 1.16$ and $g_{zz} = 17.82$) leading to faster relaxation in zero-field conditions. Application of field instigates SIM behaviour by quenching the QTM effects [64]. Complex **5** possesses Dy^{III} ion in nine-coordinated environment with five oxygen atoms from crown ether binding weakly above the Dy^{III} ion and four oxygen atoms binding strongly below, leading to pseudocapped square antiprism geometry (see Fig. 5a and Table 4). This is likely to yield strong mixing of states and the evident transverse anisotropy.

Complex **6** also has a $\{DyO_9\}$ core with prismatic geometry (see Fig. 5b and Tables 2 and 4) and exhibits f-SIM (using 1,000 Oe) behaviour with U_{eff} value of 6.1 and 22.2 cm^{-1}. Calculations reveal substantial transverse anisotropy in the ground

Table 4 List of complexes {from category B} with pertinent experimental energy barrier (U_{eff}, in cm^{-1}), ab initio computed energy barrier (U_{cal}, in cm^{-1}), main magnetic g factors and crystallographic structural information

	U_{eff}	U_{cal}	g_{xx}–g_{yy}	g_{zz}	Type of coordinated atoms	Structure	Ref.
5	30±3	33	0.90–1.16	17.82	9 O	Pseudocapped square antiprismatic	[64]
6	6.1, 22.2	73	0.26–0.81	18.81	9 O	Prismatic	[65]
7	44	111.8	0.01–0.02	19.61	9 O	Between spherical capped square antiprism and muffin	[66]
8	22.5	44.6	0.17–0.34	17.19	6 N, 4 O	Distorted bicapped square antiprismatic	[56]
9	<13.2	44.1	0.25–0.65	18.78	6 N, 4 O	Distorted bicapped square antiprismatic	[56]
10	53	64	0.2–0.9	18.6	4 O, 4 N	Square antiprismatic	[67]
11	16	188.9	0.03–0.05	19.48	8 O	Triangular dodecahedron	[47]
12	21.1	93.0	0.02–0.07	19.26	6 O, 2 N	Distorted bicapped triangular prism	[47]
13	19.7	77.3	0.63–0.66	16.09	8 N	Distorted cube	[47]
14	24.0	75.3	0.49–0.57	16.85	8 N	Distorted cube	[47]
15	28.5	109.1	0.01–0.03	19.69	6 O, 2 N	Distorted square antiprismatic	[47]
16	17	58.7	0.02–0.03	19.69	6 N	Trigonal prismatic	[47]
17	17.9	41.7	0.10–0.25	18.15	9 O	–	[68]
18	13.5, 36	46/43	0.07–0.18	19.49/ 19.56	7 O, 2 N	Intermediate between spherical capped square antiprism and spherical tricapped trigonal prism	[69]
18a	14.2, 35.9	64/43	0.03–0.09	19.58/ 19.57	7 O, 2 N	Intermediate between spherical capped square antiprism and spherical tricapped trigonal prism	[69]
19	3.8, 4.4, 12.3	52.3	0.62–2.38	17.21	9 O	Monocapped square antiprismatic	[70]
20	83	91	0.02–0.04	18.82	9 O	Distorted tricapped trigonal prismatic	[71]
20a	16	76, 46	0.02–0.04	19.44	10 O	Distorted bicapped square antiprismatic	[71]
21	42.0	89.8, 106.2	0.02–0.04	18.77	8 O	Distorted square antiprismatic	[72]
22	11.8, 41	104.5	0.02–0.04	19.78	2 N, 6 O	Triangular dodecahedron	[73]
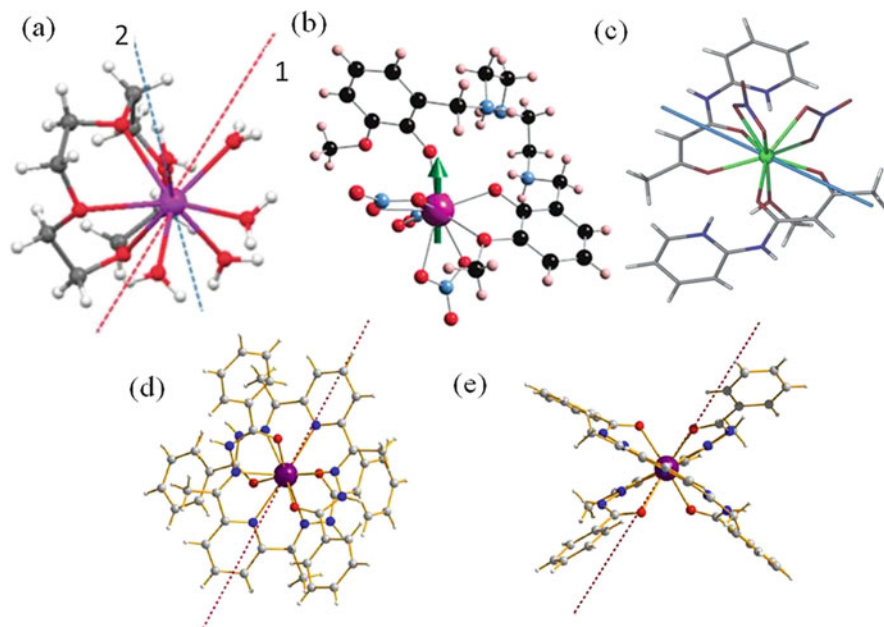
Fig. 5 (**a–e**) Molecular structures of complexes **5–9**, respectively, exhibiting computed g_{zz} axis. Arrows in complexes show the orientation of the principal magnetization axis. In complex **5**, second arrow shows the direction of KD2 g_{zz} axis. Colour code: central atom = Dy, red = O, dark blue/light blue = N, black/dark-brown/light-brown = C and white = H atoms. Reprinted from Gavey et al. [64], Ruiz et al. [65], Chilton et al. [66], Batchelor et al. [56] with permission from the Royal Society of Chemistry

KD ($g_{xx} = 0.26$, $g_{yy} = 0.81$ and $g_{zz} = 18.81$) explaining the experimental observation with the estimated U_{cal} value of 73 cm^{-1} (see Table 4). The ground KD (KD1) principal g_{zz} axis of complex **6** is in close proximity to Dy-O$_{phenolate}$ and normal to Dy-O$_{methoxy}$ bond (see inset Fig. 5b) [65]. Strong transverse anisotropy dictates strong QTM at the ground state and hence an optimum field of 1,000 Oe was required to quench the observed QTM effects.
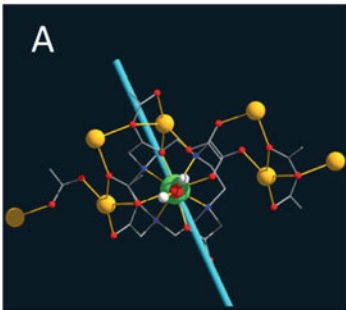
Complex **7** is also having {DyO$_9$} core with geometry that lies between a spherical capped square antiprism and a muffin shape (see Fig. 5c and Tables 2 and 4). Despite strong axiality ($g_{zz} = 19.61$, $g_{xx} = 0.01$ and $g_{yy} = 0.02$) in ground KD, complex **7** shows f-SIM (2,000 Oe) characteristics with U_{cal} and U_{eff} values estimated to be 111.8 cm^{-1} and 44 cm^{-1}, respectively [66]. The g_{zz} axis is found to lie between the β-diketonate ligands suggesting how coordinated nitrates play a role in determining the magnetic behaviour [66]. Presence of nitrate ions in **7** is discussed to govern the barrier for magnetization reversal.

Both complexes **8** and **9** have Dy^{III} ion in ten-coordinated distorted bicapped square antiprismatic geometry with {DyO$_4$N$_6$} core (see Fig. 5d, e and Tables 2 and 4). Both complexes are having almost identical structures except the deprotonated amino nitrogen of one of the ligands in complex **9**. Calculations on complexes **8** and **9** show U_{cal}/U_{eff} values of 44.6/22.5 cm^{-1} and 44.1/13.2 cm^{-1}, respectively

(a)

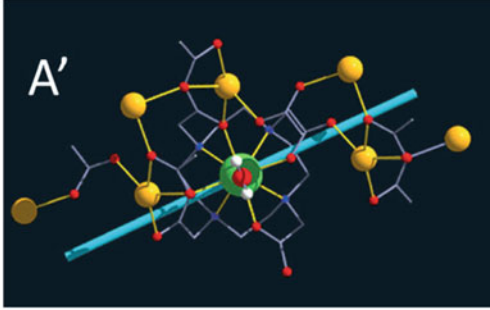| Angle of rotation H_2O	Basis set	Energy gap (cm^{-1})	g_1	g_2	g_3	Angle of the easy anisotropy axis
0	DZ	34	19.34	0.09	0.30	0.9
0	TZ	47	19.40	0.07	0.23	0.1
0	TZ-TZP	69	19.33	0.03	0.23	0.3
90	DZ	80	19.52	0.06	0.17	87.1
90	TZ	82	19.48	0.08	0.18	87.0
90	TZ-TZP	66	19.28	0.06	0.30	88.8


(b)   (c)

Fig. 6 (**a**) Tabular compilation to show dependence of magnetic anisotropy on the rotation of coordinated second coordination sphere water molecule in **10**. (**b**) Complex model of [Dy(DOTA)(H$_2$O)]$^+$ unit with three Na ions and few other modifications (model A) with their easy axis of magnetization represented by blue rod. (**c**) Water molecule of model A was rotated by 90° around Dy-O$_W$ axis in model A′. The corresponding blue rod indicates easy axis of magnetization. Colour code: central atom = Dy, red = O, brown = C and golden yellow = Na atoms. All the foregoing pictures were reprinted from Cucinotta et al. [67] with permission from John Wiley and Sons

[56]. Inherently two shorter bonds in **9** impose greater distortions in **9** compared to **8**. Larger transverse anisotropic components (g_{xx}, g_{yy}) can be ascribed to the smaller barrier in **9** compared to **8**. In **8**, the KD1-g_{zz} is linked to the idealized fourfold symmetry and aligns along the coordination bond Dy-N(pyridyl). However, in **9** simple deprotonation of the ligand resulted in rotation of such orientation by 60° towards Dy-O(carbonyl) bond.

Complex **10** has a {DyO$_4$N$_4$} core with capped square antiprism geometry. Calculations on **10** yields U_{cal} value of 64 cm^{-1} and absence of axial symmetry in the estimated g-tensors (see Fig. 6 and Tables 2 and 4). Calculations were undertaken on several models to appraise the genesis of different orientation of g_{zz} axis upon removal of coordinated water molecules. To profusely understand this behaviour, coordinated water molecules were rotated at different angles and several basis sets were also attempted. This revealed crucial role of second coordination sphere atoms (water molecule in **10**) to fine-tune magnetic anisotropy. This attributes to the partial charge transfer from the ligand atoms to the Dy^{III}-5d orbitals. Furthermore, water molecule rotation could impact the relative population of Dy^{III}-5d orbitals through π interaction with the O atom [67].

Complexes **11–16** are f-SIMs with U_{eff}/U_{cal} values 16/188.9, 21.1/93, 19.7/77.3, 24/75.3, 28.5/109.1 and 17/58.7 cm^{-1}, respectively (see Tables 2 and 4 for
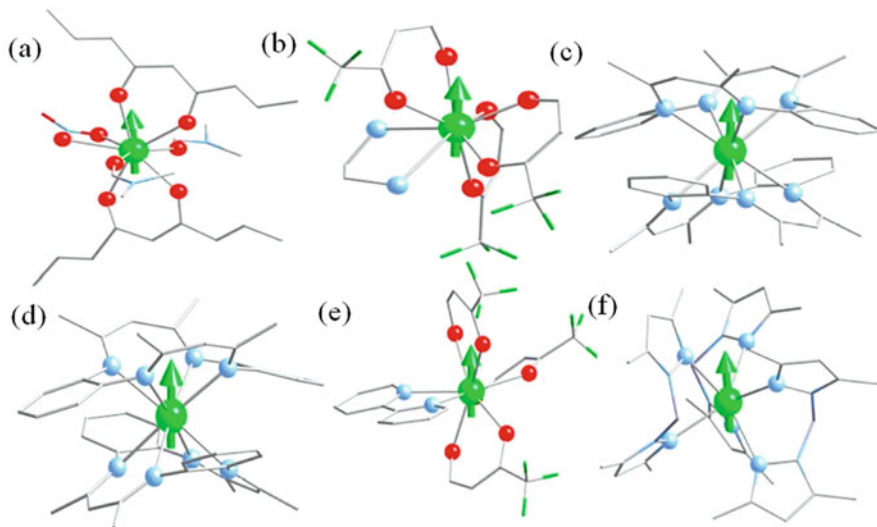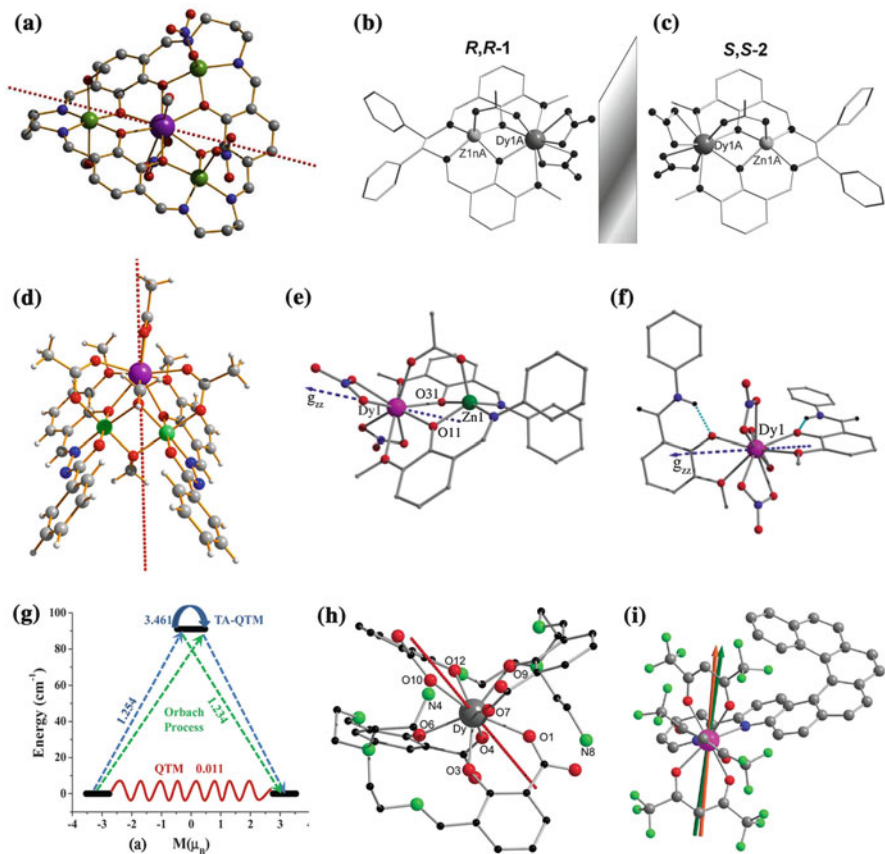
Fig. 7 (**a–f**) Molecular structures of complexes **11–16**, respectively. Arrows in complexes show the orientation of the principal magnetization axis. Colour code: central atom = Dy, red = O, light blue = N, white = C and green = F atoms. Reprinted with permission from Aravena and Ruiz [47] Copyright@2013 American Chemical Society

molecular formula, *g*-factors and structural information) [47]. Complexes **11–15** are having eight coordination numbers around central Dy^{III} ion with $\{DyO_8\}$ core in complex **11**, $\{DyO_6N_2\}$ core in complexes **12** and **15** and $\{DyN_8\}$ core in complexes **13** and **14**. Complex **16** has six coordination numbers around central Dy^{III} ion with $\{DyN_6\}$ core (see Fig. 7). Complexes **13** and **14** render two high-potential islands in the opposite regions of the sphere, with small potential in equatorial region due to pertinent shapes. This leads to accommodation of beta electron density in the equatorial region resulting in lower g_{zz} values (~16) (see Table 4). Complexes **13–15** are computed to possess close-lying first and second excited spin-free energies after incorporation of SOC. This is not ideal as one would require close-lying first excited state and relatively high-lying second excited spin-free energies to obtain axial g-tensors for the ground state. Due to these reasons, complexes **13–15** exhibit f-SIM behaviour [47].

The Zn^{II} ion has an electronic configuration $3d^{10}4s^0$ and is non-magnetic. Hence, Zn^{II} ion containing Dy^{III} complexes enacts equivalent to Dy^{III}-based mononuclear complex. Incorporation of diamagnetic ion leads to increment in barrier as they: (a) attenuate intermolecular magnetic coupling and (b) exert strong polarization effect on ligand donor atoms to impose greater negative charge. Complex **17**, in which Dy^{III} ion is nine-coordinated, $\{DyO_9\}$, is with neighbouring Dy ... Dy ions that are about 10 Å apart. This large Dy ... Dy separation is expected because of the presence of three diamagnetic Zn^{II} ions in the molecule. It possesses narrower window range of eight KDs spanning within 391 cm^{-1}. This owes to relatively longer Dy-O bonds (in avg. 2.44 Å) in **17**. KD1 in **17** is not exactly axial (substantial

Fig. 8 (**a–f**, **h–i**) Molecular structures of complexes **17–22**, respectively and (**g**) ab initio calculated magnetization relaxation mechanism in **20**. Arrows in complexes show the orientation of the principal magnetization axis. In complex **22**, two arrows show the direction of experimental and computed KD1 g_{zz} axis. Colour code: central atom = Dy, red = O, dark blue/light blue = N, black/dark-brown/light-brown = C and green = Zn atoms. In complexes **21** and **22**, small green balls represent nitrogen atoms. Reproduced from Long et al. [69] with permission from John Wiley and Sons. Reprinted with permission from Xue et al. [70] Copyright@2014 American Chemical Society. Reprinted with permission from Bhunia et al. [72] Copyright@2012 American Chemical Society. Reprinted from Upadhyay et al. [71], Ou-Yang et al. [73] with permission from the Royal Society of Chemistry

transverse g_{xx}, g_{yy} components; see Table 4) and the main anisotropy axis of Dy^{III} ion is parallel to the plane constituted by the three Zn^{II} ions (see Fig. 8a) [68].

Next two enantiomeric complexes **18** and **18a** (R,R-1 and S,S-2, respectively) show U_{eff}/U_{cal} values of 13.5(36)/46 and 14.2(35.9)/64 cm^{-1}, respectively. Both enantiomers have non-coordinated ligand field environment around Dy^{III} ion with an intermediate geometry between a spherical capped square antiprism (C$_{4v}$) and a spherical tricapped trigonal prism (D$_{3h}$, see Fig. 8b, c and Tables 2 and 4). The

Dy ... Dy intermolecular distance is found to be 9.21 Å. Larger transverse aniso-tropic components in KD1 induce relatively large transversal Zeeman splitting of the corresponding KDs that instigate QTM in **18/18a**. This justifies their pertaining f-SIM behaviour of **18** and **18a** [69]. Molecular structures for both the enantiomers show an electrical bistability up to 563 K, one of the highest reported for any molecular ferroelectric materials.

Similar to Zn^{II}, Co^{III} is also diamagnetic and Co^{III} containing Dy^{III} complexes can also be approximated as Dy^{III}-based SIM as whole paramagnetism arises from single Dy^{III} ion. One such example is complex **19**, which has a defective cubane shaped heterometallic trinuclear $\{Co^{III}_2Dy^{III}\}$ metallic centres (see Fig. 8d and Tables 2 and 4). Calculations on complex **19** articulate non-axial nature of ground and first excited KDs and this can be attributed to the nature of the crystal field of the ground energy multiplet. Axial crystal field parameters (B_2^0, B_4^0 and B_6^0) are estimated to be relatively weaker than the non-axial CFPs of the ground manifold $|M_J = \frac{15}{2} >$ of the Dy^{III} centre. This provokes faster QTM within the ground KD and instigates spin flipping by direct process within ground multiplet than the Orbach process involved in the excited state. In resemblance to **17**, crystal field splitting of ground $^6H_{15/2}$ multiplet of Dy^{III} is relatively narrow (454 cm^{-1}) as a result of longer Dy-O bonds (2.41 Å). Ab initio calculated first excited state of Dy^{III} ion is located at ~50 cm^{-1} (see Table 4) and this is larger than the barrier height obtained from *ac* experiment (U_{eff}). This reveals that the real thermally activated regime is out of the *ac* frequency window tested and for complex **19**, relaxation is mainly governed by quantum tunnelling. Therefore, non-axial anisotropy of Dy^{III} and intermolecular dipolar interaction between the nearest neighbours ($d_{Dy...Dy} = 8.15$ Å) promote QTM and quench the QTM behaviour in the absence of magnetic field. This contributes to the observation of SIM behaviour in **19** only in the presence of magnetic field [70].

Complexes **20** and **20a** are heterodinuclear $\{Zn^{II}Dy^{III}\}$ and mononuclear Dy^{III} complexes, respectively, with f-SIM behaviour. The U_{eff} for both complexes are found to be 83 cm^{-1} and 16 cm^{-1}, respectively. The Dy^{III} ion in both the complexes is found to have $\{DyO_9\}$ core with distorted tricapped trigonal prismatic geometry (see Fig. 8e, f and Tables 2 and 4). KD1 of **20** and **20a** is computed to be axial in nature though it lacks pure Ising nature. Presence of diamagnetic Zn^{II} ion is found to pose increment in the magnitude of energy barrier for **20** compared to **20a**. QTM propensity within KD1 of **20a** is relatively higher than **20** due to reduced axiality in **20a**. Calculations iterate $|\pm M_J = \frac{13}{2} >$ and $|\pm M_J = \frac{1}{2} >$ nature of the first excited KD (KD2) in **20a** and **20**, respectively. This is further corroborated by computed transversal magnetic moment matrix element pertaining to TA-QTM within the KD2 as 3.46 and 0.02 μ_B in **20** and **20a**, respectively (see Fig. 8g). Bridging phenoxo O atoms in **20** are estimated to possess higher negative charges than **20a** (-0.73 vs. -0.30 for **20** and **20a**, respectively). Diamagnetic Zn^{II} ion is expected to induce stronger polarization on the O atom and cumulatively instills larger electrostatic interaction on Dy^{III} ion. This causes the excited state destabilization and enhanced KD1–KD2 energy gap. This articulates the crucial presence of diamagnetic cation in

the coordination vicinity of lanthanide to promote larger energy barrier [71]. Previous studies performed by some of us suggest that diamagnetic replacement of Co^{III} ion with K^I, Zn^{II} and Ti^{IV} ions induces larger formal charge on the bridging O atoms, causing large separation between ground to first excited state. Within these set of models, the ab initio analysis gives the U_{cal} values in the order of $K^I > Zn^{II} > Co^{III} > Ti^{IV}$, suggesting that with decrease in the oxidation state of the diamagnetic ion, the electronic repulsion to the bridging atoms increases, causing increase in the U_{cal} values and decrease in the QTM probability [74].

Another example for this family of molecule is complex **21**, where Dy^{III} ion is in eight-coordination environment with distorted square antiprism geometry (see Fig. 8h and Tables 2 and 4). KD1 in **21** is computed to be axial and calculations on **21** articulate that the H ion positions lead to uncertainty in the direction of anisotropy axis [72]. Intermolecular magnetic coupling constant for complex **21** is found to be very small, due to very large Dy ... Dy separation (~10 Å) and the upward turn for susceptibility plot at low temperature are estimated by virtue of strong dipolar interaction.

Recently, Guennic et al. have reported a helicene based Dy^{III} single-ion magnet, complex **22** (see Fig. 8i and Tables 2 and 4). Both the racemic and enantiomerically pure forms for complex **22** are acting as SIMs in their crystalline phase. In complex **22**, $\{DyN_2O_6\}$ core is in a triangular dodecahedron environment. KD1 in **22** shows Ising anisotropy with large g_{zz} value and this orients along the most negative charged direction of the coordination polyhedron. The computed and experimental g_{zz} lies at 3.5° against each other's alignment. Accounting the antiferromagnetic intermolecular dipolar coupling for **22**, nice agreements between experimental and calculated magnetic data have been demonstrated [73].

3.1.3 Ab Initio Studies on Category C Complexes: Zero-Field Single-Ion Magnet Complexes Possessing $|\pm M_J = \frac{15}{2} >$ Ground State with the First Excited State Lying Within ~50 cm^{-1}

Foregoing section demonstrated complexes showing SIM characteristics only in the presence of applied magnetic field. Here, we shift our attention towards complexes which exhibit SIM behaviour in zero field but yet have concomitant low-lying first excited state. In this regard, we have selected three reported complexes (**23–25**). Complex **23** has nine-coordinated pseudocapped square antiprismatic geometry with $\{DyO_9\}$ core (see Fig. 9a). *AC* magnetic studies for complex **23** suggest two U_{eff} values for relaxation (34.0 and 19.0 cm^{-1}). Well-separated ground (±1), first (±2) and second excited (±3) states were noted through calculations on **23**. Energy gap between ground to first excited state is found to be 58 cm^{-1} which is larger than the U_{eff} value estimated. The transversal magnetic moments in **23** deviate from the Ising limit of anisotropy ($g_{zz} = 20$, $g_{xx} = g_{yy} = 0$) and possess transverse anisotropy. This validates the experimentally noted *ac* magnetic data of fast relaxation mechanism. The two closely lying U_{eff} values (see Tables 2 and 5) are well validated by operative
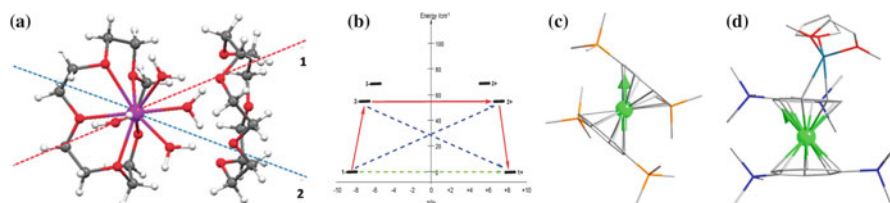
Fig. 9 (**a**, **b**) Molecular structure for complex **23** along with its ab initio calculated magnetization relaxation mechanism. (**c**, **d**) Molecular structures for complexes **24** and **25**, respectively. Arrows in complexes show the orientation of the principal magnetization axis. Colour code: central atom = Dy, red = O, dark blue = N, black/dark-brown/light-brown = C, golden yellow = Si and white = H atoms. Reprinted from Gavey et al. [64] with permission from the Royal Society of Chemistry. Reprinted with permission from Aravena and Ruiz [47] Copyright@2013 American Chemical Society

Table 5 List of complexes (from category C) with pertinent experimental energy barrier (U_{eff}, in cm^{-1}), ab initio computed energy barrier (U_{cal}, in cm^{-1}), main magnetic g factors and crystallographic structural information

	U_{eff}	U_{cal}	g_{xx}–g_{yy}	g_{zz}	Type of coordinated atoms	Structure	Ref.
23	19, 34	58	0.26–0.52	17.49	9O	Pseudocapped square antiprismatic	[64]
24	12	36.3	0.14–0.18	15.95	(Two COT^{2-} in η^8-fashion)	–	[47]
25	17	45.6	0.02–0.07	16.90	(Two COT^{2-} in η^8-fashion)	–	[47]

QTM and Orbach mechanisms via KD1 and KD2, respectively (green and blue dashed lines, respectively, in Fig. 9b) [64]. In complexes **24–25**, Dy^{III} ion is sandwiched between alkyl substituted η^8-COT ligands (see Fig. 9c, d, respectively). Complexes **24–25** exhibit U_{eff}/U_{cal} values of 17/45.6 cm^{-1}, 12/36.3 cm^{-1}, respectively (see Table 5). Complexes **24–25** can be taken as an exception to zf-SIM complexes. The zf-SIM complexes are essentially known to be associated with small KD1 g_{xx}, g_{yy} components. However, contrastingly complexes **24–25** have considerable transverse anisotropy components and show low barriers which are sensitive to external *dc* magnetic field. This accentuates substantial contribution of KD1 tunnelling as well as QTM contribution to the magnetic relaxation. In these two complexes, the beta electron density is accommodated in equatorial region resulting in smaller g_{zz} values for KD1 in **24–25** (~16, see Table 5) [47].

3.1.4 Ab Initio Studies on Category D Complexes: Zero-Field Single-Ion Magnet Complexes Possessing $|\pm M_J = \frac{15}{2} >$ Ground State with First Excited State Lying Within ~100 cm^{-1}

In this section, we intend to summarize the zf-SIMs with concomitant first excited energy multiplet located within ~100 cm^{-1}. Thus, the ligand structures described here have stronger axial interactions than the ones described in the earlier section. Suitable examples of this category include complexes **26–31** (see Fig. 10 and Tables 2 and 6). KD1 of complexes **26–31** is of Ising type with g_{zz} ranging from 19.24 to 19.60 (concomitant smaller g_x, g_{yy} values; see Table 6). Complex **28** has dodecahedron geometry with {DyO$_8$} core whereas other five complexes (**26**, **27**, **29–31**) are having distorted square antiprismatic geometry with {DyN$_2$O$_6$} core. Calculations on complex **28** rendered axially compressed shape equal to a disc with its g_{zz} being perpendicular to the beta electron plane. Complexes **26–30** estimated to possess smaller first excited and larger second excited spin-free energies (after the SOC coupling incorporation in contrary to that discussed in Sect. 3.1.2). Calculations on models of complex **28** with ligands of versatile charge distribution affirm correlation between large anisotropy of the crystal electrostatic potential and

Fig. 10 (**a–c**) Molecular structure for complexes **26–28**. (**d, e**) Molecular structure for complexes **29a–b**. (**f**) Molecular structure for complex **30**. (**g–h**) Molecular structure for complexes **31a–b**. Reproduced from Aravena and Ruiz [47], Baldovi et al. [48] Copyright@2013 American Chemical Society. Arrows in complexes show the orientation of the principal magnetization axis. Colour code: central atom = Dy, Yellow = S, red = O, light blue = N, white = C and green = F atoms
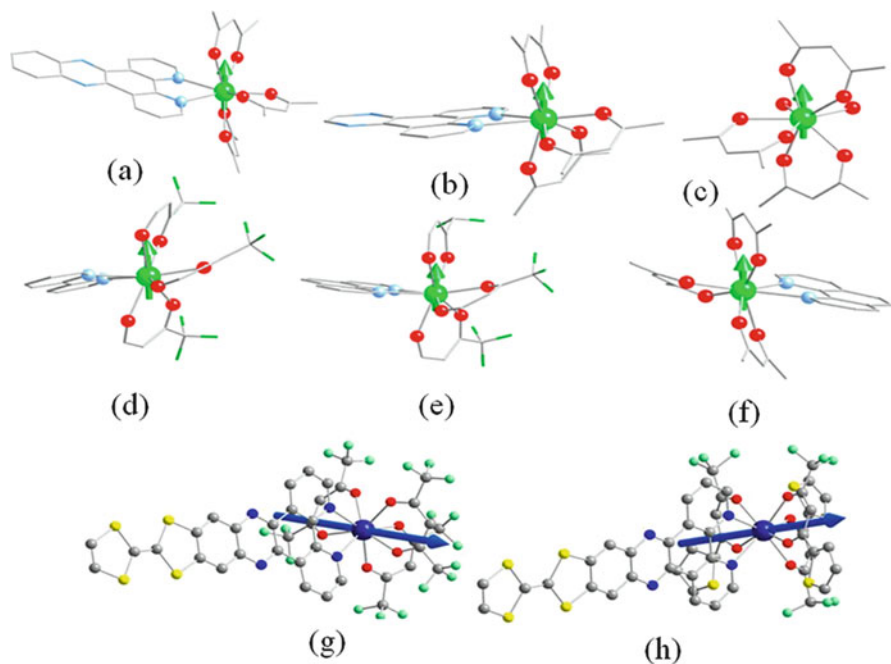
Table 6 List of complexes (from category D) with pertinent experimental energy barrier (U_{eff}, in cm^{-1}), ab initio computed energy barrier (U_{cal}, in cm^{-1}), main magnetic g factors and crystallographic structural information

	U_{eff}	U_{cal}	g_{xx}–g_{yy}	g_{zz}	Type of coordinated atoms	Structure	Ref.
26	94	120.4	0.00–0.01	19.24	6 O, 2 N	Distorted square antiprismatic	[46]
27	130	146.2	0.01	19.37	6 O, 2 N	Distorted square antiprismatic	[46]
28	45.9	151.9	0.01	19.46	8 O	Distorted square antiprismatic	[46]
29a	44.4	135.8	0.00	19.39	6 O, 2 N	Distorted square antiprismatic	[46]
29b	40	142.6	0.00	19.60	6 O, 2 N	Distorted square antiprismatic	[46]
30	59	126.3	0.01	19.51	6 O, 2 N	Distorted square antiprismatic	[46]
31a	27.1	–	0.08–0.11	18.89	6 O, 2 N	Distorted square antiprismatic	[51]
31b	44.3	–	0.00	19.58	6 O, 2 N	Distorted square antiprismatic	[51]
32	34.8	95	0.0–0.01	18.10	4 N, 6 O	Distorted bicapped square antiprismatic	[62]
33	14.6, 70.2	103.6	0.01	19.66	2 N, 6 O	Triangular dodecahedron	[73]
34	NA	117	0.02	19.47	2 N, 6 O	Distorted square antiprismatic	[75]
35	97.3, 103	129.0	0.00	19.43	8 O	Distorted square antiprismatic	[46]
36	67.3, 89.4	92.4	0.02–0.04	19.57	9 O	Distorted muffin	[76]

heteroleptic systems (combination of charged and neutral ligands). In these desired instances, beta electron density of Dy^{III}-4f electrons have propensity to concentrate into axially compressed shape. The Dy^{III}-4f beta electron density should preferentially be located along the direction of the minimum electrostatic potential of the sphere to deter proximity with the negatively charged ligands and minimize electrostatic repulsion with them [47]. Complexes **31a–b** are having identical coordination geometry but different ligand system. Large point charge of the first neighbouring atoms causes large separation between ground to first excited state for the latter molecule compared to the former one [51].

Complex **32** is similar to complex **1** with a minor modification. Complex **32** has two imino groups instead of amine groups. KD1 in complex **32** is computed to be pure Ising type (see Table 6). Experimental magnetic data was nicely reproduced harnessing ab initio computed values. Principal magnetization axis in **32** lies along the direction perpendicular to the pseudo-C$_2$ (along the N–N bond vector) axis and
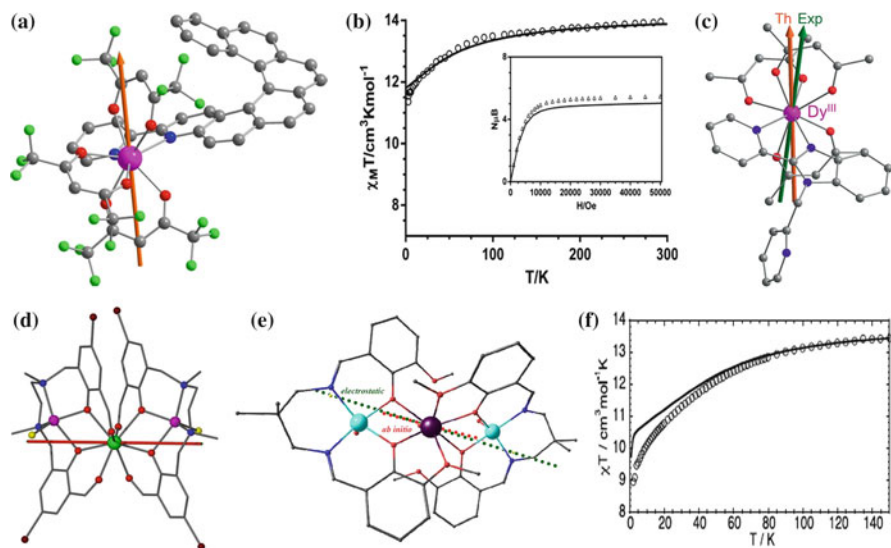
Fig. 11 (**a**, **c–e**) Molecular structures for complexes **33–36** and (**b**, **f**) χ_mT vs. T plot for **33** and **36**, respectively, solid line postulates calculated data. Arrows in complexes show the orientation of the principal magnetization axis. In complex **34**, two arrows show the direction of experimental and computed KD1 g_{zz} axis. Colour code: central atom = Dy, red = O, dark blue/light blue = N, black/dark-brown/light-brown = C, pink = Zn and green = Cl atoms. Reprinted from Ou-Yang et al. [73] with permission from the Royal Society of Chemistry. Reproduced from Jung et al. [75], Oyarzabal et al. [46] with permission from John Wiley and Sons

passes through the two –O atoms. Ising type ground state anisotropy in KD1 owes to shorter imine bonds (which corresponds to previous g_{zz} orientation) and the resultant stronger bonds in the axial direction cumulatively constitute favourable strong ligand field [62].

Complexes **22** and **33** are the same except that complex **22** is the racemic form whereas complex **33** is the enantiopure form. Pure Ising type anisotropy was detected in complex **33** with theoretical barrier estimated to be 103.6 cm^{-1} (see Fig. 11a and Tables 2 and 6). Accounting the positive intermolecular dipolar exchange interaction, nice agreement was found between experimental and calculated magnetic data (see Fig. 11b, contrary to its corresponding racemic analogue **22**) [73]. Complex **34** has {DyN$_2$O$_6$} core with distorted square antiprism geometry (D$_{4d}$ symmetry). Easy axis of the Dy^{III} ion lies along the most negatively charged direction. Computations on complex **34** invoke pure Ising type KD1 anisotropy with g_{zz} of 19.47 (see Fig. 11c and Tables 2 and 6) [75]. Complex **35** is having square antiprism geometry with {DyO$_8$} core. KD1 is markedly axial (g_{zz} = 19.43, Fig. 11d and Tables 2 and 6) with vanishing transversal g anisotropies in compliance with zf-SIM characteristics of **35**. Like in earlier instances, in **35** as well the calculated magnetic data matches well with the experiments. It shows zero-field SIM behaviour with U_{eff} value 97 cm^{-1} and this is smaller compared to ab initio calculated U_{cal}

value (129 cm^{-1}). KD1-g_{zz} in **35** is located between the planes constituted by two Dy-O-Zn-O moieties and collinear with the shortest Dy-O bond (2.25 Å) vectors while perpendicular to oblate shaped electron density. This reiterates the necessary requirement for axially strong coordination atmosphere to improve SIM behaviour in Dy^{III}-based complexes. In resemblance to the earlier statement, KD1-g_{zz} is located in such direction to evade strong electrostatic repulsion. Notably, alignment of principal magnetization axis acquired via electrostatic approach [42] complies well with that computed harnessing ab initio calculations [46]. In complex **36**, central Dy^{III} ion is surrounded by two Zn^{II} ions. It has a nine-coordinated {DyO$_9$} core with distorted muffin geometry (Fig. 11e and Tables 2 and 6). Eight KDs in complex **36** span up to 458 cm^{-1} with subsequent excited states lying even higher in energies. KD1 is of pure Ising type and beyond this, the g_{zz} value begins to reduce until fifth KD. However, beyond fifth KD, the g_{zz} value again starts to increase and at eighth KD, the highest g_{zz} is achieved. This indicates the low-symmetry nature of complex **36**. KD1 magnetic moment lies in close proximity to the two shortest Dy-O bond and ligand donor atoms with greater electron density in compliance with the oblate–prolate model. Using the ab initio computed anisotropy and crystal field parameters, experimental magnetic data is nicely reproduced with intermolecular interaction of −0.0024 cm^{-1} (see Fig. 11f). Ising ground state was corroborated by the transversal magnetic moment matrix element corresponding to the KD1, QTM process (~10^{-3} μ_B). The matrix element pertaining to the direct (Orbach) process implicating ±1 and ±2 energy states (1.73 μ_B) induces relaxation via KD2 providing theoretical barrier estimate of 92.4 cm^{-1}. Wave-function analysis postulated KD1 to be predominantly $|\pm\frac{15}{2}>$: 0.98 $|\pm\frac{15}{2}>$ while KD2 is preponderantly $|\pm\frac{13}{2}>$: 0.37 $|\pm\frac{13}{2}> +0.25 |\pm\frac{11}{2}> +0.35 |\pm\frac{9}{2}>$. DFT calculations on complex **36** articulate larger negative charges on the phenoxo O atoms as induced by the strong polarization effect of Zn^{II} ions. In order to probe the role of secondary coordination sphere influence in U_{cal} values, water ligand coordinated to two Zn^{II} ions in **36** was substituted by different halide ligands (F$^-$, Cl$^-$, Br$^-$ and I$^-$). In all the substituted models, Ising type ground multiplet was detected and U_{cal} diminishes with the expected electronegativity of the halide ion [76].

3.1.5 Ab Initio Studies on Category E Complexes: Zero-Field Single-Ion Magnet Complexes Possessing $|\pm M_J = \frac{15}{2} >$ Ground State with First Excited State Energy Separation >100 cm^{-1}

In this category **E**, we will describe the properties of Dy^{III} SIMs possessing $|\pm M_J = \frac{15}{2} >$ ground state with strong crystal field splitting (first excited state lying at >100 cm^{-1}) and exhibiting zero-field SMM characteristics. First complex under this category is complex **37**, which has {DyO$_8$} core with trigonal dodecahedron geometry. KD1 of **37** is found to be pure Ising type with subsequent excited multiplets lying higher in energy (see KD1-g_{zz} orientation in Fig. 12a and Tables 2 and 7). The main magnetic axes of the lowest three KDs in **37** are almost parallel and are
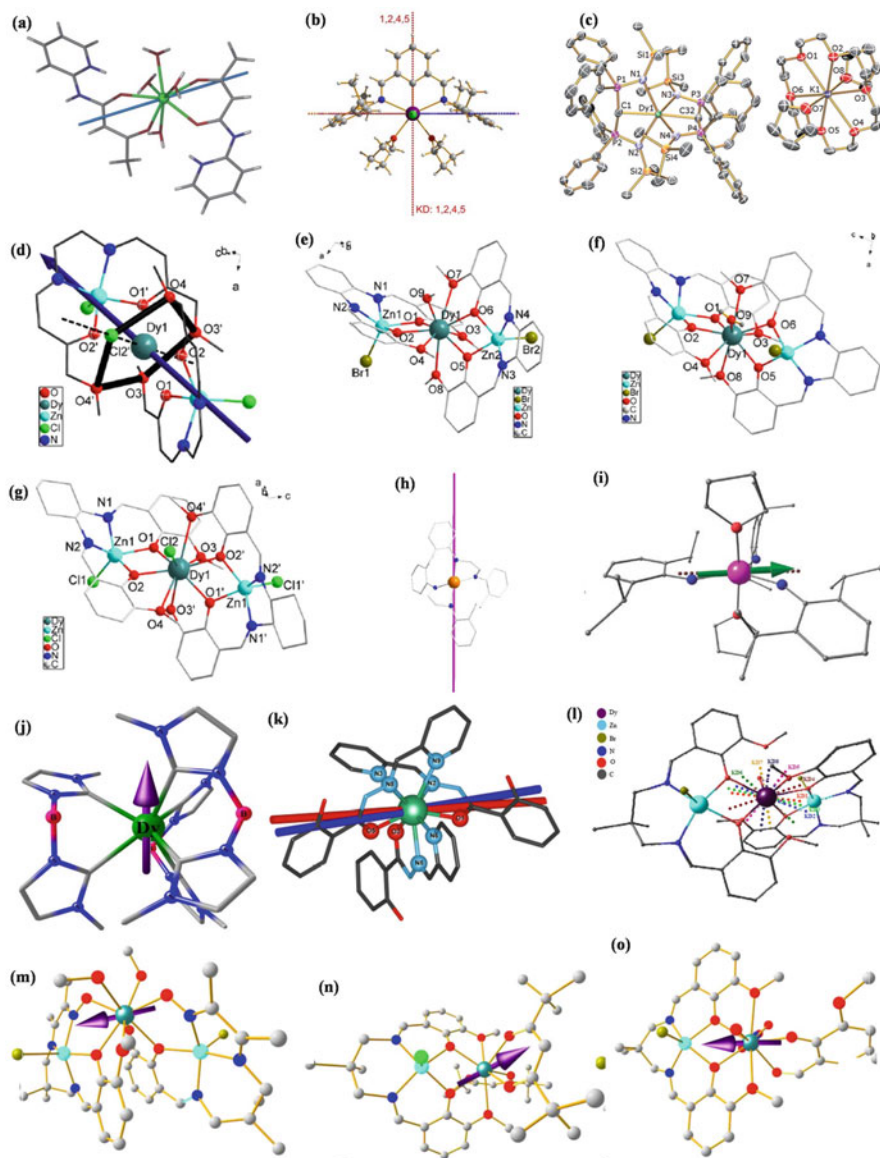
Fig. 12 (**a–o**) Molecular structures along with ground state KD orientation for complexes **37–48**, **50–52**, respectively. Arrows in complexes show the orientation of the principal magnetization axis. Complexes with two arrows are showing KD1 and KD2 g_{zz} axis, and complexes with eight arrows are showing KD1–KD8 g_{zz} axis. Colour code: central atom = Dy, red = O, dark blue/light blue = N, black/dark-brown/light-brown/white = C, cyan = Zn, light yellow = Br and green = Cl atoms. Reprinted from Chilton et al. [66], Gregson et al. [77], Sun et al. [78], Long et al. [79], Rajaraman et al. [80], Gupta et al. [81], Kishi et al. [82] with permission from the Royal Society of Chemistry. Reproduced from Lucaccini et al. [83] with permission from John Wiley and Sons. Reprinted from Liu et al. [18], Chen et al. [19], Costes et al. [84] Copyright@2016 American Chemical Society

Table 7 List of complexes {from category E} with pertinent experimental energy barrier (U_{eff}, in cm^{-1}), ab initio computed energy barrier (U_{cal}, in cm^{-1}), main magnetic g factors and crystallographic structural information

	U_{eff}	U_{cal}	$g_{xx}-g_{yy}$	g_{zz}	Type of coordinated atoms	Structure	Ref.
37	124	249.2	0.05–0.07	16.33	8 O	Trigonal dodecahedral	[66]
38	233, 270	266	~10^{-4}– 10^{-3}	19.81	2 N, 2 O, 1 C, 2 Cl	–	[55]
39	501.1, 565	515.7, 563	0.00	19.88	4 N, 2 C	–	[77]
40	299/ 334.3/ 301.6	355.6	0.00	19.96	8 O, 1 Cl	Muffin	[78]
41	161.9	351.8	0.00	19.85	9 O	Muffin	[78]
42	84.1	313.0	0.00	19.79	9 O	Spherical capped square antiprismatic	[78]
43	276.6	351.9	0.00	19.97	8 O, 1 Cl	Muffin	[78]
44	30/43/ 108	410.7	0.00	19.71	4 N	Tetrahedron	[79]
45	23	199.0	0.00– 0.001	19.67	3 N, 2 O	Trigonal bipyramidal	[80]
46	32.8, 33.6	268.5	0.07–0.09	19.91	6 N incorporation of agostic interactions with three Hs	Trigonal prismatic; incorporation of agnostic interactions with H: Tricapped trigonal prismatic	[81]
47	230	237	0.00	19.80	6 N, 3 O	Spherical capped square antiprismatic	[83]
48	102, 149.2	218.1	0.00	19.91	9 O	Distorted spherical tricapped trigonal prismatic	[76]
49	101.5, 140.7	238.5	0.00	19.94	9 O	Distorted spherical tricapped trigonal prismatic	[76]
50	82.9, 146.7	177.5	0.00	19.94	9 O	Distorted muffin	[84]
51	69.3, 111.5	159.9	0.00	19.73	8 O	Distorted biaugmented trigonal prismatic	[84]
52	44.3, 66.4	131.3	0.00	19.71	8 O	Distorted triangular dodecahedron	[84]
53	1,277	1,156	0.00	19.88	– (Sandwich type between two substituted – Cp rings)	Bent metallocene	[22]

(continued)

Table 7 (continued)

	U_{eff}	U_{cal}	g_{xx}–g_{yy}	g_{zz}	Type of coordinated atoms	Structure	Ref.
54	1,223	1320.7	0.00	19.99	– (Sandwich type between two substituted – Cp rings)	Bent metallocene; approximately eclipsed two –Cp rings	[21]
55	66.7	362.0	0.00	19.56	2 N, 6 O	Distorted square antiprismatic	[82]
56′	45.2	197.0	0.01	19.44	2 N, 6 O	Distorted square antiprismatic	[82]
57	328.0	299	0.00	19.86	7 O	Compressed pentagonal bipyramid	[19]
58	377.4	276	0.00	19.88	7 O	Compressed pentagonal bipyramid	[19]
58	492	586	0.00	19.87	1 Cl⁻, 2 O, 4 N	Distorted pentagonal bipyramid	[19]
59	712	721	0.00	19.88	1 Br⁻, 2 O, 4 N	Distorted pentagonal bipyramid	[18]
60	305	289.9	0.00	19.87	7 O	Axial pentagonal bipyramidal	[85]
61	1261.4	1,220	0.00	19.89	5 N, 2 O	Distorted pentagonal bipyramid	[86]
62	452.4, 511.1	478.4	0.00	19.86	7 O	Distorted pentagonal bipyramid	[20]
63	353.1	297	0.00	19.88	7 O	Distorted pentagonal bipyramid	[87]

deviating from KD1 by ~2° and 1.4°, respectively. However, the g-tensors of the two highest energy multiplets differ with respect to KD1 by 111.4° and 73.6°, respectively, and divert by 40.3° with respect to each other. The computed axial anisotropy is located between the two β-diketonate ligands and is collinear with the plane constituted by four water molecules to minimize the electrostatic repulsion with the U_{eff} value reported to be 123 cm^{-1} [66]. Next complex in this category is **38** with seven-coordinate Dy^{III} possessing pentagonal bipyramidal geometry with two N donors, two O donors, two chloride donors and one carbon donor from the pincer ligand. The calculated main anisotropy axis passes along the main symmetry axis and is collinear with shorter Dy-C bond vector (2.39 Å). Besides, the crucial role of C atom in dictating the orientation of KD1-g_{zz} arises from its inherent negative charge (−1.17) in its carbanionic form. Collinearity between the g_{zz} axes of KD1 and KD2 promotes relaxation via second excited multiplet (KD3) with U_{cal} value of 262 cm^{-1}. Furthermore, significant matrix element between ±3 multiplets (3.4 μ$_B$) pertaining to the TA-QTM process corroborates the relaxation probability via that

level. Significant anisotropies in KD1 and KD2 can be supported by computed huge negative axial CFP B_2^0 (-2.95). Additionally, the B_2^2 term is also estimated to be large (2.09) and this explains the huge anisotropy observed in complex **38** (see the KD orientations in Fig. 12b and Tables 2 and 7). The term B_2^2 is computed to be the largest when the quantization axis lies parallel to the main magnetic axis of KD3, passing along Cl-Dy-Cl bond vector [55].

Complex **39** is having six-coordinated distorted octahedral geometry with {DyC$_2$N$_4$} core. Linear coordination mode of the two methanediide (huge negative charge on the axis) sites in **39** assures considerable energy gap between $|\pm M_J = \frac{15}{2} >$ and other KDs. Notably, the three lowest KDs are pure $|\pm\frac{15}{2} >$, $|\pm\frac{13}{2} >$ and $|\pm\frac{11}{2} >$ states which are quantized along the main C=Dy=C axis. This suppresses relaxation via second and third excited KDs and promotes relaxation via higher energy levels. Wave-function analysis asserted fourth and fifth KDs to be composed of different mixed $|\pm M_J>$ levels, i.e. $|\pm\frac{9}{2}>$, $|\pm\frac{7}{2}>$, $|\pm\frac{5}{2}>$, $|\pm\frac{3}{2}>$ and $|\pm\frac{1}{2}>$. Additionally, perpendicular orientation of fourth and fifth KDs g_{zz} axis with respect to ground KD preferentially induces relaxation via those states. This outlines U_{cal} value to be 516 and 563 cm^{-1} (see Tables 2 and 7, and Fig. 12c for magnetization relaxation mechanism) which is very close to the estimated U_{eff} value (501 cm^{-1} and 565 cm^{-1}). Besides possessing a large U_{cal} value, the molecule also characterized to possess very large blocking temperature T_B of 10 K and this is among the best blocking temperatures reported for lanthanide based SIMs [77].

Next set of complexes that are discussed are nine-coordinate Dy^{III} complexes (**40–43**, see Fig. 12d–g). Complexes **40**, **41** and **43** are having muffin geometry whereas complex **42** has spherical capped square antiprismatic geometry with {DyO$_8$Cl} core for complexes **40** and **43**, and {DyO$_9$} core for complexes **41** and **42**. Computed transverse anisotropy components for **41–42** are larger than that estimated for **40** and **43** (see Tables 2 and 7). This underscores the prominent QTM operative in **41–42** compared to **40** and **43**. This led to the following trend in the computed energy barrier and magnitude of g_{zz} values: **42** < **41** < **40** < **43** (see Table 7). The principal magnetization axis is collinear with the Zn-Dy-Zn direction and remains perpendicular to the C$_2$ axis for **40** and **43**. The adjacent phenoxyl O atoms generate huge charge density distribution rendering prominent easy-axis crystal field. Contrarily, in these complexes, four methoxyl O atoms comprise hard plane. Cumulative effects from substantial negative charge distribution along easy axis in conjunction with diminished electrostatic repulsion along hard plane constitute contributing factor towards the observed magnetic anisotropy characteristics in complexes **40–43** [78].

Ab initio calculations on **44**, which is having tetrahedron geometry around Dy^{III} ion with {DyN$_4$} core, confer $|\pm\frac{13}{2} >$ nature to the first excited KD lying at 236 cm^{-1} (note: Dy^{III} ion also has weakly interacting two η_2-C=C groups, see Fig. 12h and Tables 2 and 7). This turns out to be larger than the Δ_{Orbach} energy barrier (30$\pm$2 cm^{-1}) procured from magnetic measurements. This infers the necessary consideration of other relaxation pathways within temperature range besides the operative Orbach relaxation phenomena. The KD1 and KD2 states have axial

character while KD3 lacks axiality instigating the relaxation process via this state. Therefore, the relaxation is likely to occur via combined effects of QTM and Raman pathways. Negligible matrix element ($\sim 10^{-2}$ μ_B) pertinent to TA-QTM process within ± 2 states unleashes relaxation propensity via higher excited states. Relaxation is likely to take place via KD3 as corroborated by significant matrix element corresponding to the TA-QTM (0.30 μ_B) within ± 3 states. This is supported by significant matrix element of Raman process to provide U_{cal} of 410 cm^{-1} (see Table 7) in **44** [79]. Next complex in this category is **45**, which has {DyN$_2$O$_3$} core with trigonal bipyramidal geometry (see Fig. 12i). In complex **45**, the eight KDs span within energy window of 790 cm^{-1}. Ground state is noted to be axial with $g_{zz} = 19.67$ and KD2 lying at 199 cm^{-1} (U_{cal}; see Tables 2 and 7) above the KD1 state. The presence of two THF-O donor atoms in the axial positions of **45** provides favourable crystal field to yield larger U_{cal} values [80]. Complex **46** has tricapped trigonal prismatic geometry with {DyH$_3$N$_6$} core. Three H atoms are having agostic interaction with Dy^{III} ion (see Fig. 12j). KD1 in complex **46** is computed to be Ising type ($g_{zz} = 19.91$; see Tables 2 and 7) which is well validated by large positive CFP B_2^0 as 3.28. Retention of axiality of KDs is broken at fourth excited KD (KD5) rendering $g_{xx} = 5.10$, $g_{yy} = 5.30$ and $g_{zz} = 8.00$. This in conjunction with appreciable matrix element for the TA-QTM within ± 5 (1.76 μ_B) and Orbach/Raman between $\pm 4/\pm 5$ (3.09 μ_B) instigates relaxation via this level to articulate $U_{cal} = 268.5$ cm^{-1}. Wave-function analysis iterated KD1 to be $| \pm \frac{15}{2} >$: 99% $| \pm \frac{15}{2} >$ and KD5 to be admixture of 56% $| \pm \frac{7}{2} > +18\% | \pm \frac{5}{2} >$ [81].

Complex **47** has spherical capped square antiprismatic geometry with {DyN$_6$O$_3$} core (see Fig. 12k). KD1 is determined to be pure Ising type in **47** ($g_{zz} = 19.80$) and aligned over the line which connects two carbonyl groups of the two LH$^-$ ligands. Nice agreement between experimental and calculated data lends support to the calculated properties of **47**. KD2 turns out to be: $|71\% | \pm \frac{13}{2} > +10\% | \pm \frac{11}{2} > +10\% | \pm \frac{7}{2} >$ and this is not sufficient to provoke substantial divergence from the axiality of g-tensor. Third excited KD possesses greater mixing between various $\pm M_J$ states. Non-collinearity of the easy axis of higher KDs increases with the KD energy and rhombicity increases with respect to KD1. The g_{zz} angle between KD1 and KD2 diverges by 6° and then by 60° with respect to the g_{zz} of KD3. In this context, magnetization relaxation occurs through Orbach two-phonon pathway via second excited state ($U_{cal} = 237$ cm^{-1}, see Tables 2 and 7). Significant matrix element (0.54 μ_B) pertaining to TA-QTM within ± 3 in conjunction with Orbach process between states ± 2 and ± 3 (0.98 μ_B) further corroborates the relaxation via second excited KD [83].

Complexes **48** and **49** have distorted spherical tricapped trigonal prismatic geometries and possess analogous X-ray as well as magnetic properties (see Fig. 12l). Eight KDs in **48** and **49** span within the energy span of 756 and 792 cm^{-1}, respectively, with consecutive excited states lying at ~3,100 cm^{-1} in both cases. KD1 is computed to be Ising type in both complexes (g_{zz} as 19.94 and 19.91 in **48–49**, respectively; see Tables 2 and 7). Relaxation occurs via first excited KD with U_{cal} value estimated as 218 and 238 cm^{-1} for complexes **48** and **49**, respectively, as supported by matrix

elements corresponding to TA-QTM and Orbach pathways. Axiality of the excited states gradually reduces up to sixth and seventh KD in **48–49**, respectively, with proportional enhancement in the magnetic moment along the XY-plane. Beyond these KDs, the energy levels enhance in axiality to reach nearly pure Ising type behaviour at the highest KD to reproduce KD1 observation. This sort of mirror symmetry implies the low-symmetry nature of these two compounds. To testify the accuracy of the estimated g_{zz} axis, electrostatic oblate–prolate model has been employed. Electrostatic deviation angles (angle between g_{zz} axes computed via ab initio calculations and electrostatic approach) are found to be 0.73° and 3.19° in **48–49**, respectively. This infers the propensity of principal magnetization axis to point towards the ligand donor atoms with larger electron density and shorter Dy-O bond vectors (phenoxide). This enforces Dy^{III}-4f oblate electron density to be perpendicular to the g_{zz} axis to minimize electrostatic repulsion.

Two pairs of large negatively charged phenoxide groups with shorter Dy-O bonds in conjunction with donor O atoms deliver suitable crystal field towards achievement of larger energy barrier. Experimental magnetic data is nicely reproduced harnessing ab initio computed anisotropy parameters at intermolecular interaction of -0.0025 and -0.0031 cm^{-1} for **48** and **49**, respectively. DFT calculations imply stronger negative charges on the phenoxo O atoms as induced by the strong polarization effect of Zn^{II} diamagnetic ion [76]. Like the foregoing discussion, complexes **50–52** (19.94, 19.73 and 19.71 for **50–52**, respectively; see Fig. 12m–o and Tables 2 and 7) also exhibit Ising type ground state anisotropy. Like in previous cases, larger Mulliken charges were noted on O atoms to impose larger barrier and KD1-g_{zz} axis is found to lie along the shortest Dy-O bond vectors in both complexes. Relaxations via KD2 in **50–52** were corroborated by Orbach process as revealed by the computed matrix elements (1.74, 1.80 and 1.84 μ_B for **50–52**, respectively) between ±1 and ±2 states. Though for all three complexes, KD1 is preponderantly $|\pm\frac{15}{2}>$, KD2 is preferably $|\pm\frac{13}{2}>$ with minor contributions from $|\pm\frac{9}{2}>$ energy level [84].

The conventional ways to procure improved SIM/SMM behaviour is to instil axial symmetry in complexes to minimize admixture of $|\pm M_J>$ levels. In this manner, we aim to stabilize the highest angular momentum projection, i.e. $|\pm M_J>$ as ground energy state. In compliance with group-theoretical norms, point group symmetries $C_{\infty V}$, $D_{\infty h}$, S_8, D_{4d}, D_{5h}, D_{6d} and D_{8d} exhibit disappearing off-diagonal crystal field parameters B_k^q ($q \neq 0$). This forbids admixing of $|\pm M_J>$ levels and ensures stabilization of the highest $|\pm M_J>$ level. In this way, it tends to suppress QTM and lends credence towards inducing relaxation via higher energy excited multiplets. We intend to discuss such instances where simple symmetry imposition enacted as a tool to promote energy barrier. Very recently, complex **53** was reported with unprecedented barrier (1,277 cm^{-1}, see Fig. 13 and Tables 2 and 7) and recorded the highest (to date) blocking temperature of 60 K possessing hysteresis with coercivity of 0.06 T and the sweep rate of 3.9 mTS^{-1}. Calculations inferred extraordinarily magnificent as well as first such SIM behaviour of **53** where all lower energized KDs pertain to specifically defined $|\pm M_J>$ value. Even in the higher KDs,
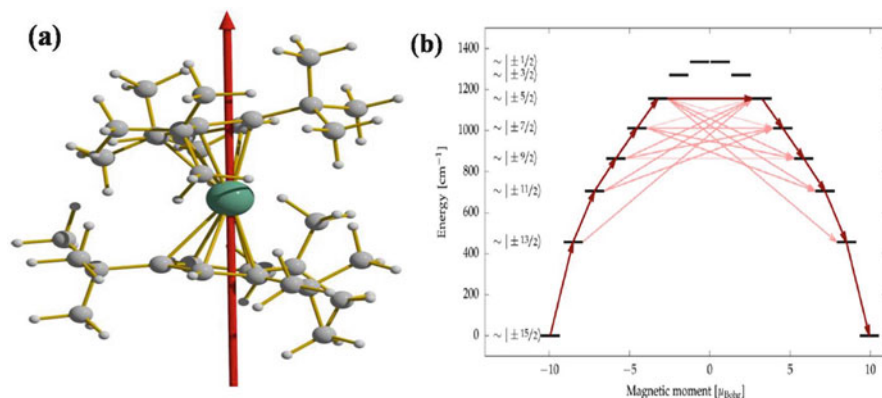
Fig. 13 (**a**) Orientation of principal magnetization axis of KD1 in complex **53**. (**b**) Ab initio spin relaxation dynamics in complex **53**. Arrow shows the orientation of the principal magnetization axis. Colour code: central atom = Dy, light-brown = C and white = H atoms. Reprinted from Guo et al. [22] with permission from John Wiley and Sons

meagre mixing of the $|\pm M_J>$ wave functions was noted. Up to fourth KD, ideal axiality exists and high axiality retains until fifth KD ($g_{xx} = 0.08$, $g_{yy} = 0.08$ and $g_{zz} = 9.12$ for fifth KD, see Table 7 for KD1). Beyond this level, transverse anisotropy components gradually become prominent and for the eighth KD, g_{xx}, g_{yy} component dominates over g_{zz} components. The g_{zz} alignments of all the excited KDs lie in parallel fashion with respect to the ground KD (see Fig. 13b for the orientation) with fifth KD forming the largest deviation of 5.6°. All the 16 lowest energy states (8 KDs) possess huge projection on specific $|M_J>$ state. Among all, the smallest projection was computed to be 0.964 within sixth KD of $|\pm M_J = \frac{5}{2} >$. This renders the allocation of all ligand field states of **53** onto one M_J state lacking mixing of energy states. In accordance with the matrix elements corresponding to the TA-QTM pathway and transverse anisotropic components, relaxation is likely to channel via sixth KD to render U_{cal} value of 1,156 cm^{-1} against U_{eff} value of 1,277 cm^{-1} (see Table 7). [22]

Complex **54** is a sandwich complex and the same as complex **53**. The most presumable relaxation for Orbach relaxation in **54** is likely: $|\pm\frac{15}{2} > \rightarrow |\pm\frac{13}{2}$ $> \rightarrow |\pm\frac{11}{2} > \rightarrow |\pm\frac{9}{2} > \rightarrow |\pm\frac{7}{2} > \rightarrow |\mp\frac{5}{2} > \rightarrow |\mp\frac{7}{2} > \rightarrow |\mp\frac{11}{2} > \rightarrow |\mp\frac{13}{2} > \rightarrow |\mp\frac{15}{2} >$ as per the calculations. Vibrational motions of the C–H groups on Cp^{ttt} ligands induce primary ($|\pm\frac{15}{2} > \rightarrow |\pm\frac{13}{2} >$) relaxation step. Pronounced axial ligand field lends well-defined delineation of the five low-lying KDs as $| \pm M_J = \frac{15}{2} >.$, $| \pm M_J = \frac{13}{2} >.$, $| \pm M_J = \frac{11}{2} >.$, $| \pm M_J = \frac{9}{2} >.$, $| \pm M_J = \frac{7}{2} >.$, $| \pm M_J = \frac{5}{2} >$ levels along the Cp-Dy-Cp axis. Model calculation with variations in the coordinated ligand type postulated that: (a) equatorial H atoms, (b) bent nature of Cp-Dy-Cp and (c) eclipsed vs. staggered nature of Cp rings hardly pose impact on anisotropy. This owes to the fact that donor contribution of Cp ring originates from delocalized π-system of ligand and not individual carbon atoms. KD1 is estimated to be Ising
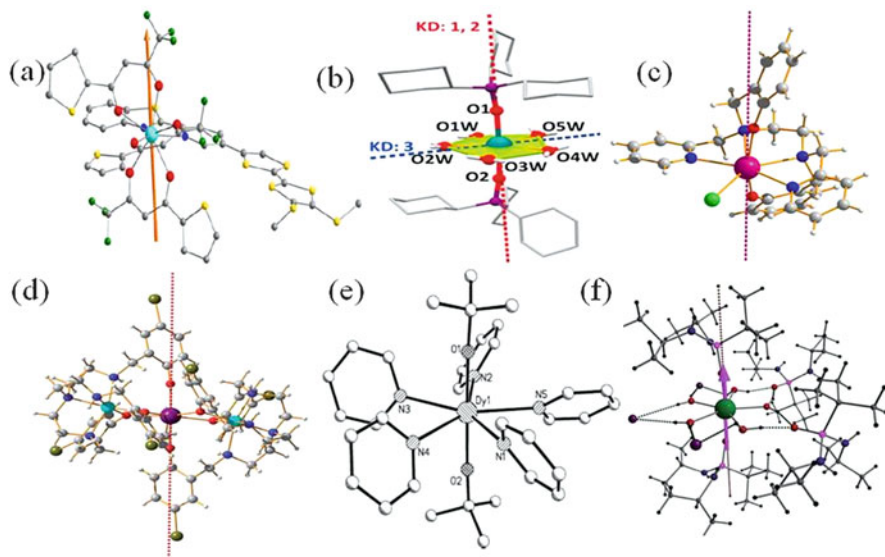
Fig. 14 (**a–f**) Molecular structures along with ground state KD orientation for complexes **55–56**, **58** and **60–62**, respectively. Arrows in complexes show the orientation of the principal magnetization axis. Colour code: central atom = Dy, red = O, dark blue/light blue = N, black/dark-brown/light-brown = C, yellow = S, green = Cl and white = H atoms. Reprinted from Gupta et al. [20], Liu et al. [82], Ding et al. [85] with permission from the Royal Society of Chemistry. Reprinted from Guo et al. [55] with permission from Nature Publishing Group. Reprinted from Ding et al. [86] with permission from John Wiley and Sons. Reprinted with permission from Liu et al. [18], Chen et al. [19] Copyright@2016 American Chemical Society

type and axiality retains until fifth KD ($g_{xy} \sim 0.01$) and g_{zz} alignment of KDs up to fifth KD remains parallel to that of KD1. Though substantial transverse anisotropy arises in sixth KD, smaller deviation between g_{zz} of sixth and ground KDs provokes relaxation via higher excited energy state. Significant transverse anisotropy ($g_{xx} = 3.36$, $g_{yy} = 4.30$ and $g_{zz} = 7.46$) in conjunction with 90° divergence of seventh KD-g_{zz} against KD1-g_{zz} unfolds relaxation via seventh KD. This outlines U_{cal} value to be 1,320.7 cm^{-1} as well validated by the huge crystal field parameter B_2^0 as 1,226.9 (see Table 7). Both complexes **53** and **54** show unprecedentedly the largest blocking temperature of 60 K (sweep rate of 22 Oe per second) and U_{eff} value of 1,223 cm^{-1} (see Table 7) [21]. Sandwich type complexes **53–54** near cylindrical symmetry and accommodation of –Cp ligand negative charges in the axial position had their privileges to instigate observation of such desired SIM characteristics.

Next complexes for this category are complexes **55** and **55′** which possess distorted square antiprismatic geometry with {DyN$_2$O$_6$} core (see Fig. 14a). KD1 of polymorphs **55** and **55′** are pure Ising type with $|\pm M_J = \frac{15}{2} >$ ground state (see Tables 2 and 7). In **55** and **55′**, relaxation is expected to occur via second and first excited KD, respectively. This can be attributed to the greater matrix elements

corresponding to TA-QTM as 0.32 (within ± 3) and 0.13(within ± 2) μ_B for **55** and **55′**, respectively. Additionally, matrix elements pertaining to Orbach process are $\pm 2 \leftrightarrow \pm 3$ (2.55 μ_B) and $\pm 1 \leftrightarrow \pm 2$ (1.88 μ_B) for **55** and **55′**, respectively. Large barriers in **55** and **55′** are ascribable to the desired pseudo-D_{4d} symmetry around the central Dy^{III} ion accentuating the crucial role of symmetry to fine-tune barrier [82]. Complexes **56** and **57** possess identical core structural motif [Dy $(Cy_3PO)_2(H_2O)_5]^{3+}$ with variation in anions. Five water molecules in the equatorial plane in conjunction with two –Cy_3PO ligands in the axial direction lend pseudo-D_{5h} symmetry to both complexes (see Fig. 14b). This provoked relaxation via second excited KD in both the complexes to render larger barrier (see values in Table 7). Matrix element pertinent to TA-QTM within ± 3 states as 3.0 and 3.2 μ_B along with significant deviations between KD1 and KD3 g_{zz} orientation provided credentials to the observed barrier. KD1-g_{zz} axis is aligned along the shortest Dy-O chemical bonds as desired. KD1 axiality as instilled by the desired ligand field symmetry was further corroborated by large negative B_2^0 CFP (-1.80 and -1.85 for **56** and **57**, respectively). [19] Complexes **58** and **59** possess local pseudo-D_{5h} symmetry, where Dy^{III} ion coordinated by 2 O in axial direction, 4 N in the equatorial plane with other equatorial site is being filled by Cl^- and Br^- for **58–59**, respectively (see Fig. 14c). KDs in complex **59** turnout to be more axial than complex **58** leading to larger barrier (see Tables 2 and 7). Additionally, larger axial (B_2^0) CFPs and smaller non-axial (B_2^2) CFPs in **59** explained the genesis of larger barrier in **59**. Shorter Dy-Cl bond compared to Dy-Br induced greater non-axial CFP in **58**. KD1-g_{zz} is oriented along the two axially located O atoms entailing its consideration vital for anisotropy. Therefore, comparatively shorter Dy-O bond and more linear O-Dy-O angle in **59** lead to larger barrier. Like in earlier cases, significant matrix element corresponding to TA-QTM (1.3 μ_B within ± 3) and Orbach processes (between ± 2 and ± 3; 2.2 μ_B) promotes relaxation via ± 3, i.e. second excited KD in **58**. However, matrix elements pertinent to TA-QTM within ± 4 (2.5 μ_B) and Orbach between ± 3 and ± 4 (2.6 μ_B) instigate magnetization blockade via third excited KD in **59** (see Tables 2 and 7 for barrier) [18]. In complex **60**, four bridging phenoxyl O atoms (also coordinated to the Zn^{II} ion), one methanol terminal O in equatorial plane along with two axial phenoxyl O atoms in axial direction constitutes the pseudo-pentagonal bipyramidal (D_{5h}) geometry around Dy^{III} ion (see Fig. 14d). This ideal symmetry corresponds to pure Ising type ground state anisotropy ($B_2^0 = -1.72$, $g_{zz} = 19.87$, see Tables 2 and 7) and leads to larger barrier by suppressing ground state QTM [85]. Large blocking temperature (14 K) in **61** can be attributed to the composite weak equatorial pyridine donor ligands combined with bis-trans-disposed tert-butoxide ligands in the axial direction. This pseudo-pentagonal bi-pyramidal (D_{5h}) geometry and near linear O-Dy-O moiety (~179°) of **61** reaffirmed the earlier statement of importance of symmetry in achieving larger barrier (see Fig. 14e and Tables 2 and 7). The lower-lying crystal field multiplets follow order $|\pm M_J = \frac{15}{2}>.$, $|\pm M_J = \frac{13}{2}>.$, $|\pm M_J = \frac{11}{2}>.$, $|\pm M_J = \frac{9}{2}>$ possessing energies 0, 564, 940, 1,141 cm^{-1}, respectively. The consecutive excited levels are mixed type and spread over 1,183–1,237 cm^{-1}. Substantial transverse g-anisotropy

components in conjunction with matrix element pertaining to ±7 states provoke relaxation via seventh KD to articulate U_{cal} as 1,220 cm^{-1} (see Table 7). Electropositive ligand donor atoms (N of pyridine) in equatorial field in conjunction with electronegative donor atoms in the axial direction constitute the desired crystal field symmetry in **61** leading to a larger barrier [86]. Five water molecules in the equatorial plane and two phosphonic diamide ligands coordinated to metal through phosphorous oxygen (P=O) in the two axial site render pseudo-D$_{5h}$ symmetry around Dy^{III} ion in complex **62** (see Fig. 14f). The axial crystal field symmetry was supported by Ising type KD1 anisotropy (g_{zz} = 19.86; see Table 6). KD1-g_{zz} axis is collinear to pseudo-C$_5$ axis and is along Dy-O-P bond vector with divergence of 4.3°. KD2 also maintained axiality (g_{zz} = 17.08, $g_{x,y}$ = 0.02) and g_{zz} is aligned almost parallel to that of KD1. Substantial transverse anisotropy (g_{zz} = 16.53, g_{xx} = 0.58 and g_{yy} = 3.13), mixed type $\pm M_J$ state ($\pm\frac{1}{2}$ and $\pm\frac{15}{2}$) and ~94° deviation between KD1 and KD3 g_{zz} orientation channels relaxation via KD3 state. This outlines U_{cal} value as 478.4 cm^{-1} which is in excellent agreement with the experimental barrier. [20] Complex **63** also possesses pseudo-D$_{5h}$ symmetry which is composed of five equatorial water molecules and two O atoms of CyPh$_2$PO ligand in the axial positions. Axial nature of KD1 (see Table 6) illustrates pronounced SIM characteristic of **63** in low temperatures. KD1-g_{zz} is oriented along principal rotational axis of pseudo-D$_{5h}$ symmetry and diverges from two axial Dy-O bond vectors by 2.9°. Accounting the ~90° difference between KD1 and KD2-g_{zz} orientations and substantial matrix element pertinent to TA-QTM within ±2 (0.76 μ$_B$) states, relaxation is likely to channel via KD2. This postulates U_{cal} value as 297 cm^{-1} and confirms pure Ising type ground state anisotropy (see Table 6) [87].

3.1.6 Ab Initio studies on Category F Complexes: Dy^{III} Single-Ion Magnets with Easy Plane/Hard Axis Anisotropy Behaviour

For the molecules which are discussed in categories A–E, the magnetization axis is easy axis with g_{zz} sufficiently greater than g_{xx}/g_{yy} (negligible or small transverse anisotropy). In these cases, molecule lies in collinear fashion with respect to the direction of applied magnetic field. If the g_{zz} axis is aligned in the perpendicular direction (against the magnetic field application) to the applied field/easy axis, the resultant anisotropy can be assumed as easy plane/hard axis anisotropy. These instances are also exemplified by large concomitant transverse anisotropy components as compared to the magnitude of g_{zz} value (XY-model). First example in this category will be complex **64** where Dy^{III} ion is found to possess seven coordination numbers with {DyN$_4$O$_3$} core (see Fig. 15a and Table 2). The geometry around Dy^{III} ion is found to have distorted pentagonal bipyramidal geometry. The χ$_M$T vs. T data in complex **64** can be ascribed to the depopulation of the excited sublevels. In order to assess their compatibility with the earlier reported crystal field parameters of **64**, EVALUCF software was employed to estimate the CFPs. The impact of ligand field over various energy multiplets (generated by SOC coupling) was derived through
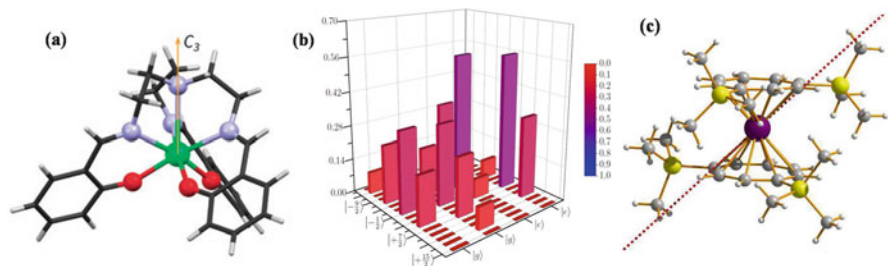
Fig. 15 (**a**, **c**) Molecular structures of complexes **64–65**, respectively. (**b**) Pictorial representation of wave-function composition in complex **64**. Arrow in complexes shows the orientation of the principal magnetization axis. Colour code: central atom = Dy, red = O, light blue = N, black/light-brown = C, yellow = Si and white = H atoms. Reprinted from Lucaccini et al. [88] with permission from the Royal Society of Chemistry. Reprinted with permission from Le Roy et al. [89] Copyright@2013 American Chemical Society

Table 8 List of complexes {from category F} with pertinent experimental energy barrier (U_{eff}, in cm^{-1}), ab initio computed energy barrier (U_{cal}, in cm^{-1}), main magnetic g factors and crystallographic structural information

	U_{eff}	U_{cal}	g_{xx}–g_{yy}	g_{zz}	Type of coordinated atoms	Structure	Ref.
64	7 ±1	50^a	9.4±0.5	1.8± 0.1	4 N, 3 O	–	[88]
65	17.4	15.6	10.7	1.35	Sandwich complexation (two COT^{2-} in η^8-fashion)	–	[89]

^{a}Computed harnessing the procured crystal field parameters

crystal field parameterization within Wybourne's formalism (Dy^{III} ion is on C$_3$ axis in **64**). This methodology does not utilize any free parameters and nicely replicate the experimental magnetic data as well as earlier reported crystal field parameters. This approach permitted direct comparison with luminescence data and allows easy inclusion of excited energy multiplets for further reference. Subsequent diagonalization rendered eigenvalues and eigenvectors of $| J, M_J>$ components by defining ground–first excited gap as 50 cm^{-1} (see Table 8). The same approach lends estimation of effective g parameters, i.e. $g^{eff}_{\perp} = 9.6$ and $g^{eff}_{\parallel} = 2.2$ (see Table 8) evoking easy plane type anisotropy for complex **64**. Smaller energy difference and easy plane anisotropy nature were supported by the mixed ground multiplet wave-function type as: 8.7% $|\pm\frac{13}{2}> + 24.3\%|\pm\frac{7}{2}> + 33.1\% |\pm\frac{1}{2}> + 20.2\% |\pm\frac{5}{2}> + 5.3\% |\pm\frac{11}{2}>$. Contrary to necessary requirement of larger $|\pm M_J>$ stabilization towards achieving higher barrier, ground multiplet is dominated by the stabilization of smaller $|\pm M_J>$ components in **64**. However, first excited state wave-function composition was subjugated by larger $|\pm\frac{3}{2}>$ and $|\pm\frac{9}{2}>$ components of the energy level (see Fig. 15b) [88]. Complex **65** is a sandwich complex of Dy^{III} ion (see Fig. 15c and Table 2). Stabilization of $|\pm M_J = \frac{1}{2}>$ energy multiplet in complex **65** was exemplified by estimated g factors: $g_{xx} = 10.67$, $g_{yy} = 10.63$ and $g_{zz} = 1.35$ (see Table 8). The KD1-g_{zz} axis point is amidst the two COT"$^{2-}$ ligands and goes through

the Dy^{III} ion. This testifies prominent impact of the distant silyl groups over the alignment of KD1-g_{zz} axis. Eighth KD in complex **65** is found to be highly axial ($g_{zz} = 19.99$, $g_{xx} = g_{yy} = 0$). This unfolds the fact that replacement of Dy^{III} by Er^{III} ion might lead to improved SIM behaviour of the same complex [89].

3.2 Model Complexes Predicted Using Ab Initio Calculations

To put an end to the ongoing argument of suitable geometry, symmetry, coordination number and type of metal ions towards achieving the best SIMs characteristics, calculations were carried out on several models to gain intuitive understanding and to make viable predictions. While ab initio calculations have proven track record to yield magnetic properties of lanthanide compounds with great accuracy, employing this methodology for predictions is at its infant stage. Here, we intend to cover such predictions and related experimental verification of the same/similar ideas, if available, already in the literature.

First of this kind here is complex **66** where originally X-ray structure is reported for the Sm^{III} analogue and ab initio calculations are performed by replacing the Sm^{III} by Dy^{III} ion (see Fig. 16a). Calculations reveal the six lowest KDs as $| \pm M_J > = | \pm \frac{15}{2} >, | \pm \frac{13}{2} >, | \pm \frac{11}{2} >, | \pm \frac{9}{2} >, | \pm \frac{7}{2} >$ where all have identical quantization axis. Accounting negligible matrix elements pertinent to QTM and TA-QTM pathways, U_{cal} can be outlined as ~1,800 cm^{-1}. The barrier is one of the largest known and owes to the near linear N-Dy-N (~176°) structural moiety unleashing targeted synthesis towards this direction [90]. Besides this prediction, magneto-structural correlation was performed. This discarded the need for ∠ligand-Dy-ligand to approach towards 180°. Instead, the essential need for two-coordinate Dy^{III} complexes was established towards achievement of larger energy barrier. To testify this, calculations were carried out on model **67** where ∠C-Dy-C = 137° and 143°. For these geometries, the U_{cal} values were turned out to be ~1,247 and 1,484 cm^{-1}, respectively, against the predicted of 1,800 cm^{-1} for **66** (see Fig. 16b). From both the model calculations, two-coordinate Dy^{III} systems seem to be extremely desirable. Besides, other model calculations evoked mitigation of barrier upon coordination of solvent molecule [91]. Apart from these two coordinate models, there are also other models predicted from the existing structures. For example, **62′** modelled by the removal of five water molecules coordinated in the equatorial plane of the Dy^{III} ion in complex **62** found to yield substantially higher barrier height (more than 2,085 cm^{-1}). The Dy-O interactions present in **62′** are stronger than Dy-C interaction in **66** and the presence of higher symmetry quenches the tunnelling leading to very large barrier height (see Fig. 16c, d). The computed U_{cal} value for this model is one of the largest reported to date; however, these predictions are yet to be tested.

Another area where prediction seems to taken a lead in the SIMs synthesis is lanthanide encapsulated fullerene molecules that are predicted to possess interesting magnetic properties. For example, model complex **68** is an example of endohedral
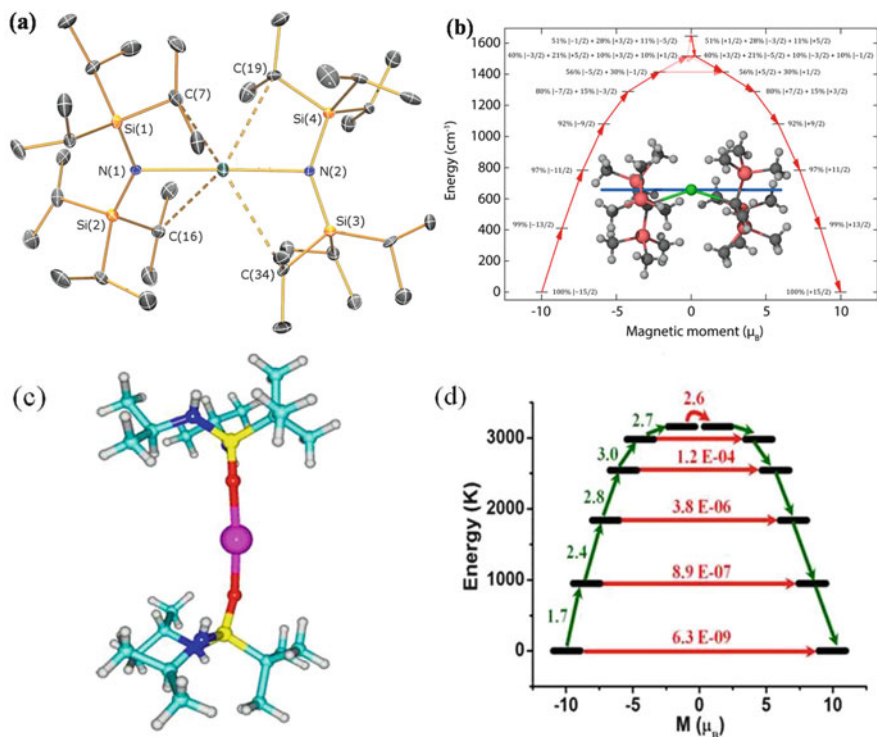
Fig. 16 (**a**, **c**) Molecular structures for complexes **66** and model **62′**, respectively. (**b**) Ab initio calculated relaxation dynamics for complex **67**. (**d**) Relaxation dynamics for model **62′**. Arrows in complexes show the orientation of the principal magnetization axis. Colour code: central atom = Dy, red = O, dark blue = N, black/dark-brown/cyan = C and white = H atoms. Reprinted from Gupta et al. [20], Chilton et al. [90] with permission from the Royal Society of Chemistry. Reprinted with permission from Chilton [91] Copyright@2015 American Chemical Society

radical hetero-metallo-fullerene molecule. Originally, $Gd_2@C_{79}N$ has been originally reported to possess $S = \frac{15}{2}$ ground state. Calculations that were initially performed by DFT methods reveal unusually large exchange interaction between radical and Gd^{III} ion [92]. The values are nearly by an order magnitude larger (400 cm^{-1}) than the radical–Gd^{III} coupling known in the literature (27 cm^{-1} reported for the recorded high exchange reported experimentally for $\{Gd_2N_2^{3-}\}$ complex) [93, 94]. Very recently, magnetic susceptibility measurement coupled with EPR techniques verifies this prediction, where experimental J values are reported to be $350 \pm 20 \text{ cm}^{-1}$ [95]. Additionally, calculations were performed by replacing the Gd^{III} ions by Dy^{III} ions. The Dy sites in model **68** bind in η^7/η^6 fashion with the hexagonal ring to deliver the strongest predicted exchange coupling along one of the axial directions (see Fig. 17a). Additionally, another weaker coupling was noted for **68** due to the presence of second Dy^{III} centre. The eight KDs span over a window of 837 and 786 cm^{-1} for Dy1 and Dy2 centres, respectively. KD1 for both the sites
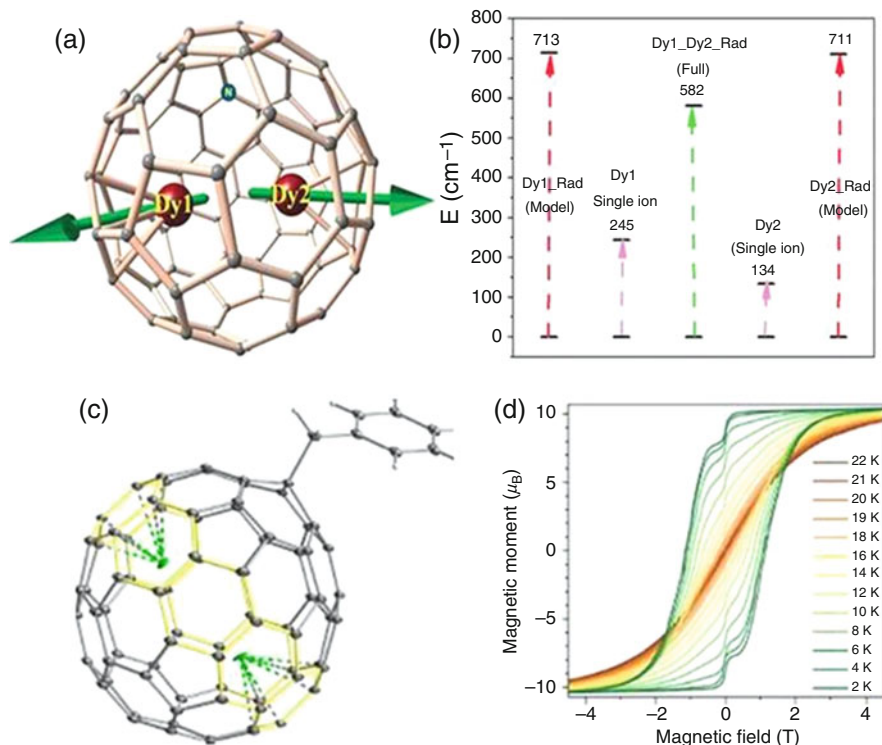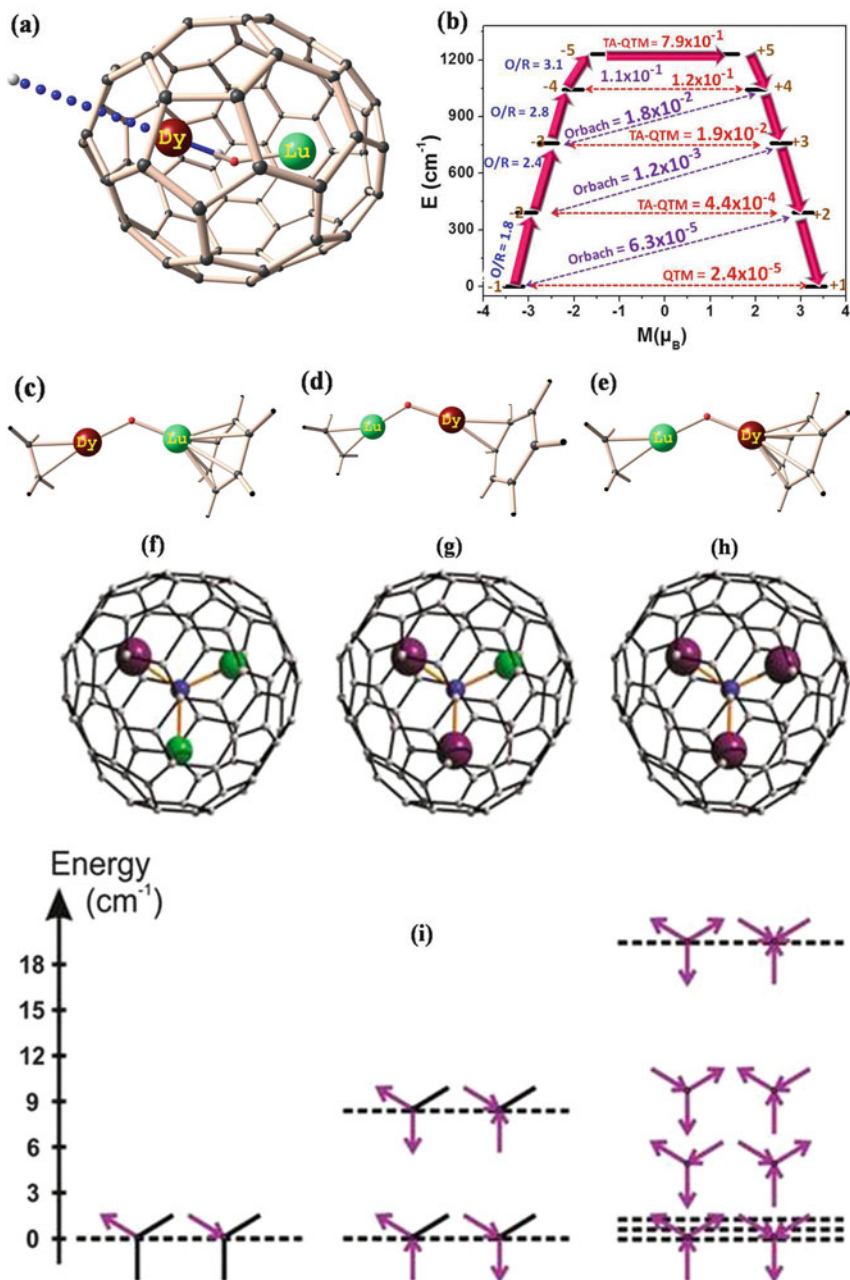
Fig. 17 (**a**, **c**) Representative molecular structures for complexes **68** and **68′**. (**b**) Ab initio calculated U_{cal} for complex **68** and (**d**) magnetization curves measured at various temperatures with the field sweep rate of 2.9 mTs^{-1} for complex **68′**. Arrows in complex **68** show the orientation of the principal magnetization axis. Colour code: central chocolate/green atoms = Dy, blue = N, dark-brown = C and white = H atoms. Reprinted from Singh et al. [92] with permission from the Royal Society of Chemistry. Reprinted from Liu et al. [96] with permission from Nature Publishing Group

are estimated to be pure Ising type ($g_{xx} = g_{yy} = 0$, $g_{zz} = 19.98$ and 19.88 for Dy1 and Dy2 centres, respectively) indicating negligible QTM ($0.0006~\mu_B$) contribution within ground multiplet. KD1-g_{zz} lies along pseudo-C$_6$ axis of the hexagonal ring. Accounting for substantial matrix element and deviation between g_{zz} axes, relaxation for both Dy sites is likely to channel via KD2. This postulates the U_{cal} value as $244.5~\text{cm}^{-1}$ and $134.3~\text{cm}^{-1}$ for Dy1 and Dy2 centres, respectively. The discrepancy between the barrier values of two Dy centres can be ascribed to the varying coordination mode with Dy1 centre interacting strongly with C$_{79}$N compared to the Dy2 site. Large ground–first excited level gap for the centres can be attributed to the large value of CFP B_2^0 as -4.54 for both centres. To have intuitive understanding of the exchange spectrum, two types of models were employed, where each of them contained one paramagnetic Dy^{III} ion along with radical hetero-fullerene, while other Dy^{III} ion is being substituted by a diamagnetic Lu^{III} ion. Ground state exchange doublets for both the models are pure Ising type with $g_{xx} = g_{yy} \sim 10^{-8/-9}$ and

$g_{zz} = 21.9$. In both the centres, sufficient tunnel splitting within first excited exchange doublets spurs relaxation via that level and this outlines $U_{cal} \sim 710$ cm^{-1} for both centres. This increase in the energy separation between the ground to the first excited state is attributed to the very large magnetic exchange between Dy-radical centres. For more accurate model consideration, exchange spectrum containing both Dy centres and radical was constructed harnessing $J_{Dy-rad} = +285.7$ cm^{-1} and $J_{DyDy} = -0.3$ cm^{-1}. Considering substantial tunnel splitting, U_{cal} value from this model can be estimated as 582 cm^{-1} (see Fig. 17b). This decrease in the energy separation between the ground to the first excited state with respect to Dy-radical model is attributed to the weak magnetic exchange between both Dy-Dy centres. Hence, in all the employed exchange-coupled models, U_{cal} value is found to be larger than that for single-ion Dy^{III} ion. So, like earlier discussion, exchange is likely to play proactive role in increasing the barrier by suppressing the QTM propensity [92]. Popov and co-workers have synthesized analogous $Dy_2@C_{80}(CH_2Ph)$ EMF (**68′**) possessing very strong exchange coupling between Dy^{III} and radical fullerene cage leading to a U_{eff} value as high as 426 cm^{-1} and a reported blocking temperature of 18 K. Hetero-fullerenes are expected to have larger magnetic exchange constant value because the unpaired electrons are found to be localized between two Dy^{III} ions enhancing the charge-transfer contribution and hence the exchange coupling constants are expected to show even higher U_{eff} values (see Fig. 17c, d) [96].

Like previous one, models **69–71** exemplify three different endohedral metallofullerenes (EMF) that encapsulate ${DyO-Lu/Sc}^{4+}$ unit inside C_{72}, C_{76} and C_{82} fullerene cages, respectively (see Fig. 18a). In these studied EMFs for DyO-Lu/Sc@C_{76} (**70**) model, four different isomers were also studied to ensure the effect of different isomers of a given fullerene on anisotropic properties. In all these models, Dy^{III} ion is ligated to hexagonal/pentagonal aromatic ring inside the fullerene ring where Dy-C distances are evaluated in the range of 2.4–2.6 Å. The Dy-O distances are found to be in the range of 2.0–2.1 Å and this articulates stronger axial interaction with the O atoms. For DyOLu@C_{76}, isomer DyOLu@C_{76}–1 (**70a**) is computed to possess the lowest energy (ground state, C_s symmetry). The other isomers DyOLu@C_{76}–2 (**70b**), DyOLu@C_{76}–3 (**70c**) and DyOLu@C_{76}–4 (**70d**) are located at 6.2, 41.1 and 55.2 kJ/mol energy higher than corresponding **70a**. For complex **69**, the Dy^{III} ion and C_{72} cage exhibit η^6 interaction with six-membered ring. However, for **70a** and **71**, C_{76} and C_{82} cages render η^2 interaction with six-membered ring. Eight KDs in **69–71** spread within an energy window of 1,475–1,625 cm^{-1} (see Fig. 18b). KD1 of Dy^{III} sites in all cases are pure Ising type ($g_{zz} = 19.98$, $g_{xx} = g_{yy} = 0$) with stabilization of $|M_J = \pm\frac{15}{2}>$ ground state. Mechanism developed suggests that the relaxation is likely to occur via KD2 in **69–70** and third excited state (KD4) in complex **71**. This renders U_{cal} value of 451.6, 396.7, 425.7, 487.0, 476.6 and 1,220.3 cm^{-1} for **69**, **70a**, **70b**, **70c**, **70d** and **71**, respectively. With the increase in fullerene cage size, the equatorial interaction of aromatic ring with Dy^{III} ion is progressively minimized. This instigates mitigation of transverse anisotropic properties in conjunction with proportional enhancement in the magnitude of the barrier

Fig. 18 (**a, f–h**) Representative molecular structures for complexes **69–77**. (**b**) Spin relaxation dynamics for complex **74** (**c–e**) models **a–c**, respectively. (**i**) The magnetic structure of the pertinent Ising like states is reflected above with schematic local magnetic moments locating along Dy-N bonds for complexes **75–77**. Arrows in complexes show the orientation of the principal magnetization axis. Colour code: central chocolate/violate atom(s) = Dy, red = O, blue = N, dark-

height. To facilitate procurement of extensive testament, three models have been developed with ethylene, η^2-benzene and benzene interacting with Dy^{III} ion (models **a–c**, see Fig. 18c–e) offering different Dy-π interactions. The models were constructed in resemblance to the lanthanide–fullerene interactions with C_{82}, C_{76} and C_{72} species, respectively. For models **a–c**, as we move towards right, progressive reduction in the barrier values were detected (U_{cal} of 2,059, 1,603 and 1,424 cm^{-1} for **a–c**, respectively). All the aforementioned **69–71** studied structures were modified by substituting Lu^{III} with Sc^{III} (corresponding **72–74**) to undertake detailed analysis. In the resultant modified structures, Ln-O-Sc possesses larger angles compared to Ln-O-Lu analogue owing to stronger Sc-O interaction and smaller Sc ionic radius. Like Lu^{III} ion analogues, their corresponding Sc analogues also render pure Ising type KD1 anisotropy. Considering the foregoing contributing factors towards determining relaxation phenomena, magnetization blockade is likely to be observed via fourth excited KD in all Sc^{III} analogues. This articulated U_{cal} value of 1,191, 1,189, 1,231, 1,341, 1,346 and 1,406 cm^{-1} for DyOSc@C_{72} (**72**), DyOSc@C_{76}(a–d) (**73**) and DyOSc@C_{82} (**74**) EMFs, respectively. To understand these observations, magneto-structural correlation was carried out on some models (model **a**, see Fig. 18c). With proportional increase of Dy-O-Lu angle, increment in U_{cal} value was noted essentially due to achievement of higher symmetry. The DyOSc@C_{82} (**74**) EMF turns out to possess one of the highest U_{cal} values for EMF based SIMs (1,406 cm^{-1}, see Fig. 18b) [97]. Recently, Popov and co-workers have synthesized two isomers of Dy$_2$S@C_{82} EMF {$C_{3v}(8)$ and $C_s(6)$} with three ensuing Orbach processes having energy barriers of 7, 33 and 856 cm^{-1} for the former isomer and with two energy barriers of 11 and 364 cm^{-1} for the latter isomer. Oxygen is known to be a stronger ligand compared to sulphur and the axial ligand field for the former is expected to be stronger and therefore Dy$_2$O@fullerenes are expected to be superior compared to the corresponding sulphur analogues [99].

Complexes **75–77** are series of Dy-Sc-EMFs with Dy$_n$Sc$_{3-n}$N@C_{80} structural motif and n varies from 1 to 3 for **75–77**, respectively (see Fig. 18f–i). In all three structures studied, the Dy$_n$Sc$_{3-n}$N unit presents with the N atom at the centre of the triangle. KD1 of Dy^{III} centre in **75** and two Dy^{III} centres of **76–77** exhibit pure Ising type anisotropy. The corresponding g_{zz} values vary in the range of 19.84–19.88 with g_{xy} lying in the range of $\sim10^{-4/-5}$. Even the KD2 for all Dy sites are found to be axial with the $g_{zz} = 16.96$–17.10 and $g_{xx} = g_{yy} = 10^{-4/-5}$. Such strong axiality implied pure $|\pm M_J = \frac{15}{2}>$ and $|\pm M_J = \frac{13}{2}>$ characters of the KD1 and KD2 level, respectively. The eight KDs span over an energy window of $\sim$1,500 cm^{-1} in **75–77** and this split for atomic $^6H_{15/2}$ multiplet is very unusual and larger compared to other Dy systems. This can be rationalized by the efficient contribution from N to the ligand field splitting of $^6H_{15/2}$ multiplets. KD2 lies at 415, 507/393 and 555/569/

610 cm^{-1} higher than the ground doublet for **75**, two Dy centres of **76** and three Dy centres of **77**, respectively. In order to assess the role of fullerene cage, calculations were undertaken on isolated [DySc$_2$N]$^{6+}$ unit. Alleviation of Dy ligand field splitting (~30%) was observed upon removal of the fullerene cage (U_{cal} = 327 cm^{-1}). The Dy-N bonds strongly interact with the fullerene cage. This has reduced the axiality of the lowest KDs and directs g_{zz} axis far from this bond vector. Strong local axiality of Dy sites, larger energy separation among ground and excited energy doublets, diminishes the coupling between the lowest KDs on Dy sites to the identical non-collinear Ising form. The Dy-Dy coupling in complexes **76** and **77** is quite significant contrasting the general notion of weaker 4f-4f interaction. The stronger exchange owes to stronger Dy-N bond, which also impinged on the larger ligand field splitting of the single-ion Dy centres. Non-Kramers exchange-coupled complex **76** shows degenerate ground exchange doublets (Δ_{tun} = 10^{-10} cm^{-1}) possessing g_{zz} = 34.13. First excited exchange doublet lying at ~8 cm^{-1} above also is strongly axial and degenerate (Δ_{tun} = 10^{-9} cm^{-1}). Quenched QTM within ground exchange doublet invokes the occurrence of two relaxation processes in **76**. The higher temperature relaxation corresponds to relaxation via local excited levels of individual Dy centres (393/507 cm^{-1}) and low-temperature relaxation pertains to overcoming the exchange energy barrier (~8 cm^{-1}). Exchange splitting in **77** (~19 cm^{-1}) is stronger than **76** due to four additional Dy-Dy interactions in the former. All the four lowest-lying exchange doublets in **77** are strongly Ising type (Δ_{tun} = 10$^{-7/8}$ cm^{-1}). First three lowest-lying exchange doublets possess $g_{zz} \approx 40$ while the most highly energetic fourth exchange doublet shows $g_{zz} \approx 3$. The three low-lying exchange doublets are quasi-degenerate with energy split over ~1 cm^{-1}. This outcome is ascribable to the underlying net Ising type interaction and different magnitude of interactions between Dy2 and Dy3 centre. Such unique quasi-degeneracy of the low-lying ground exchange doublets of **77** induces magnetic frustration. This subsequently promotes QTM within the ground exchange doublet and undermines the SMM behaviour and renders the weakest SMM behaviour (than **75** and **76**) [98].

Intrusion of small magnetic units {[LnX]$^{-/0/+}$} into cages turns out to be a potential strategy towards ameliorated SMM behaviour. The distance between cage and Dy was systemically changed in a hypothetical [DyO@C$_{60}$]$^+$ complex (**78**). Computational studies performed on complex **78** revealed that the *Ising* doublet eigenstates are energetically arranged chronologically in terms of both the M_J value and the energy spacing, with $|M_J = \frac{15}{2} >$ as the ground state doublet. The magnitudes of U_{cal}, which are subject to the Dy-O bond length, can attain a value as high as 2,100 cm^{-1} [60].

3.3 Review on Er^{III} Containing Single-Ion Magnets

Literature perusal indicates study on Dy^{III}-based SMMs is prevalent due to very strong magnetic moment and $|\pm M_J = \frac{15}{2} >$ value of corresponding Dy^{III} ion. In recent years, the study of another lanthanide ion (Er^{III}; $^4I_{15/2}$) containing identical M_J

value has gradually transpired. Er^{III} is a prolate type ion with axially located 4f electron density and entails strong equatorial crystal field to stabilize the highest angular momentum projection. Notably, we abstain ourselves from discussing the di-, or polynuclear Er^{III} based SMMs and are confined within SIMs with zf-SIM behaviour or likely to show zf-SIM behaviour. Series of Er^{III} complexes, **79–82** (see Table 2 for molecular formula), were theoretically investigated using ab initio calculations to check the influence of symmetry and structural distortions on the magnetic anisotropy. Complex **79** has a distorted square antiprism geometry with $\{ErN_2O_6\}$ core. Complexes **80–82** are sandwich type structures. With single-ion anisotropic properties, nice agreement between experimental and theoretical magnetic data has been demonstrated in all the four complexes. Except for complex **79**, all three complexes possess pure Ising type ground state anisotropy. On the other hand, KD1 in **79** is axial with significant transverse anisotropic contribution. KD1-g_{zz} is aligned towards one of the –N donors of –bath ligand and deviates from Er-N bond by 25.8°. Two different U_{eff} values observed experimentally can be attributed to the presence of two conformations of the –Me groups present in the – thd ligands (where thd = (2,2,6,6-tetramethyl-3,5-heptanedionate); bath = bathophenanthroline). Concomitant transverse KD1 anisotropy promotes ground state QTM propensity as corroborated by corresponding matrix element of 0.35 μ_B. This pathway complies nicely with the observed fast relaxation of magnetization. However, matrix elements corresponding TA-QTM/Orbach involving ±2 evoked relaxation via KD2 and this corresponds to the observed slow magnetization relaxation outlining U_{cal} value as 37 cm^{-1} (see Table 9). Calculations on model complex reflect no impinge of methyl group rotation on the magnitude of the barrier. In complex **80**, KD1-g_{zz} axis is directed along the main C_8 axis which passes through the centre of COT ligand. The Ising type KD1 with no transverse g anisotropic components rationalized the large difference in the magnitudes of barrier height computed between **79** and **80–82**. High symmetry in **80** and **81** led to collinearity among the g_{zz} orientations up to sixth KD. However, stabilization of $|M_J = \pm\frac{1}{2}>$ state in the second excited KD of **80–81** provokes relaxation via this level. However, the absence of exact symmetry in complex **82** (**79** as well) causes prominent non-collinearity between KD1 and KD2 g_{zz} axes instigating relaxation via KD2 itself (see Table 9 for estimated barrier values). The computed barrier height reflects a trend of **80 > 81 > 82 > 79** and this is in accordance with the attenuation of computed axial crystal field parameters. In order to put an end to ongoing contention of appropriate coordination number around metal ion, calculations were carried out on various $[Dy/Er(OH)_n]^{m+}$ models. Among all the appraised models, three-coordinated D_{3h} and four-coordinated D_{4h} models are computed to possess the largest barrier heights. This owes to the extensive stabilization of the equatorial crystal field for the prolate type Er^{III} ion by the favourable negatively charged –OH groups (see Fig. 19a). In similar context, calculations on $[Dy(OH)_n]^{m+}$ models indicated two-coordinated model to be most appropriate. Contrarily, two-coordinated model for Er^{III} ion does not exhibit any SMM behaviour due to lack of equatorial ligation. Model calculations affirmed crucial importance of high symmetry towards achievement of ameliorated anisotropy behaviour [118]. In

Table 9 Complexes (**79–119**) with pertinent experimental energy barrier (U_{eff}, in cm^{-1}), ab initio computed energy barrier (U_{cal}, in cm^{-1}), main magnetic g factors and crystallographic structural information

	U_{eff}	U_{cal}	g_{xx}	g_{yy}	g_{zz}	Type of coordinated atoms	Structure of complex	Ref.
79	10.83, 15.55	37.0	0.67	1.41	14.88	2 N, 6 O	Distorted square antiprismatic	[100]
80	150.1	280.4	0.00	0.00	17.94	π-coordination (η^8-fashion)-All C	Sandwich type	[100]
81	130.0	247.1	0.00	0.00	17.94	π-coordination (η^8-fashion)-All C	Sandwich type	[100]
82	136.9	164.5	0.00	0.00	17.92	π-coordination (η^8-fashion)-All C	Sandwich type	[100]
82′a	137	84.8	0.00	0.00	17.94	π-coordination (η^8-fashion)-All C	Sandwich type	[100]
82′b	224	115.9	0.00	0.00	17.94	π-coordination (η^8-fashion)-All C	Sandwich type	[100]
83	85	331	0.00	0.00	17.88	3 N	Distorted trigonal planar	[80]
84	–	76	0.03	0.64	16.20	3 N, 2O	Distorted trigonal bipyramidal	[80]
85	44	118	0.02	0.02	17.81	3 N,1 Cl	Distorted tetrahedral	[101, 102]
85a	44	118	0.02	0.02	17.80	3 N,1 Cl	Distorted tetrahedral	[101, 102]
86	3.6, 35.7	48.9, 104.9	1.03, 0.04	2.77, 0.07	13.99, 15.79	10 O	Distorted bicapped square antiprismatic	[103]
87	74	58.7	10.77	8.33	1.20	8 N	–	[54]
88	199	194.0	3.5 × 10^{-6}	3.5 × 10^{-6}	17.96	π-coordination (η^8-fashion)-All C	Sandwich type	[13]
89	22±1	54^a	1.2		13	4 N, 3 O	Distorted monocapped octahedron	[104]
89 (122 K)	20,54	67, 58	1.85,^{b} 2.18	1.85, 2.18	14.23, 13.81	4 N, 3 O	Distorted monocapped octahedron 1	[104]
89 (293 K)	20,54	64, 52	1.83,^{b} 2.28	1.83, 2.28	14.26, 13.68	4 N, 3 O	Distorted monocapped octahedron	[104]

|								
90	No mention	13.2, 13.5	4.96,b 5.27	4.97, 5.28	8.66, 7.79	4 N, 3 O	Distorted monocapped octahedron	[104]
91	No mention	21.3, 15.8	0.87, 0.53	1.30, 1.62	14.10, 13.07	4 N, 3 O	Distorted monocapped octahedron	[104]
92	27.1, 34.1	19.8	1.8	2.8	10.9	4 O, 4 N	Square antiprismatic	[105]
93	4.9	187.9	3.21	2.69	1.76	6 O	Trigonally distorted octahedron with fac-term	[106]
94	20.2, 24.3	197.2	0.1	1.0	6.8	4 O, 4 N	Square antiprismatic	[105]
95	Not SIM	1.6	0.5	2.1	12.7	4 O, 4 N	Square antiprismatic	[105]
96	Not SIM	4.8	1.3	3.3	6.2	4 O, 4 N	Square antiprismatic	[105]
97	Sot SIM	4.6	0.95	1.02	12.02	4 O, 4 N	Square antiprismatic	[105]
98	Not performed	160	0.03	0.61	7.39	5 O, 4 N	Capped square antiprismatic	[107]
99	Not performed	–	4.47	4.40	0.92	4 O, 4 N, 1 F	Capped square antiprismatic	[107]
100	Not performed	–	3.02	3.24	1.72	4 O, 4 N, 1 F	Capped square antiprismatic	[107]
101	14.7	180	0.33	0.48	4.06	9 O	-; $\angle ZnCezn = 174°$	[108]
102	20.9	503	2.43	2.43	1.03	π-coordination (η^{8}-fashion)-All C	Sandwich type	[108]
103	18.8	–	0.02	0.10	2.48	8 O	Distorted hexagonal bipyramidal	[109]
104	15.3	–	0.07	0.21	4.18	8 O	Distorted hexagonal bipyramidal	[109]
105	11.2/17.2 (zf-27.3) (field = 2000 Oe	209.9	0.02	0.02	6.29	7 O	Distorted pentagonal bipyramidal	[110]
106	15/19	12.9	0	0	19.16	8 N	–	[54]
107	Not SIM		0	0	17.10	6 N incorporation of agostic interactions with three Hs	Trigonal prismatic; incorporation of agnostic interactions with H: Tricapped trigonal prismatic	[81]
108	Not SIM		0	0	16.92	6 N incorporation of agostic interactions with three Hs	Trigonal prismatic; incorporation of agnostic interactions with H: Tricapped trigonal prismatic	[81]

(continued)

T. Gupta et al.

Table 9 (continued)

	U_{eff}	U_{cal}	g_{xx}	g_{yy}	g_{zz}	Type of coordinated atoms	Structure of complex	Ref.
109	237, 245	227	0	0	19.86	7 O	Distorted pentagonal bipyramidal	[111]
110	77.1	404.4	0	0	13.96	Three N atoms from an η^3-coordinated tridentate pyrazolylborate anion and an η^8-coordinated COT dianion		[112]
111	32.0	408.0	0	0	13.96	Three N atoms from an η^3-coordinated tridentate pyrazolylborate anion and an η^8-coordinated COT dianion		[112]
112	216					8 N, Double Double-decker square antiprismatic		[113]
113	44.8, 45.2	256.36	0	0	17.93	6 N Incorporation of agostic interactions with three Hs	Trigonal prismatic; incorporation of agostic interactions with H: Tricapped trigonal prismatic	[79]
114	21	229.39	0	0	17.92	6 N Incorporation of agostic interactions with three Hs	Trigonal prismatic; incorporation of agostic interactions with H: Tricapped trigonal prismatic	[79]
115	12.2±0.5	228	0	0	17.88	4 N	Tetrahedron	[79]
116	652	–	–	–	–	8 N	Double-decker square antiprismatic	[114]
117	564	–	–	–	–	8 N	Double-decker square antiprismatic	[115]
118	523	–	–	–	–	8 N	Double-decker square antiprismatic	[116]
119	653	–	–	–	–	8 N	Double-decker square antiprismatic	[117]

[a]Computed harnessing the procured crystal field parameters
[b]First one belongs to one molecule CASSCF approach while second corresponds to one molecule embedded in five layers of point charges CASSCF approach
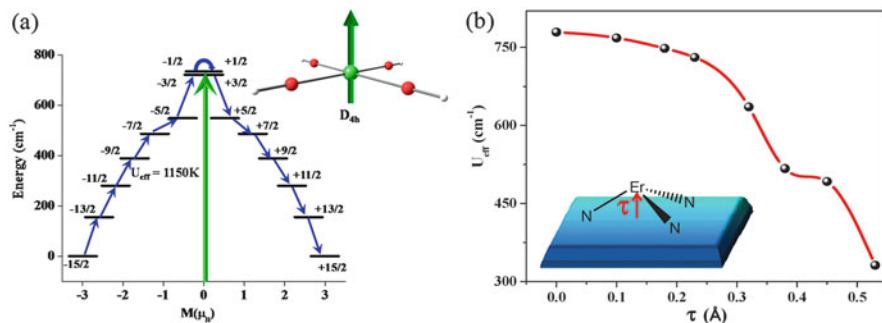
Fig. 19 (**a**) Magnetization blockade mechanism for model $[Er(OH)_4]^-$. Reprinted with permission from Baldoví et al. [45], Oyarzabal et al. [46], Aravena and Ruiz [47], Baldovi et al. [48–50], Pointillart et al. [51] Copyright@2014 American Chemical Society. (**b**) Magento-structural correlation developed by varying τ parameter. Reproduced from Rajaraman et al. [80] with permission from the Royal Society of Chemistry

another report, another sets of calculations were carried out on two rotational conformers of complex **82** which we designate as **82′a** and **82′b** (see Table 9). Calculations on the conformers evaluated at 120 K indicate strong axiality in KD1 with $g_{xx} = g_{yy} \sim 10^{-4}$ and $g_{zz} = 17.94$ (see Table 9). This denotes stabilization of $|M_J = \pm\frac{15}{2}>$ ground state with KD1-g_{zz} lying perpendicular to the average of the planes of the two rings of COT and Cp* ligands. Computed ground–first excited energy level separations of the two conformers, 84.8 and 115.9 cm^{-1}, are lower than the U_{eff} value of 137 and 224 cm^{-1} for **82′a** and **82′b**, respectively (see Table 9) [100].

In complex **83**, Er^{III} ion is positioned above the trigonal plane of the ligand donor atoms (τ, shift by 0.53 Å) while in **84**, in addition to the equatorial plane, two O atoms (THF) occupy the axial positions (see Table 2). In compliance with our foregoing model prejudice, zero-field SMM behaviour and lack of zero-field SMM behaviour were noted for **83** and **84**, respectively. The favourable equatorial ligand field is reflected in the Ising type KD1 state ($\pm\frac{15}{2}$) of **83** while intrusion by two axial ligands in **84** deteriorated the axiality with significant g_{xy} components (see Table 9). Accounting for the negligible matrix element pertinent to TA-QTM pathway, relaxation for **83** is channelled via unprecedented fourth excited KD postulating U_{cal} value as 331 cm^{-1} (see Table 9). The large discrepancy between U_{cal} and U_{eff} values can be rationalized to the unavailability of dilution experiments on this complex. However, for **84**, like conventional routes, relaxation is supposedly to take place via KD2 in accordance with substantial matrix elements (see Table 9 for barrier). Out-of-plane shift parameter (τ) was gradually varied by moving Er^{III} ion towards the plane of ligands. This correlation shows the largest barrier for planar structure inducing relaxation via unconventional seventh excited state (see Fig. 19b) [80].

Next complex in this category is complex **85** (see Table 2) which has distorted tetrahedral geometry with $\{ErN_3C_{11}\}$ core. Ground states of both **85** and **85a** are

computed to be strongly axial but lack pure Ising nature. KD2 lies at 35.7 and 37.6 cm^{-1} above the KD1 in **85** and **85a**, respectively. This articulates that inclusion of counter-ion and solvent molecules poses hardly any impinge on the low-lying spectrum or the g-factors. KD1-g_{zz} is aligned towards the pseudo-C$_3$ axis passing through the Er-Cl bond vector. Considering the large matrix element pertinent to TA-QTM within $\pm\frac{9}{2}$ (0.28 μ_B) levels, relaxation is likely to occur via third excited KD outlining U_{cal} as 118 cm^{-1} for **85a**. Large discrepancy between U_{cal} and U_{eff} values attributes to intermolecular interactions/hyperfine interactions/pronounced QTM/multi-phonon relaxation pathways. Basis set assessment performed on this complex does not reveal prominent effect on barrier estimated with the increase of the proportional basis sets. Embedded cluster approach employed to account the impact of lattice and surroundings on anisotropy rendered resemblance in the anisotropic behaviour (similar to naked complex **85/85a**). Magneto-structural correlation was developed by increasing the Er-Cl distance, keeping all other structural parameters constant. Linear correspondence was reflected between increment of U_{cal} and Er-Cl bond distance. This owes to the unfavourable axial coordination of –Cl ligand with respect to Er^{III} ion and model calculation without Cl$^-$ (only three –N donors in equatorial plane) resulted in a large U_{cal} value (557 cm^{-1}). Following up to the foregoing concept, model calculations postulated that larger Er-Cl distance and small value τ are desired to fine-tune the local structural distortion as well as anisotropy around Er^{III} ion [101]. Model studies revealed that: (a) trigonal pyramidal or tetrahedral geometry is not appropriate geometry either for oblate/prolate ions to induce improved anisotropy and (b) trigonal pyramidal geometry is comparatively better than tetrahedral geometry for prolate ions and vice versa for oblate ions. Despite the unfavourable halide position around Er^{III} ion, effect of heavier halides on the nature of magnetic anisotropy was probed. Linear increase in U_{cal} value was observed as we move down the column (Group-17) towards the heavier halides. Enhancement of Er-halide covalency down the group-17 increases the Er^{III} vacant 5d orbital population and this directly correlates with the barrier enhancement (–F to –I) [102]. Structural analysis of **86** indicates two molecules with identical molecular formula within the unit cell (**86a**, **86b**). Complex **86** has a distorted bicapped square antiprismatic geometry with {ErO$_{10}$} core. Greater ∠NEr1N in **86a** compared to **86b** invokes varying orientation of coordinated chelating nitrates in these two molecules. Magnetic measurements implied zero-field SIM behaviour for **86** (see Tables 2 and 9 for molecular formula and barrier, respectively). KD1 in **86a** (g_{xx} = 1.03, g_{yy} = 2.77 and g_{zz} = 13.99) and **86b** (g_{xx} = 0.04, g_{yy} = 0.07 and g_{zz} = 15.78) revealed axiality with greater concomitant transverse anisotropy in **86a**. In both complexes, KD1-g_{zz} is aligned towards one of the O atoms of the coordinated nitrate ligand. In accordance with g-factors, KD1 in both complexes are predominantly $|M_J = \pm\frac{13}{2}>$ type with extensive admixing with other higher excited states marking low-symmetry nature of both complexes. Accounting for the matrix elements and KD2 transverse anisotropy components, U_{cal} value can be predicted as 48.9 and 104.9 cm^{-1} for **86a** and **86b**, respectively. The discrepancy in estimated barrier between two geometrical isomers can be ascribed to four and two O donor

ligands in the axial positions of **86a** and **86b**, respectively, along with the equatorial ligands. Additionally, greater deviation of Er^{III} ion symmetry against idealized bicapped square antiprismatic geometry in **86a** further supports the trend. Model studies articulated that in these types of complexes, removal of axial ligand/reduction in a number of axial ligands reduces the QTM tendency and proportionally enhances the energy barrier [103]. Next complex for this category is complex **87** which has square antiprismatic geometry with {ErN_8} core (see Table 2). Ab initio calculations on **87** led to theoretical barrier estimate of 58.7 cm^{-1} against U_{eff} value of 74 cm^{-1} (see Table 9). However, the wave function of the ground KD turns out to be: $|\pm\frac{1}{2}>$: 0.99 $|\pm\frac{1}{2}>$ with concomitant ground state crystal field parameter B_2^0 and g_{zz} as 1.01 and ~11 (see Table 9), respectively, for **87** [54]. KD1 g-factors turn out to be completely different to earlier observations: $g_{xx} = 10.77$, $g_{yy} = 8.33$ and $g_{zz} = 1.20$ which is a feature of $|\pm\frac{1}{2}>$ doublet state. Contrary to its Dy analogue (complex **3**), this shows positive crystal field parameter while **3** showed negative crystal field parameter. This indicates unfavourable ligand field rendering stabilization of $|\pm\frac{1}{2}>$ ground state with KD2 being predominantly $|\pm\frac{3}{2}>$ [54]. Calculations on **88**, which is a sandwich type complex (see Table 2), envisioned large separation between ground and low-lying excited states. Besides, KD1 and KD2 are computed to be strongly axial with collinearity between KD1 and KD2 principal magnetization axis alignment. Negligible transverse anisotropies for KD1 and KD2 suppress QTM and TA-QTM within KD1 and KD2, respectively, as corroborated by pertinent matrix elements of ~10^{-6} and ~10^{-3} μ_B, respectively. Accounting the collinearity between KD1 and KD2 g_{zz} axis, magnetization blockade is likely to be observed at KD3 which is supported by significant matrix element (3.7 μ_B) corresponding to TA-QTM process (see Table 9 and Fig. 20a). The Dy analogue (complex **2**) of **88** showed smaller energy barrier and weak SMM property. This reverse behaviour is
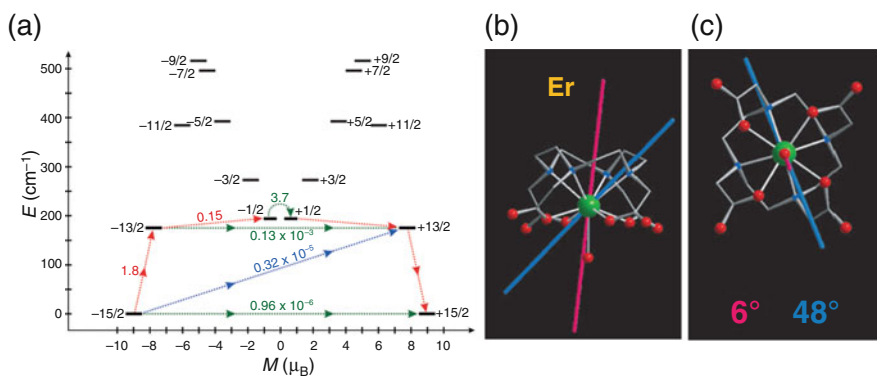
Fig. 20 (**a**) Magnetization blockade mechanism developed for complex **88**. Reprinted with permission from Ungur et al. [13] Copyright 2014 Wiley-VCH. Computed (blue) and experimental (pink) easy axis of magnetization orientation for **92** viewed (**b**) perpendicular and (**c**) parallel to the pseudo-fourfold symmetry axis of the molecule. Colour code: Er = green, O = red, N = blue and C = grey. Reprinted with permission from Boulon et al. [105] Copyright 2013 Wiley-VCH

essentially ascribable to the positive and negative CFP B_2^0 for **2** (0.35) and **88** (−1.52), respectively. This also is connected to the stabilization of $|\pm\frac{9}{2}>$ and $|\pm\frac{15}{2}>$ ground state in **2** and **88**, respectively [13]. Next three complexes (**89–91**) of this category are trigonal in geometry with $\{ErN_4O_3\}$ core. Ground–first excited gap in **89** turns out to be 54 cm^{-1} (see Table 9). This resulted in effective g parameters, i.e. $g^{eff}_\perp = 1.2$ and $g^{eff}_\parallel = 13.0$ (see Table 9) evoking easy-axis type anisotropy for **89** contrary to the easy plane behaviour for Dy analogue. Easy-axis anisotropy nature was supported by the ground multiplet wave-function type as predominantly $|\pm\frac{13}{2}>$: 68.4% $|\pm\frac{13}{2}>$ + 5% $|\pm\frac{7}{2}>$ + 10.4% $|\pm\frac{1}{2}>$ + 11.6% $|\mp\frac{13}{2}>$. This indicates lesser energy level admixture compared to Dy analogue [88]. Ab initio calculations were undertaken on complex **89** utilizing the measured crystal structures at 122 and 293 K. For **90** and **91**, the measured crystal structures at 122 K and room temperature were used. All these endeavours were aimed to compare the crystal field procured from the previously published optical spectra [101]. In this work, in addition to the CASSCF calculations, Madelung potential was approximated via five layers of point charges in order to appraise the impact of ligand field atmosphere (Madelung potential) on low-lying energy states. This delivers realistic charge distribution within the ligand field atmosphere composed by the underlying neutral molecules. All the point charges were positioned at the Cartesian position of every atom pertinent to crystal environment. The charges imposed on every atom in the ground state were adopted from foregoing CASSCF steps of the individual molecule. The ab initio computed first excited energy levels for the complex **89** at temperature 122 K resulted ground–first excited energy separation of 67 cm^{-1} $(B_2^0 = -1.05)$ and 58 cm^{-1} $(B_2^0 = -0.96)$ for bare molecule and for molecule embedded in five layers of point charges, respectively. Similarly, calculations at 293 K structure using bare molecule and molecule embedded in five layers of point charges led to the energy separation of 64 $(B_2^0 = -0.99)$ and 52 cm^{-1} $(B_2^0 = -0.88)$, respectively. All of these aforementioned energy levels acquired harnessing different approaches are in nice agreement with the energy extracted from Luminescence spectra (54 cm^{-1}). Even the computed higher energy excited doublets also agree well with the Luminescence energies. The g-values of the ground state procured from fitted Stevens parameters and ab initio calculations are noted as: $g_\parallel = 11.9/13.68$ and $g_\perp = 3.36/2.29$, respectively (see Table 9 for details). The overestimation of the g values can be ascribed to the underlying easy plane type anisotropy of the first excited energy level $(g_\parallel = 2.87$ and $g_\perp = 7.62)$. This articulates efficient impact of crystal field variation on the anisotropy of ground level which has low-lying first excited energy level (like in this case). The ab initio calculated energies along with g-factors of the ground multiplet of **90–91** are summarized in Table 9 [104]. Following up to this work, in another work, g-factors of complex **89** were estimated by different approaches. Due to the pseudo-C_3 symmetry in **89**, orientation of main magnetic axis procured from ab initio and electrostatic approaches resembles each other. However, electrostatic point-charge models render highly axial g-tensor values, contrasting the experimental observation. Additionally, harnessing the anisotropy data procured via aforementioned electrostatic approaches could neither reproduce the experimental

susceptibility or magnetization data. In similar context, minimum CASSCF+RASSI-SO approach with standard active space, considering the effects of Madelung potential and dynamic electron correlation offered energy level splitting equivalent to 75% of the experimental value. The remaining 25% of the ligand field splitting can be recovered via missing features of dynamic electron correlation and Madelung potential. The indispensability of ab initio calculations corresponds to its flexible nature as it permits mixing between metal and attached ligand orbitals, providing covalent contributions to the ligand field. As metal–ligand covalency is underestimated in the CASSCF approach, possibility of improving the accuracy to enhance splitting of the crystal field levels was probed. Inclusion of dynamic electron correlation (performing CASPT2 along with CASSCF) in conjunction with electrostatic Madelung potential of the crystal resulted computed magnetic data which is in agreement with experiments. Additionally, increase of active space by incorporating $5p^6$, $5d^0$, $6p^0$ and $5f^0$ orbitals (either by CASSCF or RASSCF approach) was found to impose prominent improvement of the energy level splitting [26].

Complex **92** is having a square antiprismatic geometry with {ErN_4O_4} core (see Table 2). KD1 of **92** possesses significant rhombic anisotropy as evident from the values $g_{xx} = 1.8$, $g_{yy} = 2.8$ and $g_{zz} = 10.9$. Easy axis of magnetization for KD1 in **92** is almost collinear (deviation by ~6°) to the $Er-O_w$ bond and the axial direction in the capped square antiprismatic geometry (see Fig. 20b, c). Despite this orientation, large discrepancy was detected between the computed and experimental anisotropy axis. This can be attributed to the considerable impact of incorporation of dynamic correlation on Er^{III} single-ion anisotropy. [35] f-SIM behaviour was noted for **92** with U_{eff} value of 27.1 (34.1) cm^{-1}. The calculated ground–first excited energy state difference of 19.8 cm^{-1} agrees well with the experimental value. The eight KDs of **92** spread within an energy window up to 427 cm^{-1} [105].

3.4 Review on Unconventional Ln^{III} Containing Single-Ion Magnets

Although the most common lanthanides (Dy^{III}, Er^{III} and to some extent Tb^{III}) remain pervasive, study of other uncommon lanthanides (Yb^{III}, Ce^{III}, Nd^{III}, Ho^{III} and Tm^{III}) also has gradually begun to transpire [119]. Particularly, Tb^{III} ion based SIMs are widely studied and the first SIM reported based on lanthanides is, in fact, [$Tb(Pc)_2$]$^-$ complex possessing very large U_{eff} value and attractive blocking temperature [113]. Here, we present selected examples of SIMs based on not only Tb^{III} ion but also other lanthanides. The Yb^{III}, Ce^{III}, Nd^{III}, Ho^{III}, Tm^{III} and Tb^{III} are represented by their term symbols as $^2F_{7/2}$, $^2F_{5/2}$, $^4I_{9/2}$, $^5I_8$, $^3H_6$ and $^7F_6$. Among these, Ce^{III}, Nd^{III}, Ho^{III} and Tb^{III} are oblate and Yb^{III} and Tm^{III} are prolate ions, respectively. In this section, we intend to cover the ab initio calculations on Ln^{III}-based SIMs. Besides, as on date, no zero-field SIM feature been reported for Pr^{III}/Sm^{III} complexes, and
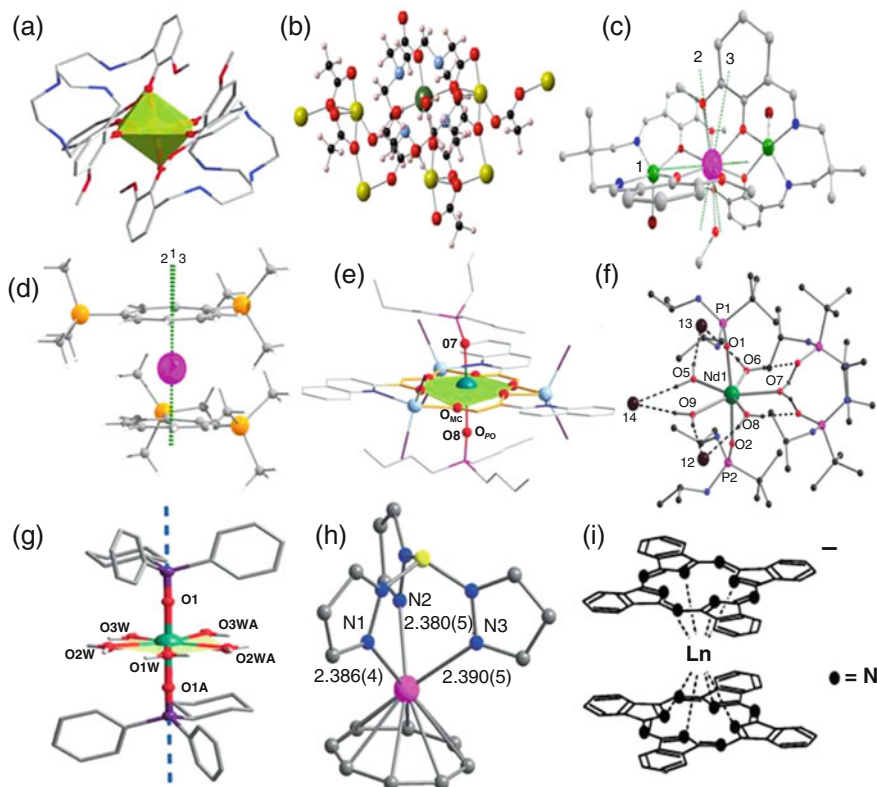
Fig. 21 (**a–i**) Molecular structures of complexes **93**, **94**, **101**, **102**, **103**, **105**, **109**, **110** and **112**, respectively. Arrows/dashed lines in complexes show the orientation of the principal magnetization axis. Complexes with more than one arrow are showing g_{zz} axis for the same numbers of KD states. Colour code: central atom(s) = Dy, red = O, dark-blue/light-blue = N, black/dark-brown/light-brown = C, dark green = Na, golden yellow = Si, yellow = S and white = H atoms. Reprinted from Li et al. [109], Gupta et al. [110] with permission from the Royal Society of Chemistry. Reprinted from Boulon et al. [105], Singh et al. [108], Chen et al. [111], Meng et al. [112] with permission from John Wiley and Sons. Reprinted with permission from Ishikawa et al. [113] Copyright@2003 American Chemical Society. Reprinted with permission from Liu et al. [106] Copyright@2012 American Chemical Society

therefore those are also discarded from our confined study. First complex of this category is complex **93** which has trigonally distorted octahedron geometry with {YbO$_6$} core (see Fig. 21a and Table 2 for molecular formula). Complex **93** was noted as the first Yb^{III}-based complex showing easy plane anisotropy. Complex **93** exhibited f-SIM behaviour with U_{eff} of 4.9 cm^{-1} (see Table 9). KD1 in **93** possesses large transverse anisotropy as evident in the estimated values $g_{xx} = 3.21$, $g_{yy} = 2.69$ and $g_{zz} = 1.76$ (see Table 9). KD1 rhombicity promotes strong QTM within the ground state, discarding the possibility of SIM behaviour in the absence of external applied field. Eigenfunctions of the KD1 can be represented as: $-0.02 \left| \frac{7}{2} \right> -0.02 \left|$

$-\frac{7}{2} > +0.65|\frac{5}{2}> +0.67|-\frac{5}{2}> -0.26|\frac{1}{2} > +0.25|-\frac{1}{2}>$. This reveals that **93** does not comply with the requirement of the largest $| M_J = \pm\frac{7}{2} >$ as the ground state. Rather, contribution from $| M_J = \pm\frac{7}{2}>$ is meagre, with extensive mixing from other energy levels. This was further corroborated by the KD1 g_{zz} value which is far from the expected g_{zz} value of KD8 for the stabilized $| M_J = \pm\frac{7}{2} >$ level. KD2 is located at 187.9 cm^{-1} higher in energy and remains far from experimental value. Therefore, slow magnetization relaxation in **93** corresponds to direct process while Orbach relaxation pathway is discarded completely [106]. Next set of complexes for this category is complexes **94–97** (Yb^{III} (**94**), Tb^{III} (**95**), Ho^{III} (**96**) and Tm^{III} (**97**), see Fig. 21b). They have {LnO$_4$N$_4$} core with square antiprism geometry. Among these four complexes, only complex **94** shows field-induced SMM behaviour. KD1 of **94** has improved axiality compared to **93**, with $g_{xx} = 0.1$, $g_{yy} = 1.0$ and $g_{zz} = 6.8$. Easy axis of magnetization for KD1 in **94** is almost collinear (deviation by ~12°) to the Yb-O$_w$ bond and the axial direction in the capped square antiprismatic geometry. f-SIM behaviour was noted for **94** with U_{eff} value of 20.2 cm^{-1}. The calculated ground–first excited energy state difference is estimated as 197.2 cm^{-1}. The eight KDs of **94** spread within an energy window of 416 cm^{-1} with larger g_{zz} value corresponds to $| M_J = \pm\frac{7}{2}>$ ground state [105]. SIM behaviour was missing for complexes **95–97**.

Easy axis of magnetization for KD1 in **95** is perpendicular (deviation by ~85°) to the Tb-O$_w$ bond and the axial direction in the capped square antiprismatic geometry. Considering the non-Kramers nature of the Tb^{III}, Ho^{III} and Tm^{III} in **95**, **96** and **97**, respectively, tunnel splitting (Δ_{tun}) within the ground energy multiplets acts as dictating factor for SIM behaviour ($\Delta_{tun} = 1.6$, 4.8 and 4.6 cm^{-1} were evaluated for **95**, **96** and **97**, respectively). Within the ground energy multiplet, this large separation precludes the presence of magnetic bistability deterring SIM behaviour in all these three complexes. Besides, KD1 in all three complexes possess significant transverse anisotropy inducing magnetization blockade within ground states itself [105]. Easy axis to easy plane type ground state anisotropy transformation was noted upon changing the axial water ligand from **98** to axial fluoride ligand in **99/100**. All these three complexes have capped square antiprismatic geometry. Complexes **99** and **100** possess identical coordination environment, with {LnO$_4$N$_4$F$_1$} core, except the Yb-F bond length which is 1.97 Å and 2.38 Å for **99** and **100**, respectively. The KD1 main magnetic factors for **98–100** nicely corroborated the change of anisotropy behaviour (see Table 9). This ascribes to the weaker equatorial crystal field of employed DTMA (diethylene triamine penta acetic acid) ligand which stabilizes the prolate $|M_J = \pm\frac{7}{2} >$ state. Coordination of the F$^-$ over the fourfold axis creates prevalent axial crystal field unfavourable for prolate ions. This instigates stabilization of $|M_J = \pm\frac{1}{2}>$ as the ground state. Compared to the neutral water ligand, replacement by negatively charged fluoride in axial direction is found to be detrimental for the SIM behaviour [107]. Complexes **101** and **102** are Ce^{III} ion based SIMs, with former complex having nine oxygen atoms coordinated to Ce^{III} ion whereas latter is having π-coordination (η^8-fashion) – where C atoms coordinated to Ce^{III} ion (see Fig. 21c, d). Complex **101** shows axial type KD1 anisotropy with

stabilization of $|M_J = \pm\frac{5}{2}>$ state, substantiating zero-field SIM behaviour (see Table 9). KD1-g_{zz} is aligned towards one of the O donors of the bridging ligands and diverged from Ce-O bond vector/Zn-Ce-Zn axis by 11°/20.8°, respectively. Accounting for matrix elements and g-factors of KD2, relaxation is likely to channel via KD2 outlining U_{cal} value as 180 cm^{-1} (see Table 9). Model calculations revealed that intermolecular interaction (point charges) and increase of active space/basis set have no significant role on the nature of anisotropy. The eight KDs in **101** and **102** span over an energy window of 488 and 1,036 cm^{-1}, respectively. This infers the presence of stronger metal–ligand covalent interaction in **102**. However, larger transverse component with small g_{zz} values of KD1 stabilizes $|M_J = \pm\frac{1}{2}>$ state in **102** and rationalized by the presence of stronger equatorial ligand field. This corresponds to stronger QTM within ground state (matrix element = 0.79 μ_B) and entails the need of application field ratifying its f-SIM feature (see Table 9). Stabilization of $|M_J = \pm\frac{5}{2}>$ and $|M_J = \pm\frac{1}{2}>$ in **101** and **102**, respectively, was nicely endorsed by computed CFP $B_2^0 = -23.35$ and +17.61, respectively. Complex **101** shows ideal crystal field but lacks symmetry whereas **102** with higher symmetry is devoid of suitable ligand field. This articulates the simultaneous need of ideal symmetry and crystal field to achieve improved SIM behaviour. Model calculations indicated that lower coordination number [120] and coordination no 5/7 possessing trigonal bipyramidal or pentagonal bipyramidal geometries are appropriate to procure larger barrier [108].

Complexes **103–104** have distorted hexagonal bipyramidal geometry around central metal ion with {LnO$_8$} core (see Fig. 21e and Table 2). Complex **103** is having Ce^{III} paramagnetic ion and complex **104** has analogous Nd^{III} paramagnetic ion. KD1 for complex **103** is computed to compose of: 96% $|\pm\frac{3}{2}>$ (f-SIM) with predominant g_{zz} values and negligible transverse anisotropy (See Table 9). The ground–first excited energy separation (303 cm^{-1}) is larger than the reported U_{eff} value (see Table 9) discarding the relaxation probability via Orbach process. This articulates that predominant relaxation pathway is likely to be Raman process with direct process involved in substantial fields and QTM pathway prevails in zero field. Complex **104** (f-SIM) is isostructural with **103** with KD1 representation as: 71% $|\pm\frac{9}{2}>$ +29% $|\pm\frac{3}{2}>$. Here as well, due to larger ground–first excited level gap (104 cm^{-1}), underlying relaxation mechanism delineation resembles to that discussed for **103**. Experimental data postulated that the $g_{zz} \sim 5$–5.5 for axial type KD1 in **104** which is larger than computed one (see Table 9). It is notable that harnessing computed anisotropy properties are in nice agreement with experiments [109]. Complex **105** is seven-coordinated Nd^{III} complex with {NdO$_7$} core (see Fig. 21f). Five KDs pertaining to $^4I_{9/2}$ ground level of Nd^{III} in complex **105** spread within an energy window of 416 cm^{-1}. KD1 is found to be axial (see Table 9) with stabilization of $|M_J = \pm\frac{9}{2}>$ state. KD1-g_{zz} lies in proximity to the O of (O=P−) atom of the phosphonic amide ligand (along C$_5$ axis but deviated by ~5°). KD2 possesses large transverse anisotropy ($g_{xx} = 0.10$, $g_{yy} = 0.42$ and $g_{zz} = 5.10$) implying possible relaxation via this state (see Table 9). Wave-function analysis postulated KD2 as mixture of $|M_J = \pm\frac{5}{2}>$ and $|M_J = \pm\frac{1}{2}>$ levels. CASSCF LoProp

charges showed prominently larger negative charges on the axial O atoms compared to their equatorial congeners rendering $|M_J = \pm\frac{9}{2}>$ as the ground state [110]. Complex **106** is isostructural to complex **87** but with Ho^{III} ion instead of Dy^{III} ion. KD1 is calculated to have $g_{zz} = 19.16$ and $B_2^0 = -0.85$ (see Table 9). Considering integer angular momentum quantum number of Ho^{III} ion, all the energy states are found to be strongly mixed [54]. The ab initio calculated ground–first excited gap (12.9 cm^{-1}) agrees well with that procured from the crystal field approach (15/19 cm^{-1}; see Table 9) [54].

Like complex **106**, next three complexes are (**107–109**) also Ho^{III} ion based SIMs with the energy spectrum for 17 energy levels (seven pseudo-doublets and three singlets) of the ground $^5I_8$ multiplet for the Ho^{III} ion shows showing energy span of 204 and 207 cm^{-1} for **107** and **108**, respectively. Complexes **107** and **108** are trigonal prismatic in geometry with three agostic interaction between Ln and H atoms. Complex **109** has distorted pentagonal bipyramidal geometry with {HoO$_7$} core (see Fig. 21g). Ground pseudo-doublets of **107** and **108** are Ising type with g_{zz} of 17.10 and 16.92, respectively. Wave-function analysis articulates predominantly $|\pm M_J = 7>$ type ground state with mixing from other higher states and this was corroborated by the $g_{zz} = 17.5$ expected for pure $|\pm M_J = 7>$ state. The Δ_{tun} is noted as 0.04 and 0.07 cm^{-1} for **107** and **108**, respectively, precluding magnetic bistability and SIM behaviour. Positive value of ground state CFP $B_2^0 = 1.00$ and 0.93 for **107** and **108**, respectively, endorses for unfavourable crystal field and completely suppressed SIM behaviour [81]. Complex **109** is a rare zero-field SIM where compressed pseudo-D$_{5h}$ environment around Ho^{III} reduces its inherent QTM probability as well as mixing of different $|\pm M_J>$ levels. KD1 possesses g_{zz} of 19.86 (see Table 9) and approaches towards that expected for pure $|\pm M_J = 8>$ state of 20. The $\Delta_{tun} = \sim 10^{-4}$ cm^{-1} was noted within ground pseudo-doublets provoking possible relaxation via higher excited energy levels. Though the Δ_{tun} within first excited pseudo-doublet was considerable enough, transition moment matrix element corresponding to the ± 1 and ± 2 was not pronounced. Substantial Δ_{tun} within ± 3 in conjunction with matrix elements within ± 2 and ± 3 spurs relaxation via this state (see Table 9) [111].

Complexes **110–111** are Tm^{III} ion based complexes with three N atoms from an η^3-coordinated tridentate pyrazolylborate anion and η^8-coordinated COT dianion (see Fig. 21h). Complex **111** is the same as complex **110** except methyl substitution in Tp*. Dynamic magnetization experiments revealed slow magnetization relaxation for **110** and **111** in applied static *dc* magnetic field whereas corresponding diluted samples exhibit relaxation even at zero field. Both **110** and **111** exhibit nearly degenerate ground states with $\Delta_{tun} = 0.01$ and 0.02 cm^{-1}, respectively, denoting faster QTM in **111**. Non-coincidence between ground and first excited pseudo-doublets indicated plausible magnetization blockade via this first excited level (128.8° and 85.9° for **110** and **111**, respectively). Additionally, huge Δ_{tun} of 19.36 and 2.93 cm^{-1} in **110** and **111**, respectively, necessitates relaxation to be channelled via this state (see Table 9). The larger ground–first excited gap can be attributed to the differences between 4f charge density of ground $|\pm M_J = 6>$ and $|\pm$

$M_J = 5>$ states. The improved barrier of **110** corresponds to better molecular symmetry (see Table 9) and steric hindrance arose from –Me groups in **111**. Due to this, comparatively longer Tm-N bonds in **111** exert inherently weaker crystal field. Further, ground pseudo-doublet wave-function analysis for **110** and **111** as: $0.96 |\pm 6 > +0.03 |\pm 3>$ and $0.92 |\pm 6 > +0.04 |\pm 4 > +0.02 |\pm 2 >$, respectively, reinforced better SIM behaviour in **110** [112].

The highly anisotropic ground states of the Tb^{III} ion, which are oblate in nature and prefer strongly axial ligand fields, can be stabilized in sandwich complexes. Ishikawa and co-workers, in 2003, have reported first Ln^{III}-based mononuclear sandwich complexes, $[TbPc_2]^-$ complex (where Pc = phthalocyanine) (**112**), with very large barrier height for spin reversal (216 cm^{-1}) which surpassed all the records of barrier heights reported for any mono$-$/polynuclear transition metal complexes at that point in time. It has to be noted that phthalocyanine/porphyrin type macrocycles are not considered as classical η-type capping ligands because their coordination mode is more σ-type, similar to the multidentate chelating ligands. Therefore, the CF symmetry of such a ligand can be regarded as pseudo C_4 [113]. Next three complexes (**113–115**) are Tb^{III} ion based SMMs with $\{TbN_6H_3\}$ core for the **113** and **114** and $\{TbN_4\}$ core for the complex **115**. The energy spectrum for 13 energy states (six pseudo-doublets and one singlet) of ground $^7F_6$ atomic multiplet of Tb^{III} in **113** and **114** spans within an energy window up to 590 and 515 cm^{-1}, respectively. The ground pseudo-doublets are pure Ising type (see Table 9) and approaching towards that expected for pure $|\pm M_J = 6>$ state of ~18. The ground pseudo-doublets are detected with $\Delta_{tun} = 0.02$ and 0.05 cm^{-1} for **113** and **114**, respectively, entailing f-SIM behaviour in both complexes. However, significant $\Delta_{tun} = 0.03$ and 0.04 cm^{-1} within first excited pseudo-doublet of **113** and **114**, respectively, inevitably blocks magnetization via this state (see Table 9 for barrier values) [81]. Ab initio calculations on complex **115** confer $|\pm M_J = 6>$ as the ground pseudo-doublet possessing Δ_{tun} of 0.03 cm^{-1}. This large intrinsic tunnelling gap necessitates use of external static *dc* applied magnetic field to quench QTM and observe SIM behaviour. Now, first excited pseudo-doublet lying at ~228 cm^{-1} with Δ_{tun} of 0.65 cm^{-1} undoubtedly spurs relaxation via this state. This turns out to be larger than the Δ_{Orbach} energy barrier (12.2±0.5 cm^{-1}) procured from magnetic measurements. This infers the necessary consideration of other relaxation pathways within temperature range. Therefore, the relaxation is likely to occur via combined effects of QTM, direct and Raman pathways which is reminiscent of the mechanism discussed for its Dy analogue (complex **44**) [79].

Next four set of complexes for this category are Tb^{III} double-decker complex with $\{TbN_8\}$ core and square antiprismatic geometry (**116–119**, see Fig. 22). Complexes **116** and **119** are heteroleptic whereas complexes **117** and **118** are homoleptic in nature. Inclusion of the bulky strong electron-donating (dibutylamino) groups on the periphery positions of either phthalocyanine ligands offers strong ligand field with unsymmetrical molecular structure and radical-4f interactions. These factors result in appearance of both large energy barrier and high magnetic blocking temperatures [114–117].
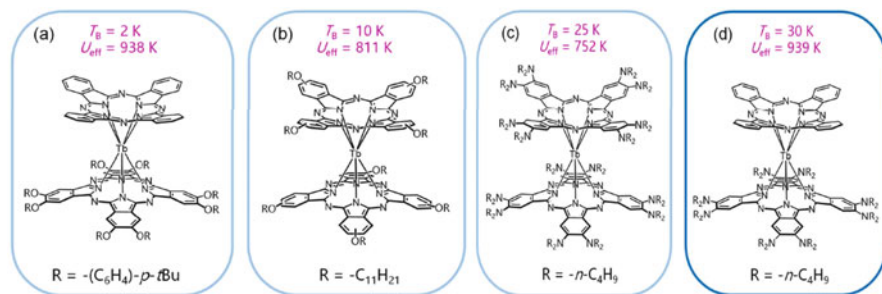
Fig. 22 (**a–d**) Molecular structures along with blocking temperature and effective energy barrier for complexes **116–119**, respectively. Reprinted with permission from Chen et al. [117] Copyright@2017 American Chemical Society

4 Conclusions

Controlling ligand geometry and point group symmetry could help chemists to aim appropriate complexes with significantly large magnetization blockade barrier. In spite of the progress made till date, it is clear that thorough theoretical calculations are required to predict promising molecular systems that are worth to synthesize using experimental means. Designing ligands with appropriate symmetry is extremely important to fine-tune the U_{eff} and also to enhance T_B beyond liquid N_2 temperatures. As the stabilization of the largest M_J level as the ground state and the crystal field splitting of the M_J levels are the most desired characteristics of lanthanide based SMMs, we have summarized various Dy^{III} SIMs based on their ground state $|\pm M_J>$ levels and the computed crystal field splitting to six different categories that are discussed above (A to F). We have also considered Er^{III}/Tb^{III} SIMs with f-SIM or zf-SIM properties reported for our analysis.

To summarize, we have plotted all the different geometries of Dy^{III} complexes (along x-axis) from all the six categories with respect to their U_{cal} values reported (y axis, see Fig. 23). Out of 16 geometries studied, pentagonal bipyramidal geometry found to yield both large as well as small U_{cal} values based on its axial and equatorial ligand field strength. Those molecules with strong axial ligand field with weak equatorial ligand field yield very large U_{cal} values with attractive blocking temperatures. However, if the ligand field strength is reversed, i.e. strong equatorial ligation and weak axial ligation yields smaller U_{cal} values. This particular geometry clearly illustrates how important it is to design the strength of the donor ligands to obtain attractive magnetic properties.

The second category is Dy^{III} ion based metallocene complexes; here as well, both smaller and larger U_{cal} values are possible depending on the nature of the coordinating ring. Sandwich complexes with large aromatic rings interact with the equatorial electron density of the Dy^{III} ion leading to smaller U_{cal} values as one can witness in [Dy(COT)$_2$] complexes. Whereas, sandwich complexes with small aromatic rings, such as Cp*, are found to yield very large U_{cal} values due to strong axial
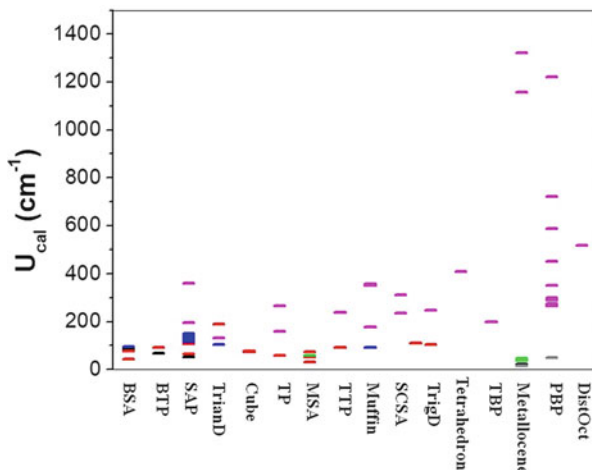
Fig. 23 Plot representing U_{cal} values for different complexes of all six categories with respect to their geometries. Colour code for categories: black = A, red = B, green = C, blue = D, magenta = E and grey = F. *BSA* bicapped square antiprismatic, *BTP* bicapped triangular prism, *SAP* square antiprismatic, *TrianD* triangular dodecahedron, *TP* trigonal prismatic, *MSA* monocapped square antiprismatic, *TPP* tricapped trigonal prismatic, *SCSA* spherical capped square antiprismatic, *TrigD* trigonal dodecahedron, *TBP* trigonal bipyramidal, *PBP* pentagonal bipyramidal, *DistOct* distorted octahedral

ligand field exerted by this ligand in stabilizing $|\pm M_J = \frac{15}{2}>$ ground state and destabilizing the $|\pm M_J = \frac{1}{2}>$ state (see Fig. 24). Besides, higher symmetry helps to quench the tunnelling leading to relaxation via higher excited state resulting in a very large U_{cal} values. If the ring sizes of the sandwich complexes are chosen aptly, this can lead to a significant breakthrough as has been witnessed with a blocking temperature of 60 K. However, one of the main issues with such systems is stability of these organometallic SMMs under ambient conditions as this is desired in the next logical step of fabricating devices from these molecules.

Tetrahedron is another possible geometry where one can get high U_{cal} value. Perfect octahedral complexes are found to relax via ground state KD. But, if the structures are distorted significantly, this found to yield large U_{cal} values. Bicapped square antiprismatic, bicapped triangular prism, cube and monocapped square antiprismatic geometries are not the desired ones as they yield very low U_{cal} values, independent of the choice of the donor ligands. Based on the studied examples, one can achieve U_{cal} value of 95 cm^{-1}, 93 cm^{-1}, 75 cm^{-1} and 73 cm^{-1}, respectively, for these geometries. Many examples are reported in the literature where complexes with these geometries are found to exhibit not even f-SIM characteristics. Remaining nine geometries (see Fig. 23) are found to yield mixture of both large as well as small U_{cal} values based on the distortion and ligand field strength. For square antiprismatic geometries, one can achieve a max U_{cal} value as high as 362 cm^{-1}. For this geometry, among our studied complexes, the minimum reported U_{cal} value is 52 cm^{-1}. In the same way, for remaining eight geometries, triangular dodecahedron,
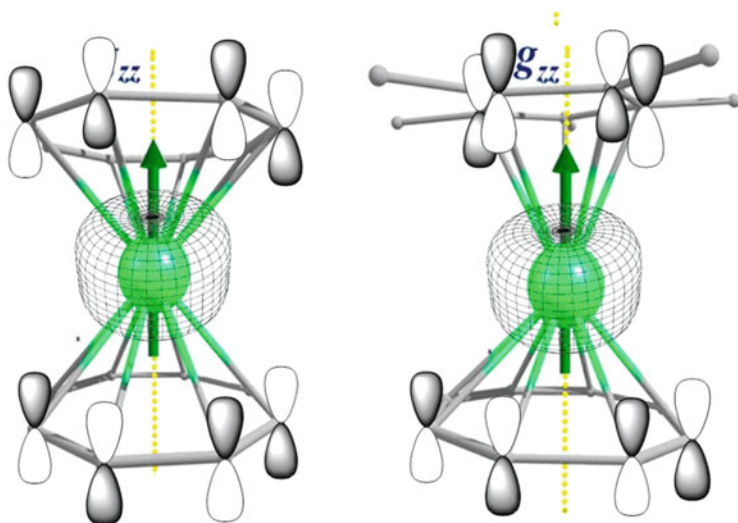
Fig. 24 Pictorial presentation of two different molecules with: (**a**) two C_8 rings around Dy^{III} ion and (**b**) one C_8 and second C_5 ring around Dy^{III} ion along $|\pm M_J = \frac{15}{2}>$ charge distribution suggesting strong axial ligand field geometry maintained for the second molecule with a C_5 ring with respect to the first molecule with C_8 rings

trigonal prismatic, tricapped trigonal prismatic, muffin, trigonal dodecahedron, spherical capped square antiprismatic, tetrahedron and trigonal bipyramidal, the maximum to minimum reported U_{cal} are found to be 104/189, 59/267, 91/239, 92/356, 105/249, 237/313 and 199/199 cm^{-1}, respectively. For a given geometry, it is preferable to have oxygen donor ligands along the axial directions than nitrogen donors as the former exerts stronger crystal field interaction than the latter. This is one of the desired conditions when we have mixed N, O donor ligands, to obtain large U_{cal} values in Dy^{III} SIMs.

We have plotted all different studied geometries of Er^{III} and Tb^{III} complexes (along x-axis) with respect to their U_{cal} values reported (y axis, see Fig. 25). Out of all the studied geometries for Er^{III} complexes, trigonal planar is found to yield the highest U_{cal} value (331 cm^{-1}) because of strong equatorial ligand field around Er^{III} ion with no ligation along axial direction. The Er^{III} sandwich complexes can yield both large as well as small U_{cal} values (85–280 cm^{-1}) based on the size of the ring and whether it exerts axial or equatorial ligand field? Those molecules with strong equatorial ligand field in the presence or absence of weak axial ligand field found to yield larger U_{cal} values and this is eventually translated into attractive blocking temperatures. However, if the ligand field strength is reversed, this yield smaller not desired U_{cal} values. Er^{III} complexes with tetrahedral geometry are found to achieve U_{cal} value as high as 118 cm^{-1}. Besides, Er^{III} ion in the distorted monocapped octahedron geometry is found to yield U_{cal} value between 16 and 54 cm^{-1}. Remaining three geometries (square antiprism, trigonal bipyramidal and bicapped square antiprismatic) yield U_{cal} values smaller than 50 cm^{-1}.

Fig. 25 Plot representing U_{cal} values for different complexes of Er^{III} and Tb^{III} with respect to their geometries. Colour code: black = Er^{III} and red = Tb^{III}. *SAP* square antiprismatic, *Trig Plan* trigonal planar, *TBP* trigonal bipyramidal, *Td* tetrahedral, *BSAP* bicapped square antiprismatic, *DMOh* distorted monocapped octahedron, *DD* double decker, *Trig Pris* trigonal prismatic
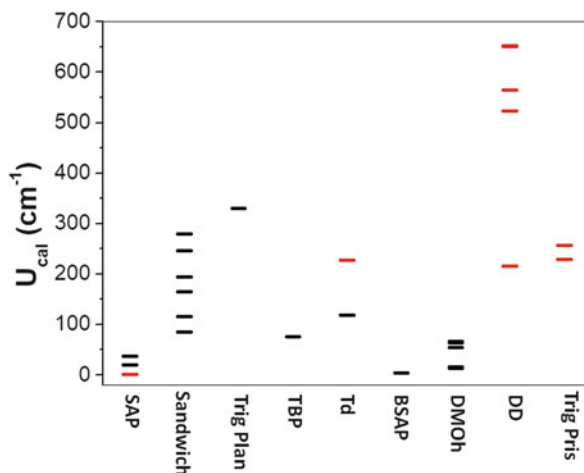
Out of all the geometries studied for Tb^{III} complexes, double-decker complexes are found to yield very high U_{cal} value (653 cm^{-1} $\leq$ U_{cal} $>$ 216 cm^{-1}). Tetrahedral and trigonal prismatic geometries also found to yield high U_{cal} value such as 228 cm^{-1} and 257 cm^{-1}, respectively. The Tb^{III} ion square prismatic geometries are found to be not suitable for obtaining large U_{cal} values as the relaxation in most of the instances occurs through ground state or through first excited state, which is found to be very close to the ground state.

Besides these coordination complexes based on lanthanide ions, there are also other classes of SMMs where the role of theory in predicting potential targets is well highlighted. This includes synthesis and characterization of various Dy^{III} ion based endohedral fullerene molecules. Several such molecules are predicted to possess attractive magnetic properties and recently some of those molecules are synthesized and characterized. Experiments essentially confirm the predictions at least in three reported cases, and this highlights the role of ab initio calculations in the design and development of lanthanide based SIMs.

4.1 Future Outlook

In this section, we intend to describe the future outlook in the area of ab initio calculations and how one could possibly solve the existing issues? The limitations and accuracy of the methodology employed are already described; while some work to correct such problems are undertaken already, this area still needs to catch with the parallel development on new theoretical methods. Here, we highlight a few issues which could be targeted in the near future:

1. One of the limitations of the widely employed CASSCF methodology is the restriction on the reference space employed. While this methodology is highly successful for lanthanide based systems, employing these methods for radical-4f and {3d-4f} clusters is challenging as computations are often limited by the number of orbitals/electrons that can be considered within the chosen reference space.

2. For polynuclear lanthanide complexes, often fragment approach is employed where individual lanthanide ion anisotropies are computed and eventually coupled together using Lines model to derive relaxation mechanism. While this approach has been employed successfully for several systems, if the number of exchange interaction increases, this generates the familiar problem of over parameterization in fitting procure. Thus, one has to adapt other possible theories such as density matrix renormalization group (DMRG or DMRG-PT2) or multi-reference coupled cluster (MR-CCSD(T)) methods where there is a possibility to perform calculations on full systems. While these methodologies are already available and are tested for various systems, applications in lanthanide based SIMs/SMMs are yet to be carried out.

3. While the relaxation mechanism derived from ab initio calculations are very useful, the accuracy of the relaxation mechanism needs to be improved tremendously to have a meaningful comparison with experimental observations. Modelling spin–spin, spin–lattice and other relaxation processes are of utmost importance to bridge the gap and to make robust predictions. Employing Pauli master equation to derive other mechanistic features has been highlighted recently in several examples [21, 121, 122], and further work in this direction needs to be carried out on a priority basis to improve our understanding of the mechanism of relaxation.

4. Estimation of blocking temperature and relaxation time for SIMs/SMMs is extremely important. The blocking temperatures in lanthanide SMMs are often unpredictable and there is a large difference between the U_{eff} and T_B values. At present, T_B values are obtained only by experimental means and computing this parameter is very intricate and one has to go beyond molecular calculations to accurately reproduce such important parameters. Development in this direction is desired.

5. While it is known that spin is a dynamic quantity, calculations are often performed on static structure and there are only a few instances where the structural dynamics of the complexes are taken into account [121]. This is fundamentally important problem, as many of the molecules reported have fluxional behaviour and thus are expected to fluctuate significantly even at low temperatures. Methodologies coupling molecular dynamics and ab initio calculations are to be developed to further enhance our understanding.

6. Viable predictions from the calculations offer important clues to the experimentalist to design and develop new generation SMMs. Predictions often need accurate geometries and these are (albeit limited) often performed at present using density functional methods. While it is known that DFT has inherent problems in addressing degenerate states, methodologies which are superior

need to be adapted to offer accurate structures which in turn will lead to reliable predictions.

References

1. Miller JS, Epstein AJ (2000) MRS Bull 25:21–30
2. Yamashita M, Katoh K (2017) Molecular magnetic materials. Wiley-VCH Verlag GmbH, KGaA, Weinheim, pp 79–101
3. Aldoshin SM, Korchagin DV, Palii AV, Tsukerblat BS (2017) Pure Appl Chem 89:1119
4. Cornia A, Costantino AF, Zobbi L, Caneschi A, Gatteschi D, Mannini M, Sessoli R (2006) In: Winpenny R (ed) Single-molecule magnets and related phenomena. Springer, Berlin, Heidelberg, pp 133–161
5. Coulon C, Miyasaka H, Clerac R (2006) Single-molecule magnets and related phenomena, vol 122. Springer, Berlin, Heidelberg, pp 163–206
6. Gatteschi RSD, Villain J (2006) Molecular nanomagnets. Oxford University Press, Oxford
7. Pedersen KS, Vindigni A, Sessoli R, Coulon C, Clérac R (2017) Molecular magnetic materials. Wiley-VCH Verlag GmbH, KGaA, Weinheim, pp 131–159
8. Gao S (2015) Molecular nanomagnets and related phenomena. Springer, Berlin, Heidelberg
9. Benelli C, Gatteschi D (2015) Introduction to molecular magnetism. Wiley-VCH Verlag GmbH, KGaA, Weinheim, pp I–VII
10. Kahn O (1993) Molecular magnetism. VCH Publishers, Orsay
11. Ruiz E, Alvarez S, Rodriguez-Fort A, Alemany P, Pouillon Y, Massobrio A (2001) In: Miller JS, Drillon M (eds) Magnetism: molecules to material, vol 2. Wiley-VCH, Weinheim, p 227
12. Clemente-Juan JM, Coronado E, Gaita-Ariño A (2015) Lanthanides and actinides in molecular magnetism. Wiley-VCH Verlag GmbH, KGaA, Weinheim, pp 27–60
13. Ungur L, Le Roy JJ, Korobkov I, Murugesu M, Chibotaru LF (2014) Angew Chem Int Ed Engl 53:4413–4417
14. Luzon J, Sessoli R (2012) Dalton Trans 41:13556–13567
15. Sessoli R, Powell AK (2009) Coord Chem Rev 253:2328–2341
16. Jiang S-D, Wang B-W, Gao S (2014) In: Gao S. (ed) Molecular nanomagnets and related phenomena, Springer, Berlin, pp 1–31
17. Tang J, Zhang P (2015) Lanthanide single molecule magnets. Springer, Berlin
18. Liu J, Chen Y-C, Jia J-H, Liu J-L, Vieru V, Ungur L, Chibotaru LF, Lan Y, Wernsdorfer W, Gao S, Chen X-M, Tong M-L (2016) J Am Chem Soc 138:5441–5450
19. Chen Y-C, Liu J-L, Ungur L, Liu J, Li Q-W, Wang L-F, Ni Z-P, Chibotaru LF, Chen X-M, Tong M-L (2016) J Am Chem Soc 138:2829–2837
20. Gupta SK, Rajeshkumar T, Rajaraman G, Murugavel R (2016) Chem Sci 7:5181–5191
21. Goodwin CAP, Ortu F, Reta D, Chilton NF, Mills DP (2017) Nature 548:439–442
22. Guo F-S, Day BM, Chen Y-C, Tong M-L, Mansikkamäki A, Layfield RA (2017) Angew Chem Int Ed 56:11445–11449
23. Meng Y-S, Jiang S-D, Wang B-W, Gao S (2016) Acc Chem Res 49:2381–2389
24. Liddle ST, van Slageren J (2015) Chem Soc Rev 44:6655–6669
25. Dreiser J (2015) J Phys Condens Matter 27:183203
26. Ungur L, Chibotaru LF (2017) Chem Eur J 23:3708–3718
27. Chibotaru L (2015) Theoretical understanding of anisotropy in molecular nanomagnets. In: Gao S (ed) Molecular nanomagnets and related phenomena, vol 164. Springer, Berlin, Heidelberg, pp 185–229

28. Ungur L, Chibotaru LF (2015) Lanthanides and actinides in molecular magnetism. Wiley-VCH Verlag GmbH, KGaA, Weinheim, pp 153–184
29. Aquilante F, Autschbach J, Carlson RK, Chibotaru LF, Delcey MG, De Vico L, Fdez Galván I, Ferré N, Frutos LM, Gagliardi L, Garavelli M, Giussani A, Hoyer CE, Li Manni G, Lischka H, Ma D, Malmqvist PÅ, Müller T, Nenov A, Olivucci M, Pedersen TB, Peng D, Plasser F, Pritchard B, Reiher M, Rivalta I, Schapiro I, Segarra-Martí J, Stenrup M, Truhlar DG, Ungur L, Valentini A, Vancoillie S, Veryazov V, Vysotskiy VP, Weingart O, Zapata F, Lindh R (2016) J Comp Chem 37:506–541
30. Aquilante F, De Vico L, Ferre N, Ghigo G, Malmqvist PA, Neogrady P, Pedersen TB, Pitonak M, Reiher M, Roos BO, Serrano-Andres L, Urban M, Veryazov V, Lindh R (2010) J Comp Chem 31:224–247
31. Duncan JA (2009) J Am Chem Soc 131:2416–2416
32. Swerts B, Chibotaru LF, Lindh R, Seijo L, Barandiaran Z, Clima S, Pierloot K, Hendrickx MFA (2008) J Chem Theory Comput 4:586–594
33. Veryazov V, Widmark PO, Serrano-Andres L, Lindh R, Roos BO (2004) Int J Quantum Chem 100:626–635
34. Karlstrom G, Lindh R, Malmqvist PA, Roos BO, Ryde U, Veryazov V, Widmark PO, Cossi M, Schimmelpfennig B, Neogrady P, Seijo L (2003) Comput Mater Sci 28:222–239
35. Malmqvist PA, Roos BO, Schimmelpfennig B (2002) Chem Phys Lett 357:230–240
36. Chibotaru LF, Ungur L (2012) J Chem Phys 137:064112–064122
37. Chibotaru LF, Ungur L (2006) MOLCAS SINGLE_ANISO routines. University of Leuven, Belgium
38. Douglas M, Kroll NM (1974) Ann Phys 82:89–155
39. Hess BA (1985) Phys Rev A 32:756–763
40. Heß BA, Marian CM, Wahlgren U, Gropen O (1996) Chem Phys Lett 251:365–371
41. Ungur L, Chibotaru LF. http://www.molcas.org/documentation/manual/node105.html
42. Chilton NF, Collison D, McInnes EJL, Winpenny REP, Soncini A (2013) Nat Commun 4:2551
43. Rinehart JD, Long JR (2011) Chem Sci 2:2078–2085
44. Sievers J (1982) Z Phys B: Condens Matter Quanta 45:289–296
45. Baldoví JJ, Clemente-Juan JM, Coronado E, Gaita-Ariño A (2014) Inorg Chem 53:11323–11327
46. Oyarzabal I, Ruiz J, Seco JM, Evangelisti M, Camón A, Ruiz E, Aravena D, Colacio E (2014) Chem Eur J 20:14262–14269
47. Aravena D, Ruiz E (2013) Inorg Chem 52:13770–13778
48. Baldovi JJ, Borras-Almenar JJ, Clemente-Juan JM, Coronado E, Gaita-Arino A (2012) Dalton Trans 41:13705–13710
49. Baldoví JJ, Cardona-Serra S, Clemente-Juan JM, Coronado E, Gaita-Ariño A, Palii A (2012) Inorg Chem 51:12565–12574
50. Baldoví JJ, Cardona-Serra S, Clemente-Juan JM, Coronado E, Gaita-Ariño A, Palii A (2013) J Comput Chem 34:1961–1967
51. Pointillart F, Jung J, Berraud-Pache R, Le Guennic B, Dorcet V, Golhen S, Cador O, Maury O, Guyot Y, Decurtins S, Liu S-X, Ouahab L (2015) Inorg Chem 54:5384–5397
52. Lines ME (1971) J Chem Phys 55:2977–2984
53. Ungur L, Chibotaru LF (2007) POLY_ANISO program. KU Leuven, Belgium
54. Marx R, Moro F, Dorfel M, Ungur L, Waters M, Jiang SD, Orlita M, Taylor J, Frey W, Chibotaru LF, van Slageren J (2014) Chem Sci 5:3287–3293
55. Guo Y-N, Ungur L, Granroth GE, Powell AK, Wu C, Nagler SE, Tang J, Chibotaru LF, Cui D (2014) Sci Rep 4:5471
56. Batchelor LJ, Cimatti I, Guillot R, Tuna F, Wernsdorfer W, Ungur L, Chibotaru LF, Campbell VE, Mallah T (2014) Dalton Trans 43:12146–12149

57. Bernot K, Luzon J, Bogani L, Etienne M, Sangregorio C, Shanmugam M, Caneschi A, Sessoli R, Gatteschi D (2009) J Am Chem Soc 131:5573–5579
58. Gupta T, Rajaraman G (2016) Chem Commun 52:8972–9008
59. Zhang P, Zhang L, Tang J (2015) Dalton Trans 44:3923–3929
60. Ungur L, Chibotaru LF (2016) Inorg Chem 55:10043–10056
61. Orbach R (1961) Proc R Soc Lond A 264:485–495
62. Campbell VE, Bolvin H, Rivière E, Guillot R, Wernsdorfer W, Mallah T (2014) Inorg Chem 53:2598–2605
63. Li DP, Wang TW, Li CH, Liu DS, Li YZ, You XZ (2010) Chem Commun 46:2929–2931
64. Gavey EL, Al Hareri M, Regier J, Carlos LD, Ferreira RAS, Razavi FS, Rawson JM, Pilkington M (2015) J Mater Chem C 3:7738–7747
65. Ruiz J, Mota AJ, Rodriguez-Dieguez A, Titos S, Herrera JM, Ruiz E, Cremades E, Costes JP, Colacio E (2012) Chem Commun 48:7916–7918
66. Chilton NF, Langley SK, Moubaraki B, Soncini A, Batten SR, Murray KS (2013) Chem Sci 4:1719–1730
67. Cucinotta G, Perfetti M, Luzon J, Etienne M, Car PE, Caneschi A, Calvez G, Bernot K, Sessoli R (2012) Angew Chem Int Ed Engl 51:1606–1610
68. Feltham HLC, Lan Y, Klöwer F, Ungur L, Chibotaru LF, Powell AK, Brooker S (2011) Chem Eur J 17:4362–4365
69. Long J, Rouquette J, Thibaud J-M, Ferreira RAS, Carlos LD, Donnadieu B, Vieru V, Chibotaru LF, Konczewicz L, Haines J, Guari Y, Larionova J (2015) Angew Chem Int Ed 54:2236–2240
70. Xue S, Ungur L, Guo Y-N, Tang J, Chibotaru LF (2014) Inorg Chem 53:12658–12663
71. Upadhyay A, Singh SK, Das C, Mondol R, Langley SK, Murray KS, Rajaraman G, Shanmugam M (2014) Chem Commun 50:8838–8841
72. Bhunia A, Gamer MT, Ungur L, Chibotaru LF, Powell AK, Lan Y, Roesky PW, Menges F, Riehn C, Niedner-Schatteburg G (2012) Inorg Chem 51:9589–9597
73. Ou-Yang JK, Saleh N, Fernandez Garcia G, Norel L, Pointillart F, Guizouarn T, Cador O, Totti F, Ouahab L, Crassous J, Le Guennic B (2016) Chem Commun 52:14474–14477
74. Vignesh KR, Langley SK, Murray KS, Rajaraman G (2017) Inorg Chem 56:2518
75. Jung J, da Cunha TT, Le Guennic B, Pointillart F, Pereira CLM, Luzon J, Golhen S, Cador O, Maury O, Ouahab L (2014) Eur J Inorg Chem 2014:3888–3894
76. Costes JP, Titos-Padilla S, Oyarzabal I, Gupta T, Duhayon C, Rajaraman G, Colacio E (2015) Chem Eur J 21:15785–15796
77. Gregson M, Chilton NF, Ariciu A-M, Tuna F, Crowe IF, Lewis W, Blake AJ, Collison D, McInnes EJL, Winpenny REP, Liddle ST (2016) Chem Sci 7:155–165
78. Sun W-B, Yan P-F, Jiang S-D, Wang B-W, Zhang Y-Q, Li H-F, Chen P, Wang Z-M, Gao S (2016) Chem Sci 7:684–691
79. Long J, Shestakov BG, Liu D, Chibotaru LF, Guari Y, Cherkasov AV, Fukin GK, Trifonov AA, Larionova J (2017) Chem Commun 53:4706–4709
80. Rajaraman G, Singh SK, Gupta T, Shanmugam M (2014) Chem Commun 50:15513–15516
81. Gupta T, Velmurugan G, Rajeshkumar T, Rajaraman G (2016) J Chem Sci 128:1615–1630
82. Kishi Y, Pointillart F, Lefeuvre B, Riobe F, Le Guennic B, Golhen S, Cador O, Maury O, Fujiwara H, Ouahab L (2017) Chem Commun 53:3575–3578
83. Lucaccini E, Briganti M, Perfetti M, Vendier L, Costes J-P, Totti F, Sessoli R, Sorace L (2016) Chem Eur J 22:5552–5562
84. Costes JP, Titos-Padilla S, Oyarzabal I, Gupta T, Duhayon C, Rajaraman G, Colacio E (2016) Inorg Chem 55:4428–4440
85. Liu J-L, Chen Y-C, Zheng Y-Z, Lin W-Q, Ungur L, Wernsdorfer W, Chibotaru LF, Tong M-L (2013) Chem Sci 4:3310–3316
86. Ding Y-S, Chilton NF, Winpenny REP, Zheng Y-Z (2016) Angew Chem Int Ed 55:16071–16074

87. Chen Y-C, Liu J-L, Lan Y, Zhong Z-Q, Mansikkamäki A, Ungur L, Li Q-W, Jia J-H, Chibotaru LF, Han J-B, Wernsdorfer W, Chen X-M, Tong M-L (2017) Chem Eur J 23:5708–5715
88. Lucaccini E, Sorace L, Perfetti M, Costes J-P, Sessoli R (2014) Chem Commun 50:1648–1651
89. Le Roy JJ, Jeletic M, Gorelsky SI, Korobkov I, Ungur L, Chibotaru LF, Murugesu M (2013) J Am Chem Soc 135:3502–3510
90. Chilton NF, Goodwin CAP, Mills DP, Winpenny REP (2015) Chem Commun 51:101–103
91. Chilton NF (2015) Inorg Chem 54:2097–2099
92. Singh MK, Yadav N, Rajaraman G (2015) Chem Commun 51:17732–17735
93. Rinehart JD, Fang M, Evans WJ, Long JR (2011) Nat Chem 3:538–542
94. Rajeshkumar T, Rajaraman G (2012) Chem Commun 48:7856–7858
95. Hu Z, Dong B-W, Liu Z, Liu J-J, Su J, Yu C, Xiong J, Shi D-E, Wang Y, Wang B-W, Ardavan A, Shi Z, Jiang S-D, Gao S (2017) J Am Chem Soc
96. Liu F, Krylov DS, Spree L, Avdoshenko SM, Samoylova NA, Rosenkranz M, Kostanyan A, Greber T, Wolter AUB, Büchner B, Popov AA (2017) Nat Commun 8:16098
97. Singh MK, Rajaraman G (2016) Chem Commun 52:14047–14050
98. Vieru V, Ungur L, Chibotaru LF (2013) J Phys Chem Lett 4:3565–3569
99. Chen C-H, Krylov DS, Avdoshenko S, Liu F, Spree L, Yadav R, Alvertis A, Hozoi L, Nenkov K, Kostanyan A, Greber T, Wolter AUB, Popov AA (2017) Chem Sci 8:6451–6465
100. Boulon ME, Cucinotta G, Liu SS, Jiang SD, Ungur L, Chibotaru LF, Gao S, Sessoli R (2013) Chem Eur J 19:13726–13731
101. Flanagan BM, Bernhardt PV, Krausz ER, Lüthi SR, Riley MJ (2001) Inorg Chem 40:5401–5407
102. Singh SK, Pandey B, Velmurugan G, Rajaraman G (2017) Dalton Trans 46:11913–11924
103. Das C, Upadhyay A, Vaidya S, Singh SK, Rajaraman G, Shanmugam M (2015) Chem Commun 51:6137–6140
104. Pedersen KS, Ungur L, Sigrist M, Sundt A, Schau-Magnussen M, Vieru V, Mutka H, Rols S, Weihe H, Waldmann O, Chibotaru LF, Bendix J, Dreiser J (2014) Chem Sci 5:1650–1660
105. Boulon ME, Cucinotta G, Luzon J, Degl'Innocenti C, Perfetti M, Bernot K, Calvez G, Caneschi A, Sessoli R (2013) Angew Chem Int Ed 52:350–354
106. Liu J-L, Yuan K, Leng J-D, Ungur L, Wernsdorfer W, Guo F-S, Chibotaru LF, Tong M-L (2012) Inorg Chem 51:8538–8544
107. Blackburn OA, Chilton NF, Keller K, Tait CE, Myers WK, McInnes EJL, Kenwright AM, Beer PD, Timmel CR, Faulkner S (2015) Angew Chem 127:10933–10936
108. Singh SK, Gupta T, Ungur L, Rajaraman G (2015) Chem Eur J 21:13812–13819
109. Li Q-W, Wan R-C, Chen Y-C, Liu J-L, Wang L-F, Jia J-H, Chilton NF, Tong M-L (2016) Chem Commun 52:13365–13368
110. Gupta SK, Rajeshkumar T, Rajaraman G, Murugavel R (2016) Chem Commun 52:7168–7171
111. Chen Y-C, Liu J-L, Wernsdorfer W, Liu D, Chibotaru LF, Chen X-M, Tong M-L (2017) Angew Chem Int Ed 56:4996–5000
112. Meng Y-S, Qiao Y-S, Zhang Y-Q, Jiang S-D, Meng Z-S, Wang B-W, Wang Z-M, Gao S (2016) Chem Eur J 22:4704–4708
113. Ishikawa N, Sugita M, Ishikawa T, Koshihara SY, Kaizu Y (2003) J Am Chem Soc 125:8694
114. Ganivet CR, Ballesteros B, de la Torre G, Clemente-Juan JM, Coronado E, Torres T (2013) Chem Eur J 19:1457–1465
115. Mannini M, Bertani F, Tudisco C, Malavolti L, Poggini L, Misztal K, Menozzi D, Motta A, Otero E, Ohresser P, Sainctavit P, Condorelli GG, Dalcanale E, Sessoli R (2014) Nat Commun 5:4582
116. Chen Y, Ma F, Chen X, Dong B, Wang K, Jiang S, Wang C, Chen X, Qi D, Sun H, Wang B, Gao S, Jiang J (2017) Inorg Chem Front 4:1465
117. Chen Y, Ma F, Chen X, Dong B, Wang K, Jiang S, Wang C, Chen X, Qi D, Sun H, Wang B, Gao S, Jiang J (2017) Inorg Chem 56:13889–13896

118. Singh SK, Gupta T, Rajaraman G (2014) Inorg Chem 53:10835–10845
119. Pointillart F, Cador O, Le Guennic B, Ouahab L (2017) Coord Chem Rev. https://doi.org/10.1016/j.ccr.2016.1012.1017
120. Gupta T, Rajaraman G (2014) J Chem Sci 126:1569–1579
121. Lunghi A, Totti F, Sessoli R, Sanvito S (2017) Nat Commun 8:14620
122. Vignesh KR, Soncini A, Langley SK, Wernsdorfer W, Murray KS, Rajaraman G (2017) Nat Commun 8:1023. https://doi.org/10.1038/s41467-017-01102-5